Theses and Dissertations   Graduate School

2016

Versatile Synthesis of Transition Metal Phosphides: Emerging Front-runners for Affordable Catalysis

April C. Mattei
Virginia Commonwealth University

Versatile Synthesis of Transition Metal Phosphides: Emerging Front-runners for Affordable Catalysis

A dissertation submitted in partial fulfillment of the requirements for the degree of Doctor of Philosophy at Virginia Commonwealth University

By

April C. Mattei

Formerly known as April C. Hines

B.S., Randolph-Macon College, 2010

Principal Investigator: Everett E. Carpenter

Professor of Chemistry

Virginia Commonwealth University

July 2016

Acknowledgements

During my time at Virginia Commonwealth University there are many people that have positively impacted my experience and aided me in my success in and outside of the classroom and laboratory. First and foremost I would like to thank the VCU Chemistry Department for allowing me the opportunity to attend this institution and their dedication to excellence and assistance in all of my academic and professional endeavors. In addition to the department, the support of my fellow lab mates is unmatched and greatly appreciated and is all supported with the knowledge and assistance of our PI, Dr. Everett Carpenter. Together this group has provided countless laughs, academic encouragement and great friendship. Lastly, nothing would be possible without the love and support of my family and friends and loving husband who have kept encouraging me throughout this entire process. Thank you to all for a memorable experience.

Table of Contents

List of Figures and Tables

Abstract

Versatile Synthesis of Transition Metal Phosphides: Emerging Front-runners for Affordable Catalysis

By: April C. Mattei

Formerly known as April C. Hines

A dissertation submitted in partial fulfillment of the requirements for the degree of Doctor of Philosophy at Virginia Commonwealth University

Virginia Commonwealth University, 2016

Principal Investigator: Everett E. Carpenter

Professor of Chemistry

Transition metal phosphide materials have found themselves at the forefront of research revolving around energy applications. Due to the vast range of properties possessed by marginally different phase compositions, binary and ternary metal phosphides are utilized as catalysts, semi-conductors and magnetocaloric materials along with many others. These attractive properties, which are highly phase dependent, call for a versatile and cost effective synthesis route for various phosphide materials without sacrificing properties important at the nanoscale such as particle size and morphology.

The primary focus outlined in the work of this dissertation pertains to a versatile wet chemical synthesis capable of producing multiple phases of binary and ternary phosphides containing one or more of the transition metals cobalt, iron and nickel. These metals were of particular interest due to the proven catalytic activity of iron, cobalt or nickel binary phases and the lack of research conducted on the corresponding ternary phases. The challenge presented by wet chemical synthesis methods is the ability to separate different crystal phases of metal phosphide in a short amount of time, with less toxic and lower cost chemicals, and a simple synthetic process with the ability to produce products on a larger scale. Oleylamine was used as a solvent, capping agent and reducing agent along with trioctylphosphine or triphenylphosphine as a phosphorus source. Many binary phosphide phases were synthesized with the same method and purity of phase was controlled primarily with temperature or phosphorus to metal ratio (P:M). At lower temperatures (290-320°C) or lower P:M (4:1) Ni_3P, Ni_2P, Fe_2P, and Co_2P were synthesized while higher temperatures (330-360°C) or higher P:M (22:1) produced Ni_5P_4, $Ni_{12}P_5$, FeP and CoP. Ternary phosphides FeCoP and CoNiP were also successfully synthesized at temperatures of 300-330°C with small excesses of phosphorus (2-5 molar excess).

Preliminary catalytic studies for the evolution of hydrogen gas were conducted to test the efficacy of phosphide materials produced via the simplistic oleylamine method. Ni_2P was found to have the highest activity toward hydrogen evolution with an overpotential of 320 mV which is comparable and in some cases better than other unsupported phosphide catalysts of the same phase. The ability to control phase composition using a simple, cost effective wet chemical synthesis is promising for the future production of active metal phosphide materials.

Chapter 1: Introduction

1.1 Overview

Transition metal phosphides (TMPs) have a wide array of properties that are sought after both commercially and fundamentally. These properties are highly dependent upon the phase of the transition metal phosphide and include categories such as semiconductors, ferromagnets, catalysts etc. TMPs are typically segregated into two main groups, binary phosphides are composed of a single metal and phosphorus, while polyphosphides comprise more than one metal and phosphorus. For the purpose of this work, the only types of polyphosphides that will be explored are those with only two types of metal and will be referenced as ternary phosphides. For example, Fe_3P is a ferromagnet with a high transition temperature, while Fe_2P is a small band-gap semiconductor. [1] Similarly, Ni_2P is one of the most highly active catalysts for hydrodesulfurization (HDS) and hydrodenitrogenation (HDN), while NiP_2 is a promising negative electrode for lithium-ion batteries. [2,3]

Transition metal phosphides of many varieties, particularly those of iron, nickel and cobalt have gained popularity in recent years due to their promising results that either make them a more cost-effective alternative, or outweigh the current performance of an existing material. Due to their applauded performances in current critical research in the fields of ion-battery capacity, hydroprocessing of petroleum feedstocks and renewable energy by hydrogen evolution, it is pertinent to prepare viable synthetic routes for their transitions into industrial-level production.

1.2 Uses of Transition Metal Phosphides

The identity of almost every metal phosphide is known because of the ease of reactivity of the phosphide ion with most less-electronegative elements. Phosphides have a wide range of chemical and physical properties and for that reason are difficult to place into exact categories. One viable suggestion for classification is based upon stoichiometry and broken into three separate classes; phosphorus-rich, metal-rich and monophosphides. Phosphorus-rich consist of those with a metal-to-phosphorus ratio greater than one, while the metal-rich ratio is less than one and a monophosphide's ratio is exactly one. Research centered around transition metal phosphides has skyrocketed due to their utility across many different applications. Applications attracting the most attention in recent years heavily revolve around energy sources. Treatment of current petroleum feedstocks and bio-oils, high capacity electrodes for sodium and lithium-ion batteries and catalytic generation of hydrogen via water splitting are topics at the forefront of the research field for transition metal phosphides.

The removal of sulfur and nitrogen from fuel feed-stocks has been of particular interest as the impurity standards have become more stringent for transportation fuels. Upon burning fuels with high contents of nitrogen and sulfur, their respective oxides are released into the atmosphere. High concentrations of SO_2 in the atmosphere was discovered to be harmful to plant and animal ecosystems as well as the human respiratory system which lead to higher restrictions on emissions implemented by the Environmental Protection Agency (EPA) and other regulatory agencies worldwide since the 1970s. Currently the government regulations in the U.S., Europe and Japan all limit the sulfur contents of diesel to less than 10 parts per

million.[4] Due to these regulations, catalysts are used to treat fuel feedstocks before they are burned for energy purposes. The removal of organonitrogen compounds is critical to achieving ultra-low sulfur levels because their presence inhibits the removal of sulfur and can potentially poison catalyst further down the processing line for fuels.

While supported metal catalysts, such as Pt[5], Ni-Mo-S[6] and Co-Mo-S[7] have been praised for their efficiency, cost in the case of Pt and recyclability in the cases of Ni-Mo and Co-Mo are a concern. Due to those obstacles, metal phosphides have been heavily researched for their catalytic activities with respect to hydrodesulfurization (HDS)[8], hydrodenitrogenation (HDN)[9]. Ni_2P has established itself throughout the years as the leader for catalysis in hydrodesulfurization and is making headway in the catalysis in many other realms. Its activity for HDS is proven higher than the sulfided Ni-Mo and Co-Mo materials and its cost is much less than that of the supported Pt catalysts.

Lithium-ion batteries are currently at the top of the portable electronics pyramid and are praised for their light weight as well as their quick and efficient recharging capabilities. High capacity electrode materials are needed for Lithium-ion transport to prevent dendritic structure formation leading to a decrease in overall coulombic efficiency. A widely used material is graphite which interacts with lithium ions reversibly, possesses good conductivity and requires a low electrochemical potential. Although there are many positive things about this material, it is being rivaled by other electrode candidates that possess a higher capacity for lithium-ions.

The maximum amount of lithium ions able to intercalate into the graphitic carbon structure is 1 ion per 6 carbon atoms which translates to a capacity of 372 mAh g^{-1}. Transition

metal phosphides containing the metals iron, cobalt and nickel are at the forefront of the lithium-ion electrode research due to their higher capacities and similar properties to graphite. Theoretically Fe_2P and FeP_2 have capacities of 563 and 1365 mAh g^{-1} respectively and have gained research interest as carbon-free anodes with promising performance.[10] Co_2P and CoP were also investigated as potential anodes to compete with graphite and CoP registered 630 mAh g^{-1} with good recyclability. [11] Once again, the front-runner, Ni_2P has displayed impressive capacity results among Ni_2P nanoparticles and Ni_2P nanowires yielding capacities of 742 mAh g^{-1} and 909 mAh g^{-1} respectively.[12-13] Due to these auspicious results and continued research revolving around transition metal phosphides as anodes for lithium-ion and sodium-ion batteries, further investigation into procedures for efficiently synthesizing phosphides of many phases and sizes in a single system is advantageous.

$$\text{(Equation 1)} \qquad\qquad H_2O\ (l) \rightarrow H_2\ (g) + \frac{1}{2}O_2\ (g) \quad \Delta G^0 = 237.2\ kJ\ mol^{-1}$$
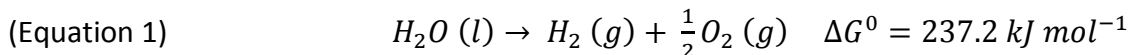
One of the most exciting new endeavors for utilizing transition metal phosphides is for the evolution of hydrogen gas from water. The electrolysis of water (Equation 1) is an electrolytic reaction that converts water into gaseous hydrogen and oxygen. This electrolysis is a combination of two important half reactions that will be further discussed in Chapter 5 of this text. The abundance of water in combination with the energy potential of hydrogen gas makes this system a very intriguing one to try to conquer. Efficient production of hydrogen by the electrolysis of water is an increasingly important reaction as limited fossil fuels are consistently depleted, and demands for energy continue to increase. The spotlight tends to shine on hydrogen due to it having the largest energy density over any other fuel known in the world

and its green production from renewable resources. The best known catalyst for the hydrogen evolution reaction (HER) in terms of efficacy is platinum. Although incredible effective at producing hydrogen, large scale implementation of hydrogen evolution by platinum metal is limited due to its high cost and low abundance.[14]

Due do the impracticality of Pt as a viable candidate for large scale production, many other avenues have been explored over the last two decades for materials that are significantly lower in cost and competitive in catalytic ability. A few classes of materials have been considered as potential alternative catalysts for HER including metal sulfides, selenides and most recently phosphides. Most of these alternatives include the metals cobalt, iron, nickel or molybdenum which have all shown high HER activity. Transition metal phosphides compared to other non-precious metal catalysts have shown high HER activity and are being heavily research as a viable candidate for large scale hydrogen evolution implementation. At the forefront of this research, phases that have sparked the most attention for this application are Ni_2P, $Ni_{12}P_5$, Co_2P and CoP.[3,15–24]

For some catalysts, a synergistic effect between two metals is often observed in which the activity of the mixed metal catalyst such as a ternary phosphide is higher than that of its monometallic counterparts. A known example of this is Ni-Mo-S catalysts for HDS.[25] However, catalytic activities for bimetallic phosphide catalysts have proven to be more of a complex system, as it has produced ternary catalysts with lower[26], intermediate[27], and higher[28–30] activities than their binary phosphide compounds. The synthesis of these ternary phosphide compounds is made possible by the ability of the interacting metals to form solid solutions,

leaving the overall crystal structure virtually unchanged. In the case of phosphides, studies have shown that Ni is capable or forming a solid solutions of the type $(Ni_{1-x}M_x)_2P$, where M = Mo, Co, Fe, Mn, Cr.[31,32]

1.3 Synthesis Strategies of Transition Metal Phosphides

The synthesis of binary transition metal phosphides, particularly Co_xP_y and Ni_xP_y, has been presented through many different avenues that span across benchtop, solvothermal, furnace and syringe pump apparatuses. CoP nanowires have been synthesized by O'Brien et al. by thermal decomposition in the presence of alkylphosphonic acids in oleylamine (OAm) and trioctylphosphine oxide (TOPO), while hollow urchin-like particles of the same phase were made in the presence of triphenylphosphine (TPP) and OAm.[33,34] Xie and coworkers were able to produce Co_2P hollow spheres and tubes using an autoclave approach using yellow phosphorus and ethanol at long reaction times (30-48 hrs).[35] Many different phases of Ni_xP_y have been synthesized and studied, however, the main phase of interest is Ni_2P due to its ability to form solid solutions with Co_2P as well as its superior performance over many catalytic platforms. Ni_2P nanowires have been synthesized by slow injection of Ni-Trioctylphosphine (TOP) complex into preheated solvent via a syringe pump[13] and hollow Ni_2P nanoparticles have been reported using conversion of Ni templates in the presence of TOP, and the reaction of Ni salt precursor in OAm and TOP.[36,37] The applications for Ni_2P encompass photocatalytic degradation of organic dyes[38], HDS[39], HDN[9], HER[40] etc. Figure 1.3.1 shows the general synthetic parameters of binary transition metal phosphides with respect to temperature, phosphorus source and synthetic method.
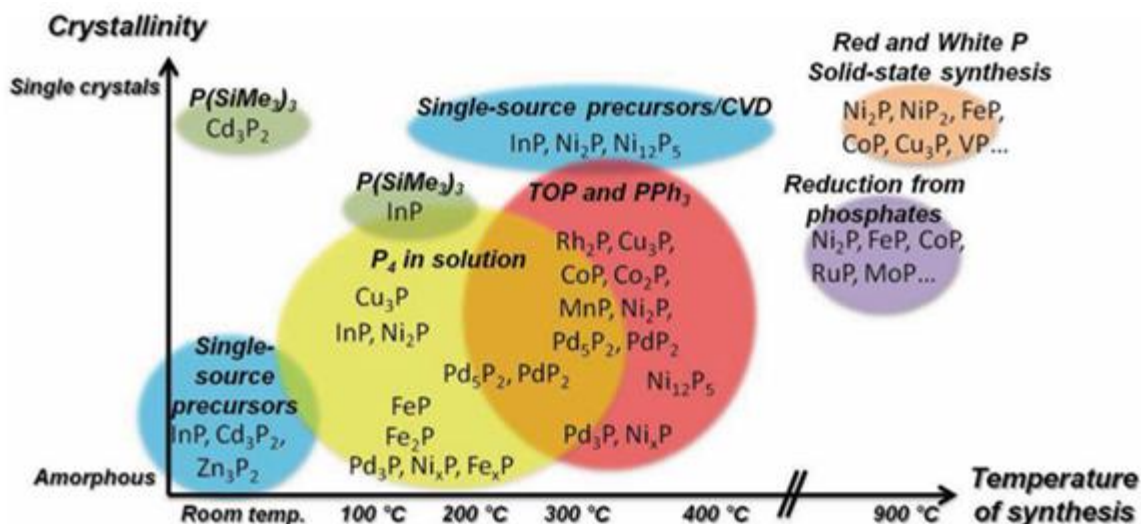
Figure 1.3.1: General Synthetic Parameters and Phase Identifications of Transition Metal

Phosphides

For the catalysis of HDS, it has been suggested and subsequently proven previously that $Co_xNi_{2-x}P$ has a higher activity than Co_2P or Ni_2P alone. Bussell et al. has presented a $Co_{0.1}Ni_{1.9}P$ catalyst that has a 34% higher activity for the HDS of thiophene than its optimized Ni_2P catalyst[30] and comparable conversions between Ni_2P and $Co_{0.1}Ni_{1.9}P$ in the HDN of carbazole.[41] Meanwhile, Smith et al. have found that in the case of 4,6 dimethyldibenzothiophene (DMDBT) that activity of Co doped Ni_2P catalyst is slightly higher and the addition of Co enhances the selectivity toward direct desulfurization as opposed to the hydrogenation route.[28] These catalysts were generally prepared by an impregnation route and subsequent temperature programmed reduction (TPR) method which tends to be lengthy in reaction and drying time. Since the monometallic phosphides have taken off in recent years, investigation into bimetallic phosphides has been neglected.

In this study, $Co_xNi_{2-x}P$ and $Co_xFe_{2-x}P$ are formed in a batch type process that has the potential for scalability. Co_2P, Ni_2P and $Co_xNi_{2-x}P$ are easily prepared by the reduction of metal salts in the presence of oleylamine and a phosphorus source, either trioctylphosphine (TOP) or triphenylphosphine (TPP). These unsupported catalysts are tested for their efficacy toward the hydrogen evolution reaction and the photocatalytic degradation of Rhodamine B.

1.4 The Oleylamine System

Wet chemical syntheses using organic solvents has proven to be a fruitful avenue for tailored nanoparticle synthesis. These systems allow for controlled reduction, nucleation and growth of particles of multiple identities by adjusting the concoction of solvents and surfactants appropriately. Nanoparticles are vastly different from their bulk counterparts in terms of properties and reactivity and can be different from one another with a subtle change in morphology, size or crystal structure. It is this control over shape, size, and crystalline structure that make solution synthesis appealing in the nanoparticle community.

One multi-faceted organic solvent that has gained much attention over the last few decades is oleylamine (Figure 1.6.1). Oleylamine is a viscous, long-chain primary amine that has been proven to be effective as a mild reducing agent, surfactant, high boiling point organic solvent or sometimes even a combination of these usages. In certain cases, oleylamine has been known to form complex compounds with some metal ions forming a metastable type of secondary precursor that is successively decomposed in solution to yield many different types of nanoparticles.
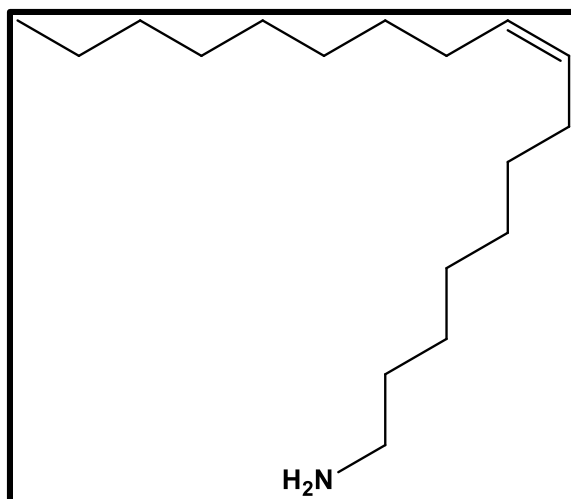
Being a liquid at room temperature, oleylamine is friendlier to work with in solution-type synthesis as a surfactant compared to other long chain alkylamines which solidify upon cooling due to their higher melting points. In addition to having a low melting point, oleylamine has a relatively high boiling point compared to other organic solvents of 365°C. This low melting point and high boiling point make oleylamine attractive for use as a surfactant and solvent in many nanoparticle syntheses.

Due to the unique "cis" orientation about the double bound carbons compared to its other chain-like counterparts, oleylamine produces particles of different morphologies than that of other primary alkylamines with similar basicity and affinity through the amine functional group. Its lack of linearity allows for a more spherical nanoparticle formation as opposed to long-range ordered materials (i.e. nanorods). However when used as a co-surfactant with certain compounds, oleic acid for example, oleylamine has also been proven to form rod-like

structures.[42] For these reasons it is common for oleylamine to be used as a surfactant or co-surfactant in many organic nanoparticle syntheses.

Oleylamine has also been proven capable of reducing metal ions at high temperatures. Not all metal ions however are capable of reduction by such a mild reducing agent. For example, iron, cobalt and nickel ions in the 2+ state are capable of being reduced by oleylamine however Mn^{2+} ions are not. It is unclear exactly the cut-off is for reducing power of oleylamine but it likely lies somewhere between ions with reduction potentials between -0.7618 and

-1.185 which correspond to the reduction potentials of Zn^{2+} and Mn^{2+} respectively.

Due to the choice of precursor for this work, the likelihood of the mechanism for oleylamine reduction outlined in Figure 1.4.2 is likely. Acetate precursors are known to degrade at high temperatures to form metal oxide and metal due to the decomposition chemistry of the acetate.[43–45] Nickel acetate tetrahydrate has been studied and proven to from $NiCO_3$ which further degrades into NiO and Ni metal. Due to the similarities between cobalt and nickel and prior proof on many occasions of the ability of oleylamine to provide reduction of both metals, the mechanism below is adopted for the reduction of metal oxide to form metal using oleylamine.
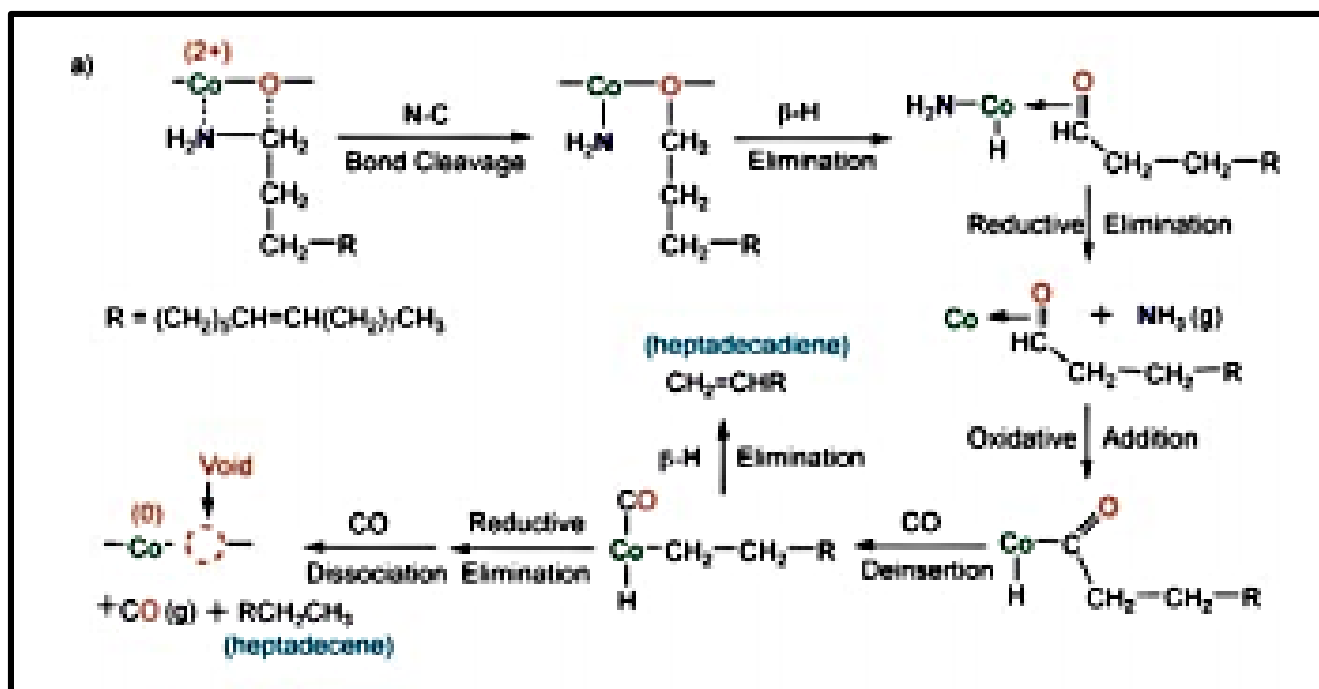
Figure 1.4.2: Reduction of fcc CoO to fcc Co by oleylamine [46]

In addition to its versatility, commercial oleylamine has a much lower cost than commonly used pure alkylamines such as hexadecylamine (HDA) and octadecylamine (ODA). This organic solvent is used in many variations and was chosen as a result of its versatility and potential for facile, cost-effective and scalable synthesis of many variations of transition metal phosphides for catalytic applications.[47]

Chapter 2: Characterization Techniques

The applications and properties of nanoparticles are highly dependent upon many characteristics; chemical composition, shape, size, surface area and crystal structure are all of interest when characterizing nanoparticles. Since it has been confirmed that nanoparticles can be vastly different from their bulk counterparts, more instruments are constantly being developed or made more sensitive in order to better understand the chemistry behind their subtle differences. These instruments often utilize magnetic fields, electron beams, x-rays or other forms of light to quantitatively or qualitatively measure some of the above characteristics of nanoparticles. Due to the vast amount of information one can collect on a single sample from multiple characteristics, the process of how these instruments work and ways to interpret their data must be introduced and explained. This chapter will explain how different instruments were used to characterize any and all of the materials made in this work. A summary of the techniques discussed can be found in table 2.1.1 below.

Table 2.1.1: Summary Characterization Techniques to be Covered in Chapter 2

Technique	Advanced techniques	Application
X-ray Diffraction (XRD)	Scherrer Analysis, Rietveld Refinement	Crystalline phase identification, crystal size determination, unit cell parmaters
Inductively Coupled Plasma-Optical Emission Spectrometry (ICP-OES)	--	Elemental analysis
Ultraviolet-visible Spectrometry (UV-vis)	--	Absorbance and concentration measurements
Scanning Electron Microscopy (SEM)	--	Surface morphology and topography determination
Transmission Electron Microscopy (TEM)	Diffraction, EELS mapping	Particle shape and size, crystal structure, elemental mapping
Vibrating Sample Magnetometry (VSM)	--	Magnetic saturation and coercivity

2.2 Powder X-ray Diffraction (XRD)

X-ray Diffraction is an analytical technique that uses the scattering of X-rays to determine the phase identification of a crystalline material. This technique is used widely among scientists not only for the information it provides, but also due its ease of use, quick data acquisition and non-destructive nature. X-ray diffraction is particularly useful for identification because it can distinguish the difference between compounds whose chemical identities are the same but crystal structures are different (i.e. glass and quartz).

The acquired data from an X-ray diffraction spectrum is based on the constructive interference of X-rays and a crystalline sample. X-rays are generated by a cathode ray tube, filtered to produce monochromatic radiation and collimated using slits and masks toward a

crystalline target. In a typical x-ray diffraction experiment, the sample is irradiated with a single

frequency of radiation across many angles. At certain angles, interactions of the sample and the

incident rays produce constructive interference resulting in diffracted rays which obey Bragg's

Law. Bragg's Law relates the wavelength of the incident radiation to the angle of the diffracted

ray and the lattice spacing of the crystalline sample by the equation 1:

<div style="text-align:center">

(Equation 1) $$n\lambda = 2dsin\theta$$

</div>

where n is a positive integer of wavelengths, λ is the wavelength of the incident ray, θ is the

angle of diffraction and d is the distance between adjacent atoms in a crystalline material, also

known as lattice spacing. The diffracted X-rays are directed toward a detector which translates

those rays to an intensity signal that manifests itself in the form of a peak at the angle of

constructive interference, known as a diffractogram. Figure 2.2.1 is a schematic of Bragg

diffraction. Determining the identity of a sample is achieved by comparing its diffractogram to

known standards. The largest known database for such standards is accessible from the

International Centre for Diffraction Data (ICDD).
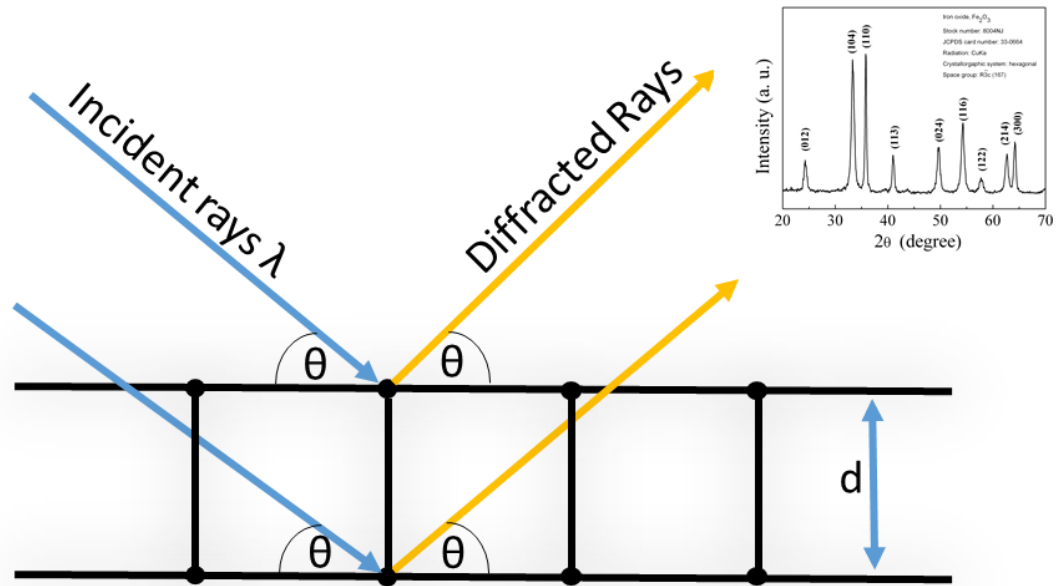
Figure 2.2.1 Schematic of Bragg Diffraction

The wavelength of the incident X-rays is dependent upon the X-ray source the diffractometer is equipped with. The most common source used is a Cu Kα radiation with a wavelength of 1.5418 Å. Other sources are available to use if desired to limit interference with elements of interest, however, their efficiencies of X-ray generations vary which can alter the intensity of the signal. Some atoms that absorb the incident X-rays and emit them as X-rays of a different wavelength (fluoresce) can cause elevated background noise when using sources of radiation that are similar to the analyte. For instance, samples containing Fe and Co are susceptible to higher background noise when using Cu Kα radiation. This noise can often be eliminated by inserting a diffracted beam monochromator, but is more difficult to remedy if the sample signal is low.

While XRD is useful for many reasons, it also has some limitations. XRD is a characterization technique for the bulk of a sample due to the penetration depth of the X-ray being hundreds of nanometers for most materials, therefore other analytical techniques must be executed to deduce any information about the surface of a sample. In addition to elements that fluoresce, many characteristics of the sample can affect the diffractogram and cause it to deviate slightly from the know standard, making some difficult to identify with absolute certainty if working with a complex system. Lattice strain can cause peak positions to shift to lower angles and small grain size or asymmetric lattice strain can cause peak broadening.

2.2.1 Peak Broadening- Scherrer Analysis

Named after Russian physicist Paul Scherrer, the Scherrer formula was implemented in 1918 upon the discovery that when monochromatic radiation falls on a randomly oriented mass of crystals, the diffracted beam is broadened when the particle size is small.[48] Scherrer analysis is used specifically to relate the width of a peak on a diffractogram to calculate the average grain size or crystallite size of a sample. Bragg diffraction (Figure 2.2.1) assumes that crystals are perfect and diffraction occurs at a single angle value for a given plane, therefore perfect crystals are calculated to have a peak width of zero. Upon experimentally measuring an imperfect sample synthesized in the lab, a peak width of zero is often not the case. Assuming instrument broadening has been compensated for by measuring a standard and subtracting the peak width from your sample's peak width, Scherrer's formula inversely relates the width of a given peak with the size of the crystal.

$$\tau = \frac{K\lambda}{\beta cos\theta}$$

(Equation 2)

Equation 2 shows the Scherrer formula used for crystallite estimation where τ represents the average grain size of the crystalline domains, *K* represents a dimensionless shape factor that is typically approximated to be 0.9, λ is the wavelength of the incident x-ray, β is the line broadening or width of a peak at half of the maximum (full-width half-max FWHM) and θ is the Bragg angle. With a few of these variables there are assumptions made that may skew results if those assumption are not concurrent with a particular sample or data set. The value for *K* assumes that the particles are ellipsoidal in nature, which is not the case for many particles at the nanoscale that take on a variety of shapes, thus altering their properties; rods, spheres, dendritic structures etc. β is the FWHM of a peak with the assumption that the instrumental line broadening in radians has already been subtracted. While these assumptions slightly affect the calculations accuracy, there are many other attributing factors to error within this relationship.

This technique is limited to sub-micrometer particles and is ideal for use at the nano-scale, with an upper limit corresponding to particles with a grain size around 0.1 to 0.2 μm. This often precludes samples that are ceramic or polymeric in nature as a result of these size constraints. It is important to note that the Scherrer formula provides a lower bound on particle size due to imperfect samples and a variety of other possibilities that can affect peak width other than crystallite size or instrument effects. While the most important of these other possibilities is lattice imperfections, there are many other possibilities that could play a role in

peak broadening: grain boundaries, sub boundaries, coherency strain, inhomogeneous strain, microstresses, twinning, dislocations, stacking faults, heterogeneities, and crystallite smallness.[49]

The Scherrer formula is a useful tool for X-ray diffraction analysis, but cannot be relied on for its accuracy and certainty and is rather a good estimating tool. X-ray diffraction in general is heavily biased toward crystalline components in a sample, therefore amorphous materials or those with non-uniform lattice spacing tend to produce wider peaks with low intensity. With low intensity peaks, the variance in the measurement of the FWHM becomes minuscule. This causes the measurements of the line broadening to be greatly dependent upon samples or parts of samples with the highest crystallinity. For this reason, Scherrer calculations are often prejudiced toward the largest crystals in a given sample. For uniformly crystalline samples this approximation is fairly accurate, but as properties of a sample lean toward imperfection, the validity of this approximation declines.

2.2.2 Rietveld Refinement

Developed by a Dutch crystallographer, the Rietveld refinement method is typically applied to neutron or x-ray diffraction data which refines a theoretical line profile until it matches a measured line profile, using a least squares approach. This method is used to act as a more quantitative approach to analyzing x-ray diffraction data as opposed to the qualitative approach typically used to identify phase. Typical data fitting for x-ray diffraction simply consists of matching a standard XRD crystal pattern to the crystal pattern of your sample. This fitting process is usually conducted using some form of data analysis software (X'Pert Highscore

Plus) and does its best to match peak position and relative intensities to the best candidate for the data that is acquired. The issue with this method is that it does not account for all materials and cannot accurately account for slight changes in diffraction pattern due to changes in lattice parameters or atomic positions.

In order to conduct a Rietveld analysis, parameters of the material to be analyzed first need to be modeled but inputting punitive information such as atom identification, lattice parameters, atomic positions and space group. These values were acquired from the Pearson Handbook of Lattice Spacings.[50] Once a model is generated in the software, it can then be refined using the Rietveld method to match the experimental data, thus providing a more quantitative analysis. Before this method, quantitative identification of crystal structure was only possible through analysis of a single crystal by x-ray diffraction. Since many materials of interest are very difficult, some if not impossible to acquire single crystals for analysis, this method provides accuracy of structure similar but not superior to single crystal x-ray diffraction. Rietveld analysis is especially useful to mixtures of phases or diffractograms in which not all peaks are clearly resolved. Figure 2.2.2 depicts an example of how these peaks can be distinguished by computationally fitting the Gaussian data by the method of least squares thus quantifying the data with higher certainty.
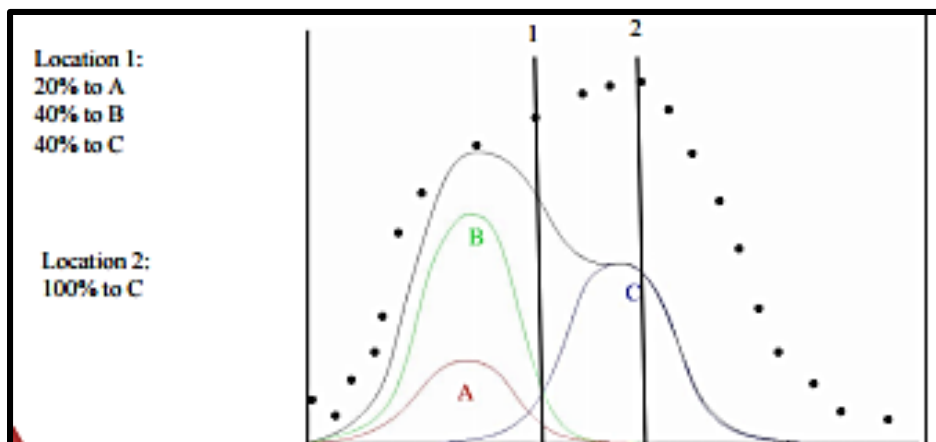
Figure 2.2.2 Example of Rietveld Refinement on an Unresolved Diffractogram

2.3 Inductively Coupled Plasma- Optical Emission Spectrometry (ICP-OES)

For many decades combustion flames were considered an easy method to analyze inorganic materials by converting inorganic solutions into free atoms to be detected and quantitatively analyzed in trace amounts by atomic absorption, emission or fluorescence spectroscopic techniques. Due to safety hazards and violent chemical reactions upon exposure to combustion flames, focus was placed on electrically generated "flames" or plasmas possessing higher gas temperatures and less reactive chemical environments. An inductively coupled plasma (ICP) is a high energy source generated by electric currents which are supplied by electromagnetic induction.[51]

ICP-OES is a type of quantitative analytical technique that revolves around the excitation and relaxation or decay of electrons in a given atom. Consider the Bohr model of an atom in Figure 2.3.1 that shows the excitation of an electron from the ground state to an excited state upon absorption of energy. When the electron relaxes back to the ground state, it emits energy

in the form of a photon of a given wavelength. Energy transitions in an atom or ion can be classified into two forms, radiational or thermal. Radiational energy transitions involve the emission or absorption of a form of electromagnetic radiation while thermal energy transitions involve an energy transfer between colliding particles. The energy, wavelength and frequency of radiational emitted or absorbed photons can be related by the Planck equation (Equation 3) where E is energy, λ is the corresponding wavelength of light, c is the speed of light, h is Planck's constant and v is the frequency of the emitted photon.
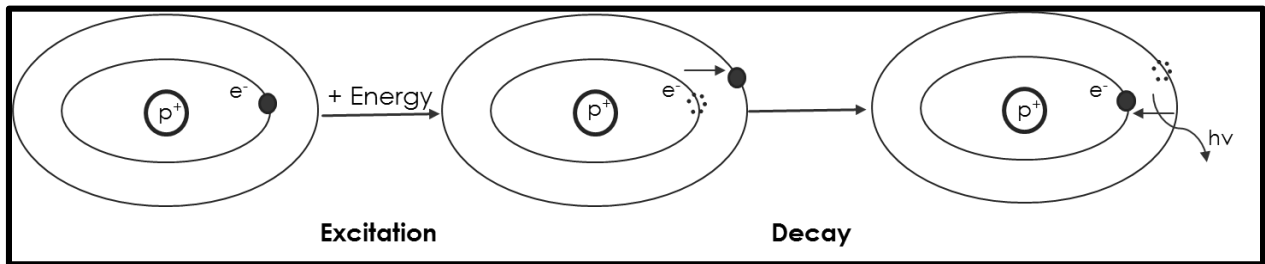
Figure 2.3.1: Bohr model of the atom showing excitation and decay of an electron in an atom

(Equation 3)
$$E = \frac{hc}{\lambda} = h\nu$$

In optical emission spectrometry (OES) the sample is subjected to energies so high that not only dissociation into atoms but also collisions capable of forming ions occur via collisional excitation. Once atoms and ions are in excited states, their electrons then decay through radiational or thermal energy transitions. The intensities of light emitted at particular wavelength are then measured and correlated to energy transitions of elements of interest. These intensities directly correlate to the quantitative value of a given element assuming the wavelength observed does not have interference from another element present with a similar

transitional energy. Accurate numerical concentration values may only be obtained if standards with a known concentration of a given analyte are made and characterized with the sample lot.

One of the key advantages to OES over other techniques is the high excitation properties associated with the high temperature sources used such as the inductively coupled plasma (ICP). The benefit of these high excitation sources is their ability to cover a wide range of energy levels of many different elements at the same time. This allows for analysis of a multitude of analytes at once considering all of the excited atoms or ions emit their unique characteristic wavelengths from multiple energy transitions around the same time. The ability to monitor multiple transitions of a single element or multiple elements simultaneously makes this technique incredibly useful but can also present drawbacks when multiple elements are being analyzed. Upon characterization of multiple elements, especially similar ones, there is an increased possibility of the most intense signals overlapping with one another. Typically this can be averted by choosing a less intense signal to monitor but sometimes this can still be problematic for samples with many different components comprised of intensities that are too close to measure separately. If interference is not an issue, sensitivity of ICP-OES is on the parts per billion scale and even lower for some elements. For the elements of particular interest; iron, cobalt, nickel and phosphorus, the detection limits all fall under 30 ppb making it possible to analyze small sample sizes which is important to consider when noting the ICP-OES is a destructive characterization technique.

2.4 Ultraviolet-visible Spectrometry (UV-vis)

When visible light passes through a colored substance, a mixed portion of wavelengths is absorbed and the remaining light that is visualized as color which is located directly across the color wheel in relation to the wavelength that are absorbed. A common feature of many colored materials, particularly organic dyes is an extensively conjugated system of pi-electrons. To understand the relationship of conjugation to color, analytical instruments like the UV-vis spectrometer have been created. UV-vis spectrometry uses ultraviolet and visible wavelengths comprised of photon energies of 36-143 kcal/mole to excited electrons in a compound. These energy transitions from the ground state to an excited state. This technique is complimentary to fluorescence spectroscopy which conversely measures transitions from excited states to the ground state.

When an organic compound is analyzed containing pi or non-bonding electrons, ultraviolet and visible light have the ability to excite these electrons to a higher anti-bonding orbital. The easier the electrons are to excite, the shorter the distance between the highest occupied molecular orbital (HOMO) and lowest unoccupied molecular orbital (LUMO). A short HOMO-LUMO distance corresponds to a longer wavelength of light that is absorbed. An exam diagram of conceivable transitions can be found in Figure 2.4.1.
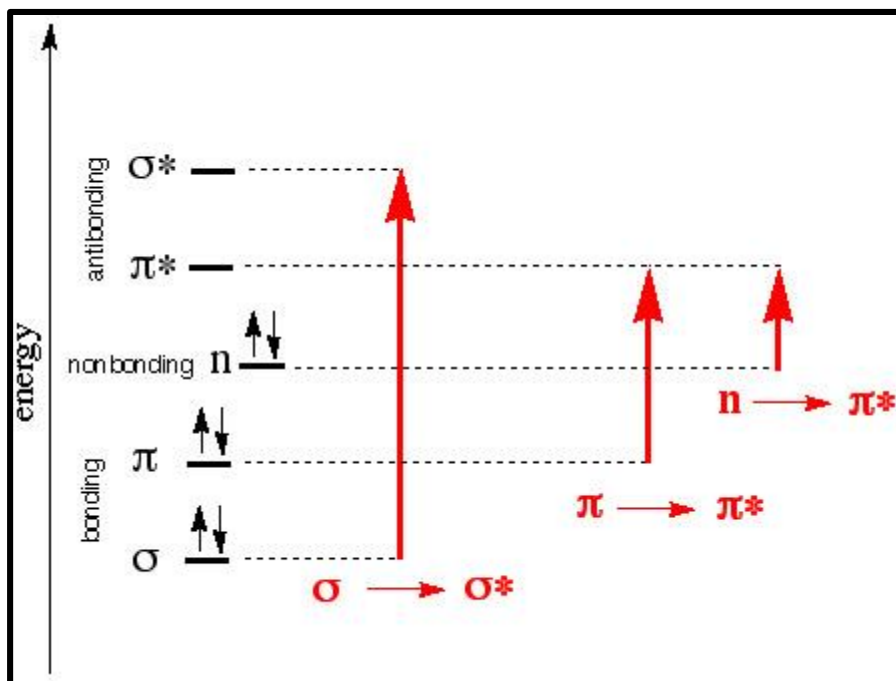
Figure 2.4.1: Example Diagram of HOMO-LUMO Transitions in UV-vis Spectroscopy

In addition to the correlation between the wavelength of light absorbed and the energy of the transition as well as the color of the sample, the concentration of a sample can also be related to the spectrum via the absorbance or intensity value of the absorbed wavelength. Concentration is related to absorbance by the Beer-Lambert Law found in Equation 4, where A is the absorbance measures, ε is the molar absorptivity coefficient that is specific to a particular compound, b is the path length of the cuvette and c is the concentration of the complex in moles per liter.

(Equation 4)
$$A = \varepsilon b c$$

2.5 Scanning Electron Microscopy (SEM)

Scanning Electron Microscopy is a qualitative surface characterization technique that utilizes a focused beam of electrons to scan across the surface of a solid substance. The electrons are scanned in a raster pattern to produce an image containing information about the surface and topography of the sample. The accelerated electrons interact with the sample and are emitted as many useful signals for analysis. The electrons responsible for generating the image seen on the screen are low energy secondary electrons which are inelastically scattered electrons emitted by atoms excited by the electron beam. These electron are often emitted from atoms that reside very close to the specimen's surface therefore yielding only surface information with a resolution of approximately 1 nm.
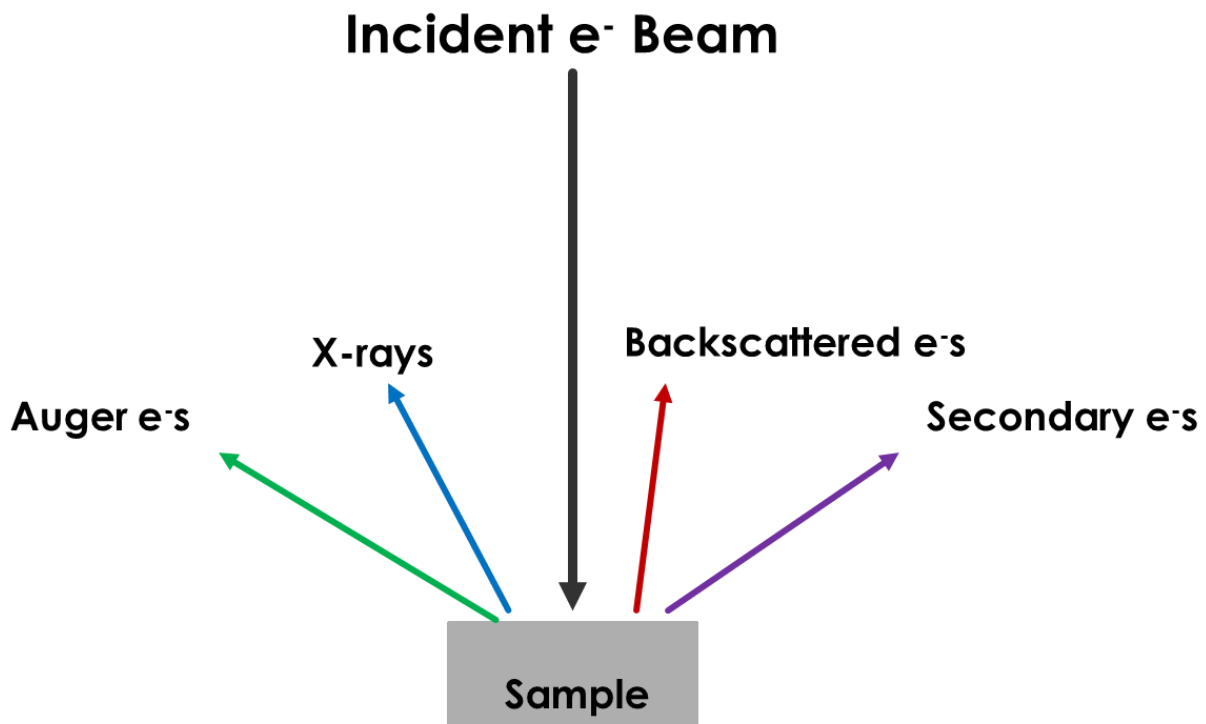
Figure 2.5.1: Diagram of Scanning Electron Microscope

2.6 Transmission Electron Microscopy (TEM)

Transmission Electron Microscopy is a complimentary and often more informative characterization technique for the analysis of nanoparticles. While SEM images give more surface information, TEM images are capable of observing smaller samples with higher resolutions and observing the "inside" of a particle since electrons are transmitted through the sample instead of scattered off the surface. This is particularly helpful for analyzing core-shell type nanoparticles or particles with holes or voids inside of them.

When the electron beam in accelerated at the sample of interest, the electrons interact with the sample in a multitude of ways that provide information about the sample. A simple diagram of these interactions is outlined in Figure 2.6.1. The most common technique using this instrument is bright field imaging and is the "standard" imaging technique for this instrument. Images are generated by measuring electrons that are transmitted through the sample without a large amount of scattering. The ability of the accelerated electrons to pass through a given sample depend of the density of the region illuminated. The differences in density produce an image containing light and dark regions that generate an image. The darkest regions are those in which electrons do not pass through the material whereas brighter regions allow some of all of the electrons to be transmitted. The shade of the produced image directly correlates to the amount of electrons passing through the material. This technique is most useful for investigating shape and size of a given sample. To ascertain more information about a sample

using TEM, more advanced techniques must be used that utilize an electron's specific

interaction with a sample.
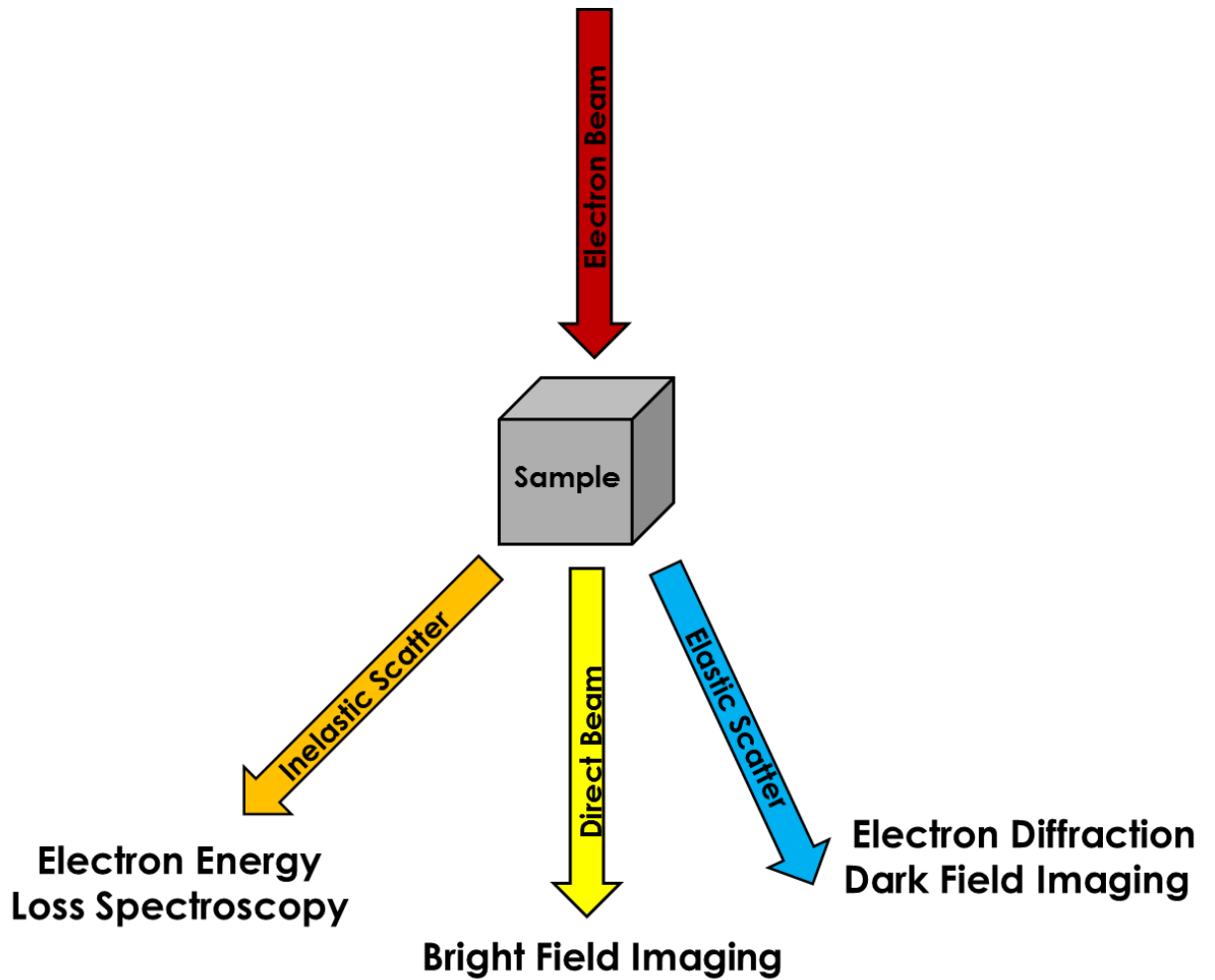
Figure 2.6.1: Schematic of Electron Interaction with Sample in TEM

2.6.1 Electron Diffraction

Typically X-ray diffraction is the most common technique used for determining

crystal structure of a sample, however electron diffraction using the TEM is another tool

capable of providing information in support of the diffractogram or to add to the information already analyzed. One major drawback of using x-ray diffraction is its limitation on smaller sized nanoparticles. Performing electron diffraction using a TEM alleviates this problem due to electrons' ability to interact with materials much stronger than x-rays allowing for diffraction analysis of small sample sizes. With this same advantage comes a threshold for size however. Due to the smaller penetration depth of the electron vs. the x-ray, electron diffraction is only most useful for particles measuring under 100 nm in diameter.[43] Electron diffraction analyzes electrons which are elastically scattered from the sample. Elastic scattering occurs when electron scatter with complete conservation of kinetic energy and leave the target unchanged from its original state.

2.6.2 Electron Energy Loss Spectroscopy (EELS)

Though diffraction techniques use elastically scattered electrons, those are not the only type of scattered electrons that can provide useful information. Inelastically scattered electrons, or electrons that do not conserve kinetic energy can be used to gather information about the type of atoms that make up a sample. Inelastically scattered electrons cause be caused as a result of energy absorbance by the same, in which the scattered electrons would possess less energy than the incident electrons. This absorbance occurs when a core electron is excited to the LUMO above the Fermi level. The amount of energy absorbed corresponds to the difference in energy between the core level and the LUMO. These energies are known for most elements on the periodic table and can be used to identify which elements are present in the

sample. By implementing an energy filter, these scattered electrons can be filtered and quantified to provide elemental analysis of a given material or part of a material.

This energy filter used for elemental analysis can also be used to generate an elemental map in which only electrons that have lost a certain amount of energy will be imaged. This allows for acquisition of not only what type of elements are in the sample of interest but also where these elements are present within the sample. This technique is referred to as EELS mapping. Although an incredibly useful technique capable of being combined with nanoparticle imaging, EELS mapping for high energy losses can produce low signals compared to a high baseline. Therefore, this technique tends to be most sensitive to elements with a low atomic number for measuring inner shell ionizations, or valence shell absorbance edge for high atomic number elements. EELS mapping was performed for Fe, Co and Ni elements for synthesized samples and monitored valence shell absorbance edges of the 3d or 2p electrons.

2.7 Vibrating Sample Magnetometry (VSM)

For samples that are magnetic is nature, the best mode of analysis of those properties is the vibrating sample magnetometer. This instrument is used to measure various magnetic properties of powder and thin film samples. Figure 2.7.1 shows a schematic of the internal parts of a VSM that are critical to attaining the magnetic information analyzed. A typical measurement is conducted by placing a small amount of magnetic sample (Usually ~ 5mg for powders) in between two electromagnets. Once between the electromagnets, the sample is constantly vibrated at a constant frequency and amplitude while a uniform magnetic field is

applied perpendicular to the axis of vibration. If a sample is indeed magnetic, this application of

a magnetic field allows for the sample to magnetize and subsequently flood the surrounding

area with magnetic flux causing induction. Induction generates an electric potential whose

amplitude is then measured by the pick-up coils in the instrument. The amplitude of the

generated electric potential is directly proportional to the magnetic moment of the sample.
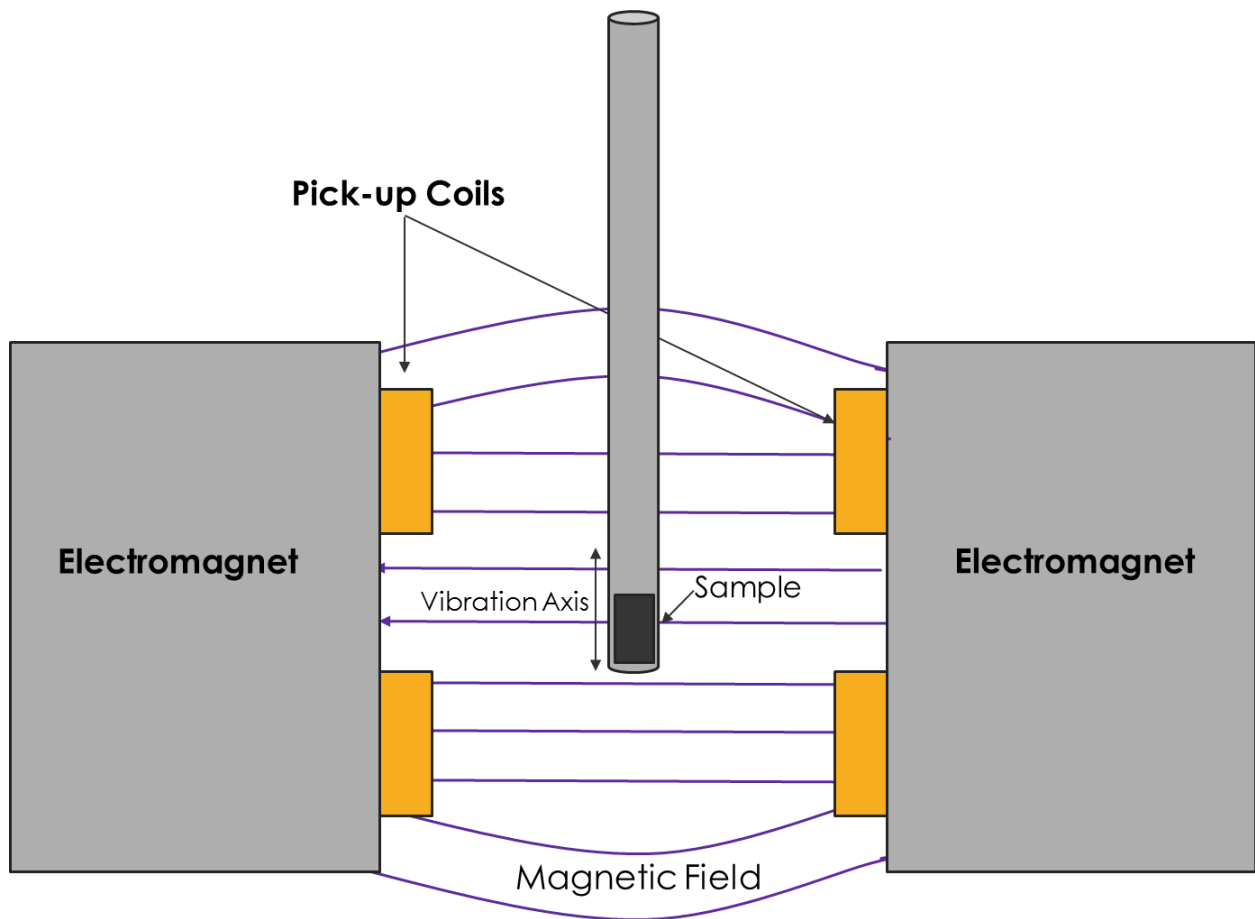
Figure 2.7.1: Schematic of Vibrating Sample Magnetometer

One of the most common experiments conducted using a VSM is the measurement of

magnetization (M) as a function of the applied magnetic field (H). This measurement for

ferromagnetic materials is often referred to as a hysteresis loop. Conducting measurements of

magnetization as a function of applied magnetic field can be used to deduce important

information about a sample such as its magnetic properties at a given temperature or the type

of magnetic material the sample is (i.e. paramagnet, diamagnet, ferromagnet etc.). Another

common and important experiment often measured is the magnetization of a sample as a

function of temperature (M (T)). This type of measurement gives more in depth information

about magnetic interaction and magnetic transitions and relate them to temperatures at which

they occur. The primary measurement used for this work is M (H) measurements due to the

lack of magnetic materials synthesized.

Chapter 3: Facile Synthesis of Binary Transition Metal Phosphides: Iron, Cobalt and Nickel Variations

3.1 Motivation

Binary phosphides consisting of Fe, Co or Ni elements were chosen due to their versatility and promise in the fields of catalysis for hydrogen evolution, hydrodesulfurization and hydrodenitrogenation, and electrodes for lithium and sodium ion-batteries. Adapting a simple method capable of producing stable, phase controlled nanoparticles that can later be supported or processed depending on their desired application is attractive for industrial applications. Current methods of synthesis typically require dangerous reagents, expensive reagents and equipment, multi-step processes or long reaction times and sometimes a combination of these. The oleylamine system is a viable system due to its versatility and capability of synthesizing various types of metal compounds with controlled phase and size. The goal of this work is to synthesize metal phosphides of three separate metals with control over phase in a simple wet chemical system. Some of these materials then are then tested for catalytic performance later on in this text to affirm the quality of particles made in relation to other works whose systems are far more expensive, complex and/or time consuming.

3.2 Introduction

Binary Phosphides are materials that are comprised of a single source of metal and phosphorus having a total of two elements in its chemical formula. The type of metal present in a given binary phosphide material is just one of the many qualities that affect the properties of the material. Important characteristics such as size, shape, crystal structure and ratio of metal to phosphorus all can play a vast role in the properties of the binary phosphide that is created. Although all of the metals experimented with in this text are magnetic in nature, not all phases

of phosphide made with these materials are magnetic. Ni_2P and Fe_2P share the share the same hexagonal crystal structure, however Fe_2P is a ferromagnetic material and Ni_2P is not. All of the other binary phosphide phases that are readily synthesized are not ferromagnetic. Binary phosphides come in a multitude of crystal structures and metal phosphide compositions that range from phosphorus rich, M: P < 1, to metal rich M: P >1. The phase of these phosphides are highly influential on the properties they possess. These properties encompass catalysis, semi-conductors, magneto-caloric materials, high capacity ion carriers, etc.

Due to their wide array of properties and applications, binary phosphides are highly sought after and are making headway in recent years toward a necessity for industrial scale production due to their enhanced activity for some applications and cost compared to noble metal competitors. As a result of these accolades, the need for attention to the synthesis methods of these materials from an industrial view is increasingly desirable. The challenge in a facile, scalable method of synthesis for binary phosphide material is control over phase, or metal to phosphorus ratio within the lattice. The phase diagrams of iron, cobalt and nickel in the presence of phosphorus present in Figure 3.2.1 show the potential phase compositions of binary phosphides as a function of temperature and atomic percent phosphorus. Phases below 400°C are only observed due to the desire to synthesize these phosphides via wet chemical syntheses.

The phase diagram for cobalt and phosphorus containing complexes is the simplest of the three binary phosphide systems. Only two primary phases are stable below 400°C and are separated by a large enough phosphorus composition to make phase control easily attainable by adjusting the amount of phosphorus available for intercalation. While iron has more

potential phase compositions for a binary phosphide possible, these too are separated by wide enough margins that were not terribly concerning. Nickel phosphide derivatives on the other hand are rather difficult to control due to the presence of a multitude of stable phases in the metal-rich realm of the phase diagram. Since metal-rich binary phosphides are more attractive for catalytic applications of varying degrees, control over synthesizing pure phase materials without incredibly tailored synthetic parameters is difficult.

Nickel phosphides are of particular interest due to the vast amount of metal-rich phases that are possible, most of which possess different crystal structures. Because of the close proximity and often overlap in phosphorus compositions and temperatures needed to attain different phases, namely Ni_3P, $Ni_{12}P_5$, Ni_2P, and Ni_5P_4, close attention must be paid to temperature and phosphorus content parameters. Still in some cases, even that is not enough to ensure pure phase synthesis of a single targeted phase. While many of these phases have shown promise as catalysts of various systems, the most noted and studied phase is Ni_2P. While Ni_2P is currently known as the most promising phase for catalysis, the other nickel phosphide phases suffer from a lack of research and experimentation with them. Some of these phases have been postulated to be intermediates to the formation of Ni_2P, however, not enough support regarding these transitions are available.
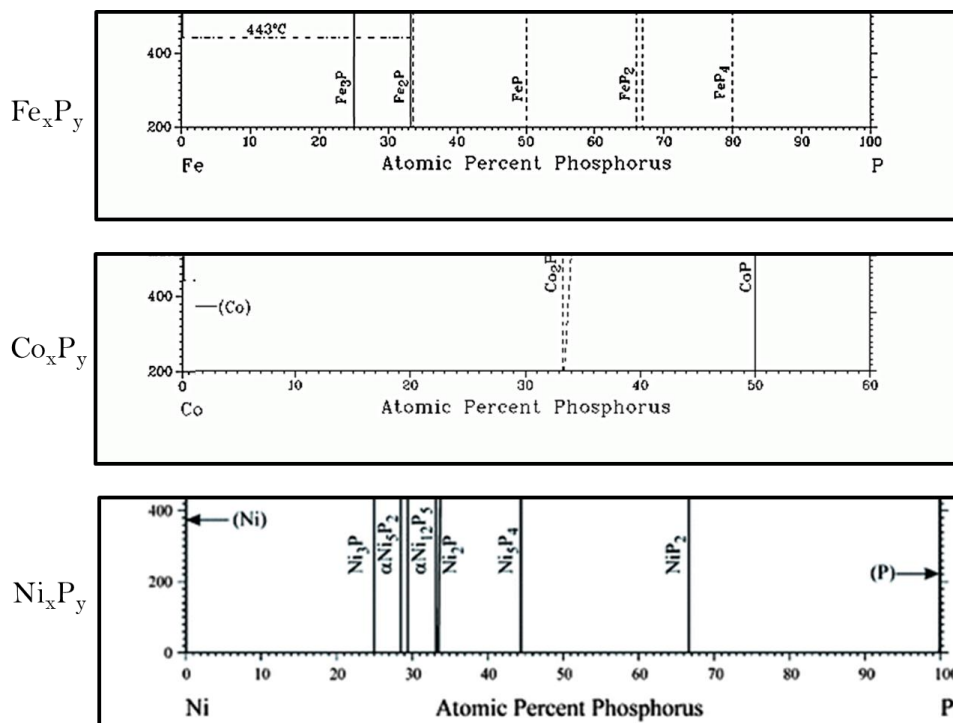
Figure 3.2.1: Phase diagrams below 400°C for Fe, Co and Ni Phosphides

Metal rich binary phosphides have attracted a great amount of attention in the catalysis world due to their promising activity at metal sites while achieving catalytic stability with surrounding phosphorus atoms to prevent catalyst poisoning and enhancing recyclability compared to purely metallic catalysts. These binary phosphides have shown activity toward hydrogen and oxygen evolution from water, hydrodesulfurization and hydrodenitrogenation of sulfur and nitrogen containing hydrocarbons in fuel sources and as high capacity lithium ion transporters for Li-ion batteries. Binary metal phosphides used for heterogeneous catalysis can be synthesized as unsupported catalyst which consist of merely particle as synthesized or supported catalysts that are typically synthesized in the presence of some sort of ordered support structure such as silica, carbon nanotubes, graphene, etc.

Typically, synthesis of supported catalysts require methods, like impregnation and organometallic routes, that require more expensive or complex precursors that must be annealed at high temperatures in the presence of the chosen support with little control over phase and particle shape and size that can be achieved using wet chemical methods. Unsupported methods on the other hand typically have better control over morphology and crystal phase of phosphide particles and display only slightly weaker activity than their supported counterparts in some cases. Development of a facile wet chemical method providing control over various phases of materials is beneficial to experiment with the possibility of post synthetic modification to add supports to synthesized nanomaterials if needed.

3.3 Experimental Methods

In a very simplified synthesis using only oleylamine (OAm) and n-trioctylphosphine (TOP) several different phases of phosphide nanoparticles, from metal rich to phosphorus rich, were synthesized. In a typical reaction, 5 mL of oleylamine and 5 mL of TOP were added to a three-neck round bottom flask and purged with nitrogen gas for five minutes. The hydrated metal (II) acetate corresponding to the specific metal of use (Fe, Co, or Ni) was added to the flask and the solution was ramped to the desired temperature using a heating mantle and variac while temperature was monitored via a digital thermometer in solution through the duration of the reaction. The ramp rate was measured to be approximately 5°C per minute and overshoot temperatures of less than 7°C were ensured. After reaching the desired reaction temperature, the solution was held at temperature for approximately one hour. A schematic of the general

reaction set-up can be found in the figure below. The solution was then removed from the heat source and cooled to room temperature naturally. Upon successful cooling the particles were washed repeatedly with ethanol and separated by centrifugation. The black particles were completely dried in a vacuum oven at 50°C.
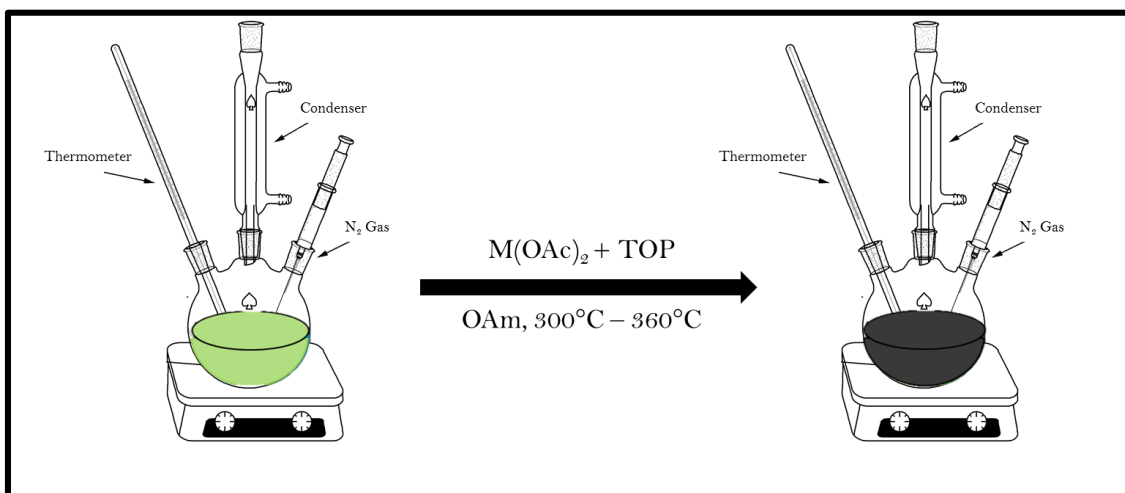
Figure 3.3.1: Schematic of Synthesis of Binary Phosphide Nanoparticles

In later experiments, conditions of the synthesis were slightly modified to provide a higher level of control or simply to test if small variations affected the phase outcome. For the system containing nickel as the metal of interest, 1-octadecene was used as a primary solvent to prevent temperatures from reaching over 310°C, while oleylamine was still utilized as a surfactant and reducing agent. Other variations included the use of triphenylphosphine (PPh$_3$) as the phosphorus source and the use of NiCl$_2$ as the metal precursor.

3.4 Results and Discussion

3.4.1 Fe_xP_y

Iron phosphide nanoparticles follow the same general trend as the cobalt phosphide particles. FeP is easily synthesized at higher temperatures and only a mixed phase was attained when lowering the P: Fe ratio and decreasing the temperature. A difference in between the syntheses of the iron and cobalt phosphides is that the mixed phase of Fe_2P and FeP were only seen if the temperature was spiked to 350°C for a few minutes and then reacted for the remainder of the reaction time around 300°C. Running a reaction just at 300°C or 320°C did not give any signal at the 100% peak for Fe_2P. Figure 4 shows the difference in morphology when going from the mixed phase Fe_2P/FeP (A) to the pure phase FeP particles (C). It has been reported in the literature that the metal rich phosphide phases of Co and Fe in particular (Fe_2P and Co_2P) tend to form rod or wire-like structures.

Figure 3.4.1.1 shows the SEM (A) and TEM (B) images of Fe_2P/Fe_3O_4 and FeP respectively. Since Fe_2P was not obtained in pure phase without another phase to grow off of, images of 200-300 nm Fe_3O_4 spheres with small wire-like Fe_2P structures can be seen in the SEM images. FeP particles on the other hand are easily synthesized at high temperatures with an excess of TOP and form spherical particles with small voids in the center. These voids are likely a result of the Kirkendall effect that occurs at the nanoscale and will be discussed later in this text.
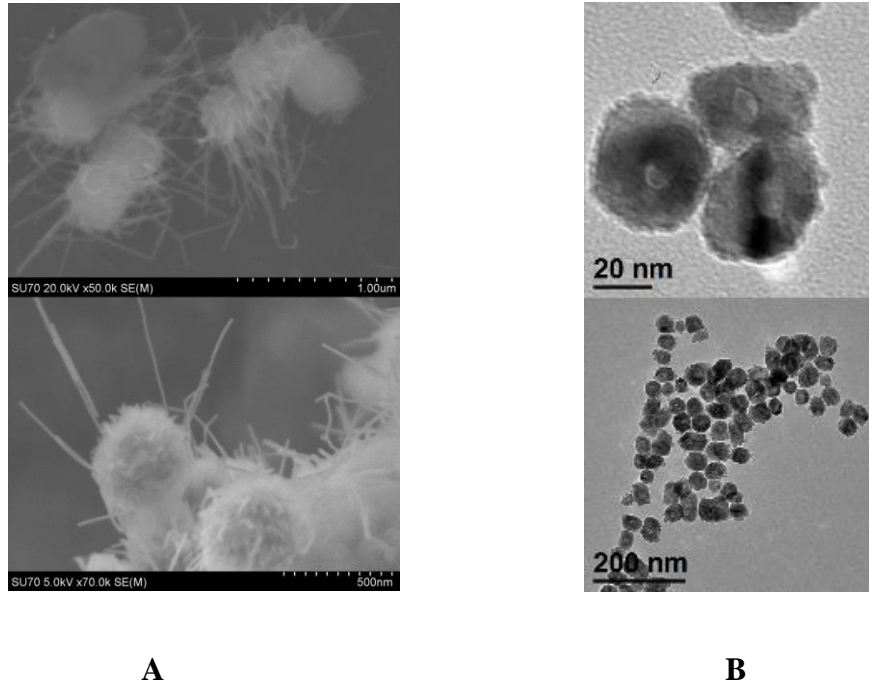
Figure 3.4.1.1: (A) SEM images of mixed phase Fe$_2$P/FeP nanoparticles. (B) TEM images of hollow FeP nanoparticles.

The formation of different iron phosphide phases mainly occurs with a change in temperature. Phosphorus rich iron phosphide (FeP) is formed at high temperatures while a mixture of phosphorus rich and metal rich phases form at 330°C (Fe$_2$P/FeP) and metal rich phosphide (Fe$_2$P) in the presence of iron oxide is formed at low temperatures or lower P:M ratios. Figure 3.4.1.2 shows the phase differential with temperature variance. This general trend is also seen with cobalt phosphide in the next section but is not the case for binary nickel phosphides.
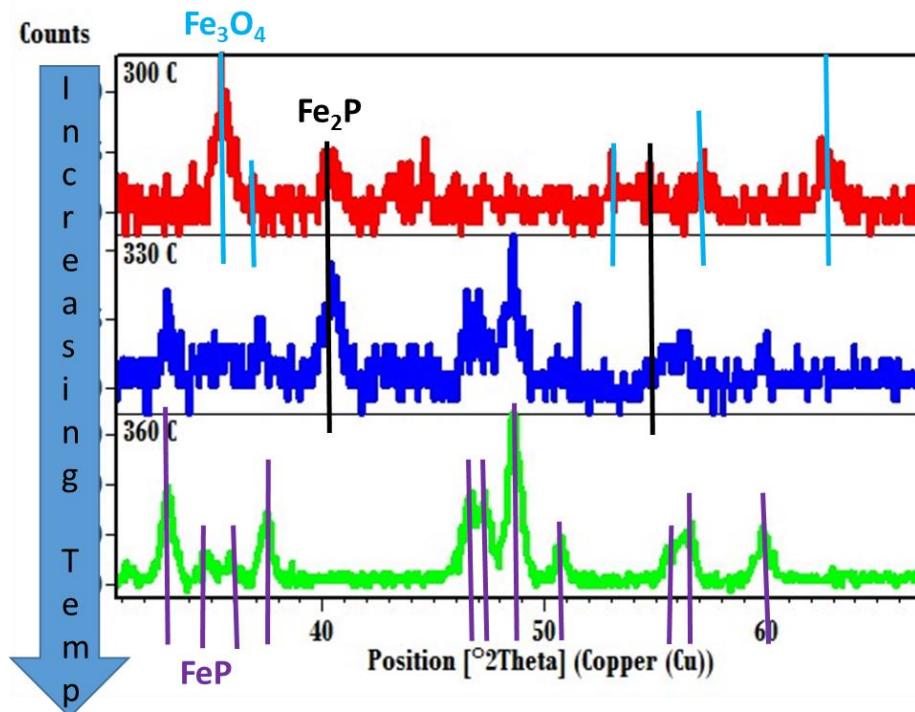
Figure 3.4.1.2: X-ray Diffractograms of Transition from Fe$_2$P to FeP with Increasing Temperature

3.3.2 Co$_x$P$_y$

Under the same general synthetic conditions, using cobalt (II) acetate hexahydrate, TOP, and OAm, phases of Co$_2$P and CoP were generated. While pure phase CoP is easily synthesized using the above components with a P: Co ratio of 10:1 at reflux for 1 hour, Co$_2$P was not as easy to isolate. As the ratio of P:Co was decreased to 3.4: 1 or the temperature was lowered to 300°C thus limiting P available, samples containing a mixed phase of Co$_2$P and CoP were detected. When the ratio was decreased further to 2:1, pure phase CoO was made. Further investigation on the temperature and duration

of the reaction will need to be conducted to pinpoint the parameters for synthesizing a

pure phase of Co_2P in this system.
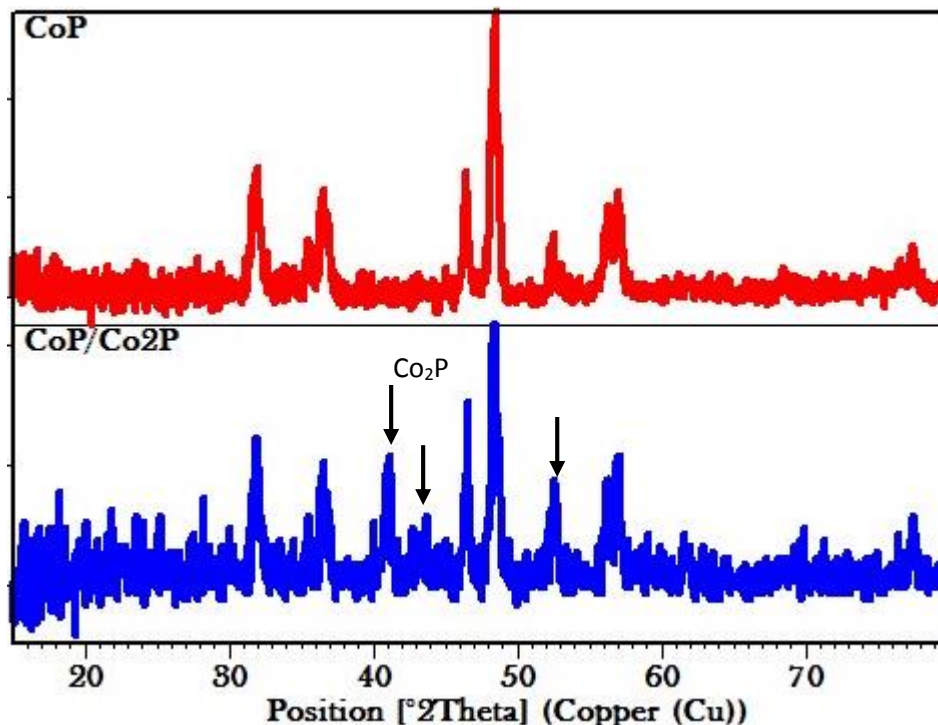
Figure 3.3.2.1: XRD Data of CoP at 360°C and Co_2P/CoP at 300°C

3.3.3 Ni_xP_y

Nickel phosphides are easily synthesized in many phases compared to their iron

and cobalt counterparts. The isolation of each phase individually using a wet chemical

approach has proven challenging but not impossible. Two approaches were tested for

the development of nickel phosphide: the thermal decomposition of a single precursor

containing both Ni and P in OAm and the reaction of a nickel precursor and separate P

source in OAm, both at elevated temperatures. For the first method, a Ni and P

containing precursor was synthesized by reacting $NiCl_2$* $6H_2O$ with 1,5-

bis(diphenylphosphino)pentane using a 1:2 ratio in gently heated (~60°C) ethanol. The

dried precursor was then added to OAm at room temperature and ramped to the

appropriate temperature. Iterations were carried out at 370°C (reflux) and 330°C. In

both cases Ni_2P was synthesized, however, the reaction carried out at 370°C also

produced NH_4Cl, while the other product at 330°C was $Ni_{12}P_5$. The presence of salt

deters the use of this single source precursor due to the probability of forming the salt

impurity which could have an effect on reaction kinetics and further complicate the

system. Also further characterization would need to be carried out to ensure the purity

of the precursor synthesized. Eliminating the single source precursor also takes out

another added step to the synthesis process and thereby eliminates another variable.

Using a phosphorus source and nickel source as separate precursors in

oleylamine led to no salt formation and the formation of a phase not seen when using

the single source precursor, Ni_5P_4. For this study, nickel (II) acetate tetrahydrate

($Ni(OAc)_2 \cdot 4H_2O$) was used as the nickel source, n-trioctylphosphine (TOP) was used as

the phosphorus source and oleylamine acted as the capping agent, reducing agent and

solvent. In initial studies with respect to temperature, the amount of TOP and nickel

acetate added were kept constant at 5 mL (11 mmol) and 265 mg (1 mmol) respectively.

When conducting the exact same reaction at different temperatures for one hour, it was

found that two different phases were capable of forming depending on the temperature

at which the experiment was conducted. Figure 3.3.3.1 shows that pure phase Ni_2P is

formed at lower reaction temperatures (300°C) while pure phase Ni_5P_4 is formed at

higher temperatures (360°C). At temperatures between 330-350°C under the same

reaction conditions, mixtures of Ni_2P and Ni_5P_4 are observed. The effect of temperature on phase of nickel phosphide generated can be attributed to the liberation of more phosphorus from TOP with increasing temperature. The presence of greater amount of phosphorus allow for the formation of phosphide phases whose Ni: P ratios are closer to one.
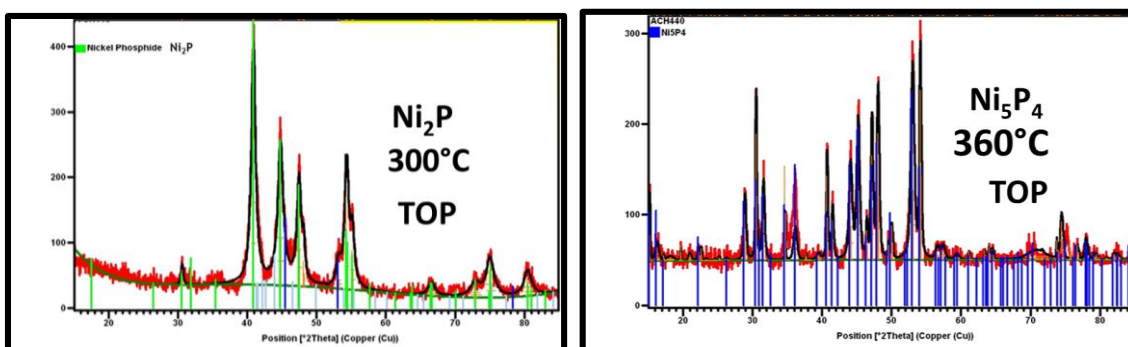
Figure 3.3.3.1: XRD Data of Pure Phases of Ni₂P and Ni₅P₄ with Temperature Variation

A   **B**
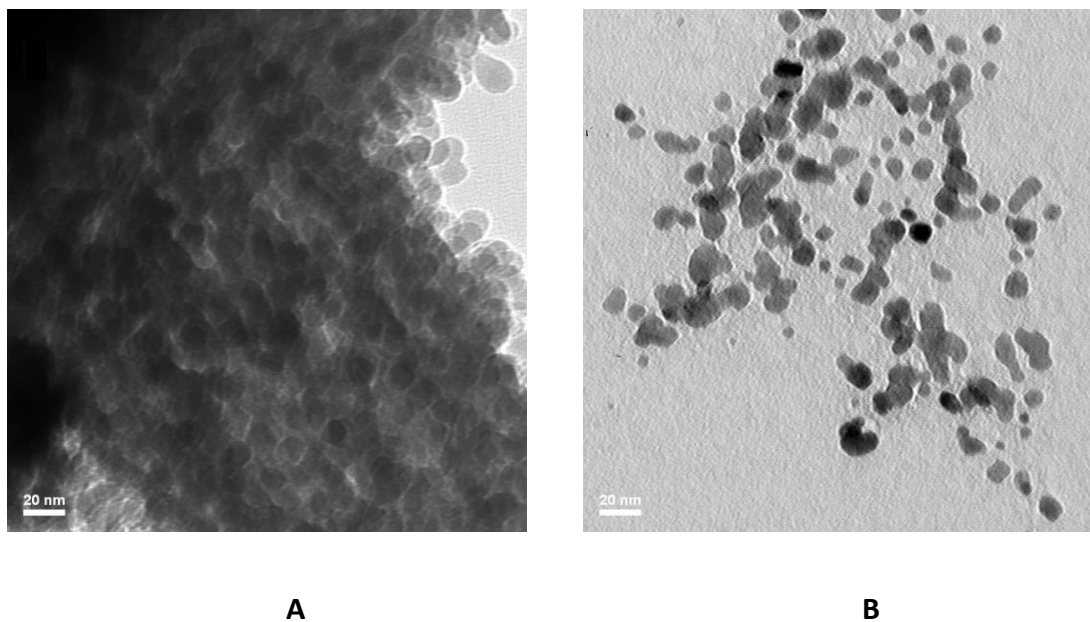
Figure 3.3.3.2: TEM Images of (A) Ni₂P Nanoparticles and (B) Ni₅P₄ Nanoparticles

To affirm that and increasing amount of phosphorus did indeed play the main role in change in nickel phosphide phase, the amount of TOP added to the reaction was varied and studied. This set if reactions was carried out at temperatures where it was possible for both Ni_2P and Ni_5P_4 phases to be present, 340°C. Starting with 0.5 mL of TOP (1 mmol) and conducting subsequent experiments that increase the phosphorus to nickel ratio to 5:1, 11:1 and 22:1. Figure 5.3.3.3 shows the XRD diffractograms that show Ni_2P at a ratio of 1:1 and an increasing amount of Ni_5P_4 formation with higher amounts of TOP when observing the data from top to bottom. This data coincides with the previous temperature study affirming that phosphorus availability significantly affects crystal phase formed.
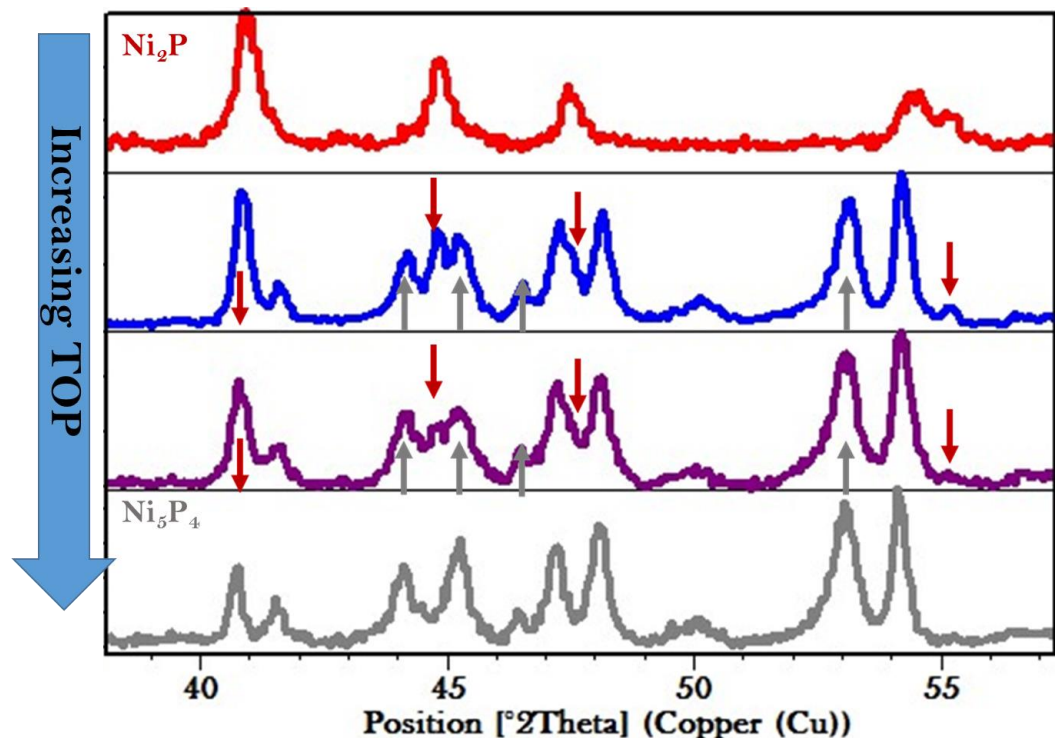
Figure 3.3.3.3: XRD Data of Transitions from Ni₂P to Ni₅P₄ with TOP

Pure phases of both of these nickel phosphides were synthesized multiple times by repeating the same general synthesis showing reproducibility if temperature is appropriately monitored. Due to the multitude of metal-rich phases of nickel phosphide attainable in lower phosphorus environments, a slightly modified system was tested to better control temperature at a lower value and make it easier to control smaller amounts of phosphorus introduced into the system. In order to ensure the reaction temperature was easily kept at a level friendlier to metal-rich phases, 1-octadecene was used as the primary solvent due to its lower boiling point of 315°C. Because TOP is a viscous liquid at room temperature, using it as a phosphorus source while trying to achieve smaller amounts introduced into the reaction can be more difficult to monitor when using liquid reactants compared to powders that can easily be weighed. For this reason, triphenylphosphine (TPP) was used as the phosphorus source

Once this modified system was implemented, reactions were carried out with octadecene as the solvent, olelyamine as the reducing agent and surfactant, nickel acetate as the nickel precursor and TPP as the phosphorus source. Using nickel acetate and a 1:1 Ni: P ratio at 310°C produced a different phase nickel phosphide than the previous system, $Ni_{12}P_5$. Under these conditions, this material was produced easily in a pure phase and is a more metal-rich phase than Ni_2P and Ni_5P_4. Some experiments by other groups have suggested that $Ni_{12}P_5$ is a precursor to Ni_2P, however upon conducting longer reaction times under the same conditions, that hypothesis does not appear to hold validity in this system. As displayed in Figure 3.3.3.4, no change in crystal phase was observed when conducting the same experiment for longer reaction times.

Pure phase $Ni_{12}P_5$ is still easily formed from one hour to three hours with no appreciable change in crystal phase, morphology or size.
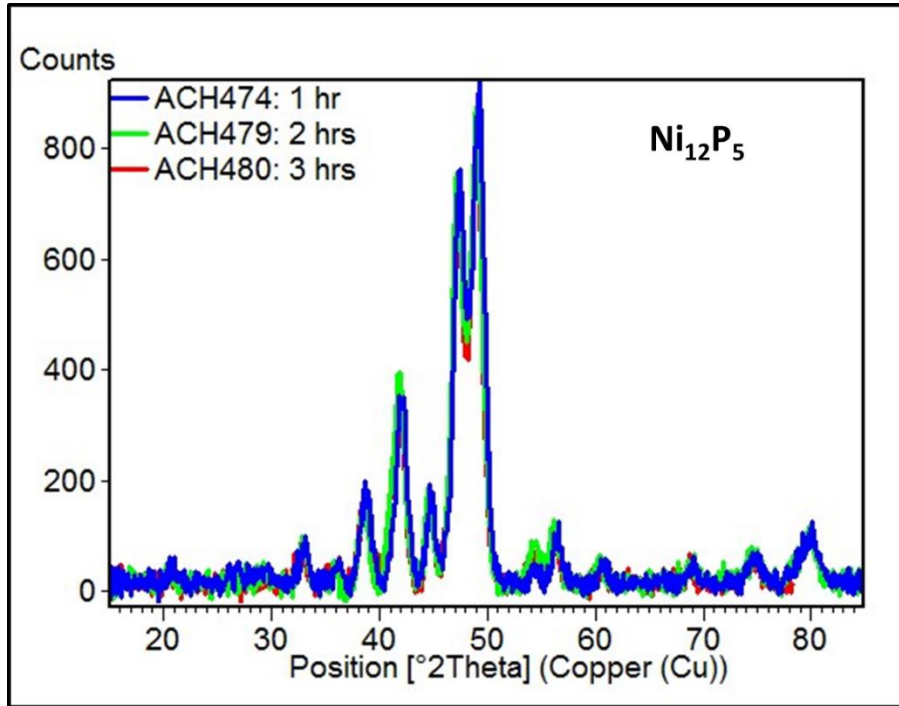
Figure 3.3.3.4 XRD Study of Effect of Time of Phase

One last study to observe phase changes of nickel phosphide materials was to change the precursor used with the aforementioned method using TPP. By simply changing the precursor from nickel acetate tetrahydrate to nickel chloride hexahydrate, a different metal-rich phase was easily synthesized. Pure phase Ni_3P is formed when reacting nickel chloride in the same exact system as discussed above which yielded $Ni_{12}P_5$. Unlike the stability of $Ni_{12}P_5$ upon implementing longer reaction times, Ni_3P is not the only phase found when slightly longer times are applied. Figure 3.3.3.5 shows formation of $Ni_{12}P_5$ with increasing reaction time. The

formation of Ni₃P upon changing precursor from nickel acetate to nickel chloride is believed to

be caused by slower kinetics when using the chloride precursor.
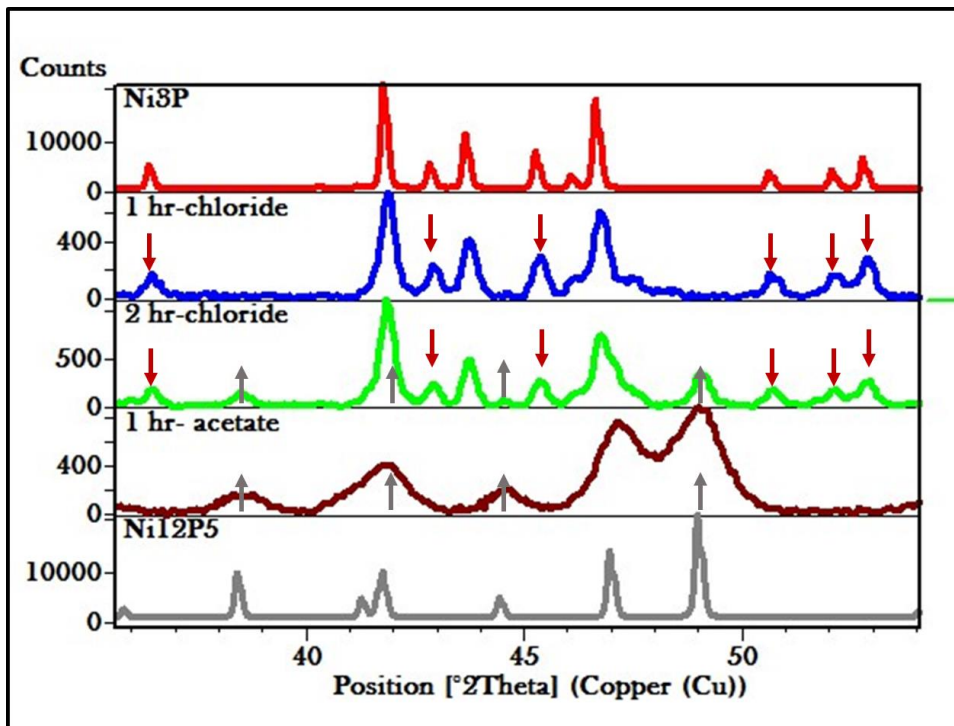
Figure 3.3.3.5: XRD Data of Phase Composition vs. Metal Precursor
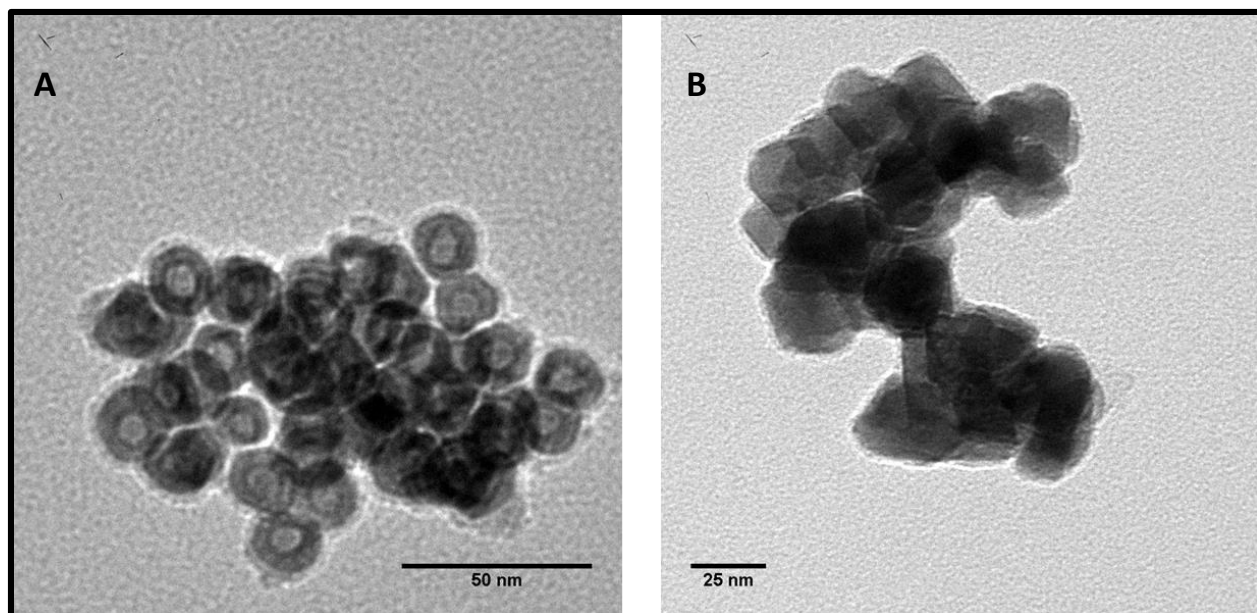
Figure 3.3.3.6: TEM Images of (A) Ni$_{12}$P$_5$ Nanoparticles and (B) Ni$_3$P Nanoparticles

Ni$_3$P will likely form Ni$_{12}$P$_5$ with longer reaction times at a P: Ni ratio of 1:1 given the above data. In order to persist formation of the metal-rich Ni$_3$P phase with increasing time, the amount of phosphorus available in solution likely needs to be reduced to a ratio closer to that of the phase's chemical formula (Ni:P = 3:1). Due to the high probability that all of the nickel precursor added to the reaction is not 100% converted into zerovalent nickel metal to be available for subsequent reaction with the neighboring phosphorus source, the ratio added is likely not that which persists throughout the reaction. Phosphorus availability increases with temperature and time while metal availability is likely not equal to the amount that was initially added. It is also possible that all of the phosphorus added is not used as a phosphorus source, but rather some is used as a co-surfactant. It does appear that from previous studied that phosphorus liberation increases with temperature. This makes it plausible for phases formed to not match identically with precursors initially added.

51

3.5 Conclusion

Binary phosphides were successfully synthesized using oleylamine as a reducing source and in cases of using TOP or TPP as a phosphorus source. Ample phase control was achieved even with an excess of phosphorus compared to the stoichiometry within a given phase's formula through temperature, phosphorus source or precursor control. As a general trend, phases produced at higher temperatures were more phosphorus rich compared to those synthesized at lower temperatures with the same amount of phosphorus source in solution. When dealing with the more complex system of nickel phosphide, control was still achieved by altering the precursor or phosphorus source in addition to temperature. Four different pure nickel phosphide phases, Ni_2P, $Ni_{12}P_5$, Ni_3P and Ni_5P_4, were synthesized with control of simple reaction conditions. Of the binary phosphides synthesized, the most difficult phase to obtain pure phases of was M_2P when M= Fe or Co. These phases were typically low in crystallinity unless there was another crystalline material in solution to aid in the growth of M_2P particles.

Chapter 4: Synthesis of Ternary Phosphide Materials: CoNiP and FeCoP

4.1 Motivation

While binary phosphides are useful as catalysts as well as a multitude of other uses, ternary phosphides containing more than one metal can be useful for their unique properties as well. Ternary phosphides when compared to binary phosphides have not been extensively studied, so it is of interest to research mixed metal phosphides containing metals that have already proven affective for catalysis. Two variations using Fe, Co, and Ni were chosen based on potential magnetic and catalytic properties associated with FeCoP and catalytic potential associated with CoNiP.[28,52] The latter of these ternary phosphides has already been utilized as a highly active catalyst for hydrodesulfurization along with other ternary nickel based derivatives such as NiWP, NiMoP and NiFeP. Further investigation into synthetic methods of ternary phosphides materials as well as their activities and properties is needed.

4.2 Introduction

Ternary phosphide materials are composed of three elements and usually involve two metals and phosphorus. When combining metals within a single structure, it is important to make sure the metals used are similar enough to be incorporated into the lattice of the other material. Phases of the type M_2P were chosen due to the ability of binary phosphides containing Co, Ni and Fe to form solid solutions with one another. The resulting mixed metal system has a formula of $M1_{2-x}M2_xP$ where metal 1 (M1) and metal 2 (M2) have different identities. The combination of metals that yield ternary phosphides can have many advantages and display interesting magnetic, catalytic and semi-conducting properties. It is often speculated that a synergistic effect can occur with ternary phosphides when combining two

active binary phosphide phases. This synergy in activity is said to originate from the presence of active catalytic metal sites that occupy more edge-like positions and make them available for higher interaction without sacrificing stability.

Observations of structural similarities and difference between phases of interest is important to ensure compatibility between the mixture of Co and Ni into a ternary phosphide material and Fe and Co into a ternary phosphide material. The former combination in the form of CoNiP has been synthesized previously and has displayed high activity for hydrodesulfurization (HDS) catalysis. In some cases the ternary phosphide has proven to be more active than its Co and Ni binary materials and in other cases the binary phases possess higher activity for HDS. The activity of this ternary phosphide material however, has not yet been tested against cobalt phosphides and nickel phosphides for activity with respect to the hydrogen evolution reaction (HER). Combinations of iron and cobalt to form ternary phosphide phases have been even more scarcely reported than those with cobalt and nickel.

When observing the crystal structures of the M_2P phases of interest, it is seen that Fe_2P and Ni_2P both possess hexagonal crystal structures while Co_2P is orthorhombic. Of these three structures, Fe_2P is the only phase that in ferromagnetic in nature. Based on this information, by initial inspection it would appear that Ni and Fe phases can create ternary phases effectively, but ternary materials combining Co and Ni and Fe and Co would be less successful based on structural differences. However, upon further inspection of the two crystal structures, it is seen that along the [001] direction of the hexagonal structure and the [010] direction of the orthorhombic structure, phosphorus atoms form tetrahedral and square based pyramids alternatively.

As seen if Figure 4.2.1 A, these alternating geometries form a canal of triangular cross

sections. Due to the inability of both canals to be occupied simultaneously, two types of canals

are possible, those with only tetrahedral sites occupied and those with only pyramidal sites

occupied. However, in both hexagonal Fe_2P and orthorhombic Co_2P geometries, canal pairs are

capable of forming as a result of both types of canals sharing common square pyramidal bases

(Figure 4.2.1 B). These pairs create a series of structural units or subcells that are rhombahedral

in nature and consist of an occupied tetrahedron-occupied pyramid pair and an empty

tetrahedron-empty pyramid pair. This subcell can be visualized in Figure 4.2.1 C.[53] The

hexagonal structure of Fe_2P results from a hexagonal arrangement of the rhombaheral subcells

while the orthorhombic structure of Co_2P results from a zig-zag stacking of the subcells as seen

in Figure 4.2.2 A and B respectively.
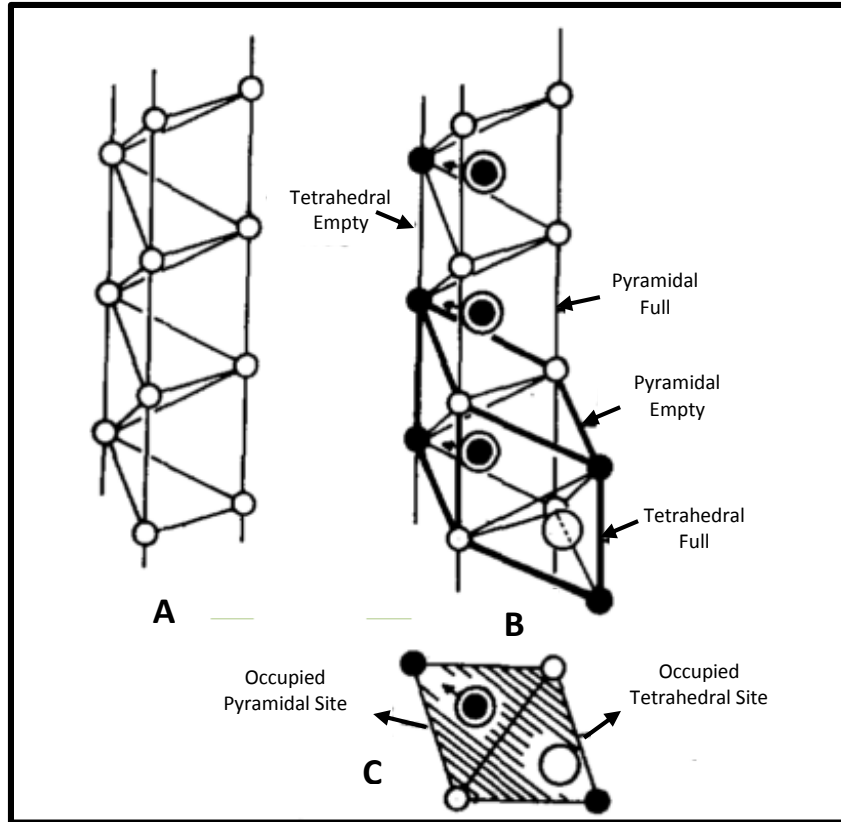
Figure 4.2.1: Building Blocks of Hexagonal and Orthorhombic M$_2$P Structures. (A) Phosphorus Canals (B) Relationship of pyramidal and tetrahedral sites form a rhombahedral subcell (C) [53]
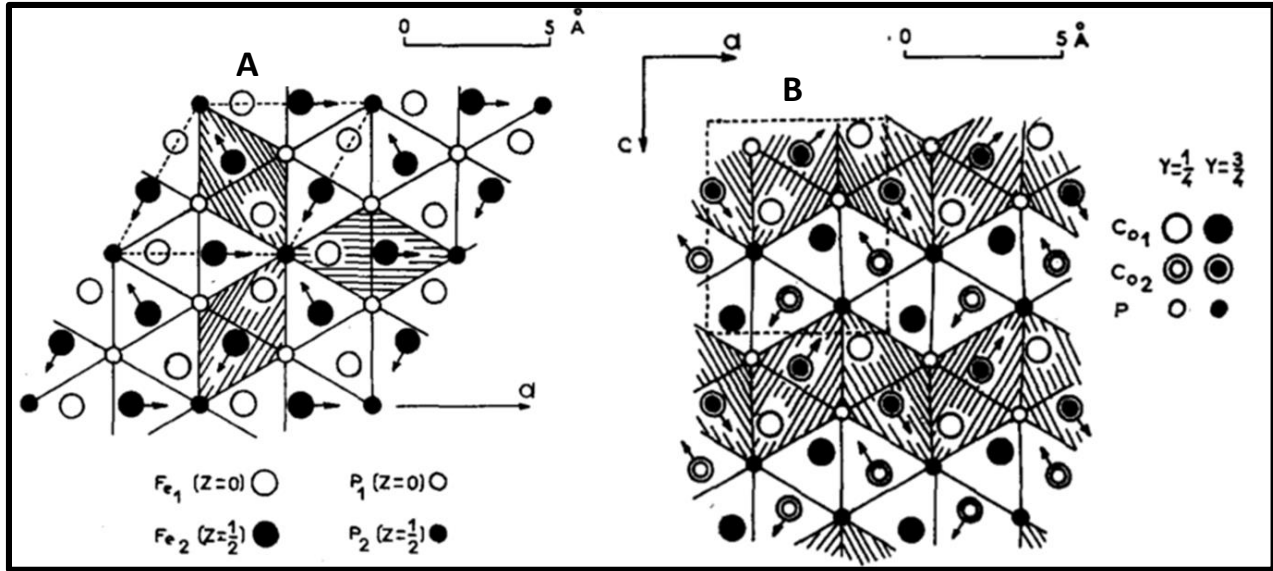
Figure 4.2.2: Stacking Arrangements of Rhombahedral Subcells for (A) Fe₂P and (B) Co₂P [53]

These crystal structure similarities allow for the formation of mixed metal ternary phosphides between binary phases or Fe_2P, Co_2P and Ni_2P. While both stacking arrangements cannot be occupied simultaneously, there is likely a threshold of metal ratios that dictates the structural arrangement of the stacking taking place in the synthesized ternary phosphide. An abundant amount of research is still needed to identify whether ternary phosphides possess an advantage over binary phosphides for a multitude of applications that binary phosphides are heavily being synthesized and researched for.

4.3 Experimental Methods

Preliminary experiments using metal acetate and oleylamine were conducted to ensure that metal alloys could indeed by synthesized under the mild reducing conditions of solely oleyamine, some of this data can be found in Appendix A. While the synthesis of ternary phosphides is very similar to the method of synthesizing binary phosphides from Chapter 3, the

phosphorus source is added separately after a desired temperature is reached. Figure 4.3.1

shows a schematic of the reaction conditions for ternary phosphide materials in which metal

acetates of chosen metals totaling 1 mmol (either Co and Ni or Fe and Co) were reacted with 5

mL of oleylamine at 300°C for a small amount of time. Variations of Co: Ni were made while

keeping the overall metal content constant at 1 mmol. Formation of metal nanoparticles was

typically assessed by the attraction of the greyish/black nanoparticles to the stir bar within the

flask causing the solution to become more transparent. Upon the observation of metal

nanoparticles, the phosphorus source, in one case TOP was added to the solution at 300°C. The

solution was aged for one hour after TOP addition at 330°C, cooled to room temperature,

washed with ethanol and separated via centrifugation.
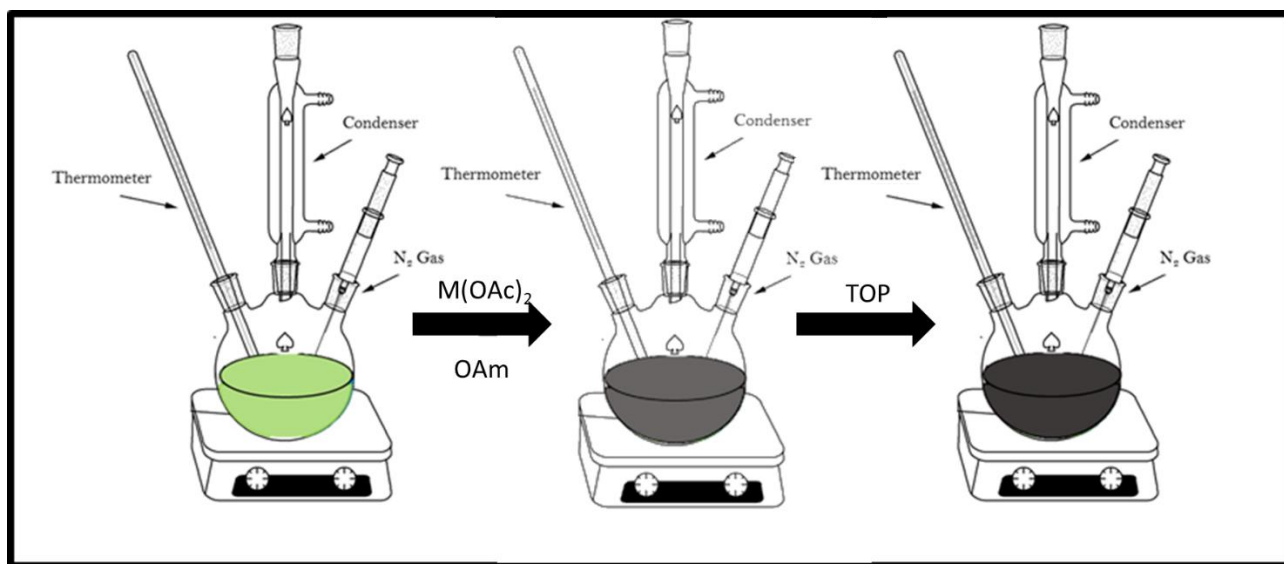
Figure 4.3.1: Schematic of Mixed Metal Phosphide Synthesis

Slight modifications were made to this synthesis to test the effect on phosphorus source by replacing TOP with PPh_3 and the addition to 1-octadecene to oleylamine to control the temperature more effectively to stay less than 310°C.

4.4. Results and Discussion

4.4.1 CoNiP

When cobalt and nickel acetates were reacted with oleylamine and subsequently a hot addition of trioctylyphosphine, mainly CoNiP was formed no matter the ratio between cobalt and nickel precursors initially added as long as the temperature was kept below 315°C. Figure 4.4.1.1 shows XRD data of iterations conducted at temperatures between 300°C and 315°C with an excess of TOP (P:M = 3.4:1). Some residual CoNi metal remains in the 50:50 mixture but no other phosphide phases were present. However, if temperatures were increased above 330°C under the same conditions, CoP was formed in addition to CoNiP at different ratios of Co: Ni. Interestingly, no other phases of nickel phosphide were observed, such as Ni_5P_4, which has previously shown to develop at higher reaction temperatures from the data provided in Chapter 3.
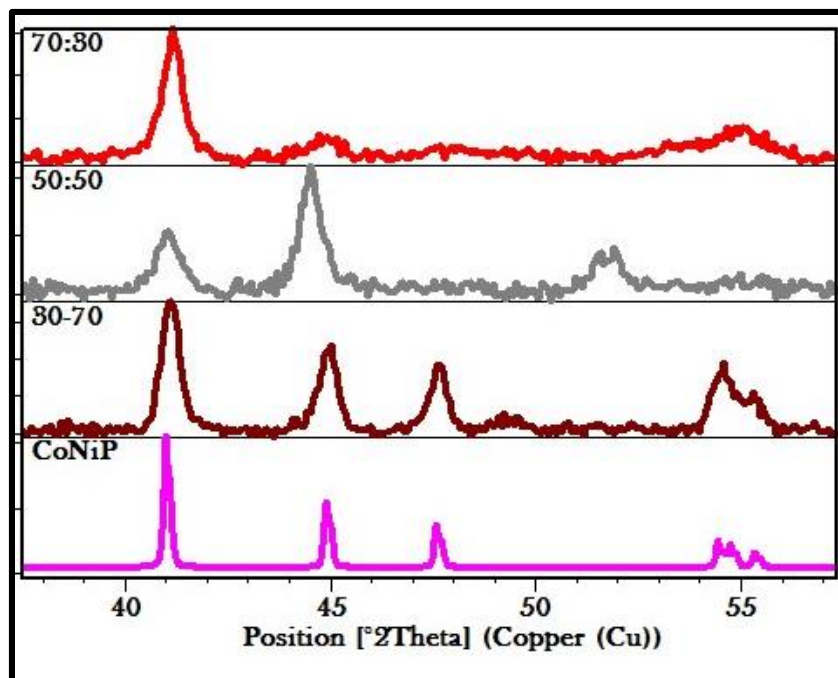
Figure 4.4.1.1: XRD Data of CoNiP at Different Co: Ni Ratios

The shape and morphology of these CoNiP nanoparticles appear to be spherical and in some cases appear hexagonal in nature and around 50-100 nm in size. These particles also possess voids in the center that take up a relatively large portion of the particle's diameter. Figure 4.4.1.2 B presents TEM images of the CoNiP particles synthesized with TOP as the phosphorus source. These particles did not appear to change much in size when varying ratios of Co: Ni metal precursors however, void sizes may have been slightly different and will be discussed further later in this section. CoNiP particles synthesized using triphenylphosphine (TPP) instead of TOP are pictured in Figure 4.4.1.2 A. These particles seem to have similar size to void ratios within their given particles, however when comparing sizes of the overall particles, the particles synthesized with TPP are considerably smaller than those synthesized with TOP.
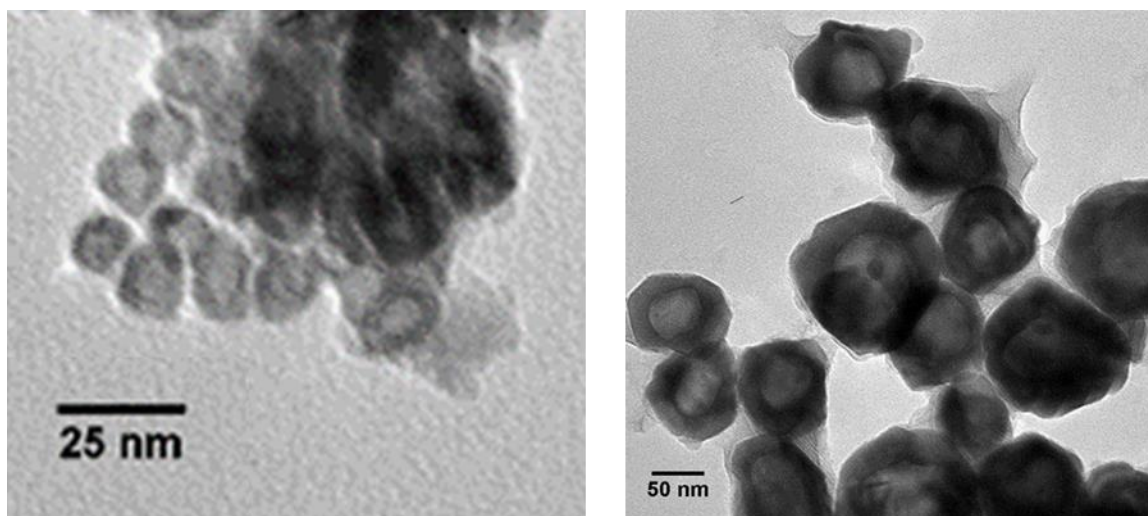
Figure 4.4.1.2 TEM Images of CoNiP with Co: Ni ratio of 30:70 with (A) TPP and (B) TOP

Particles synthesized using TPP have the same general shape as those made with TOP however the particle sizes were about 10-15 nm compared to the 50-100 nm particles made in TOP. In addition to smaller size, the particles made with TPP possess a more narrow size distribution leading to more overall uniform particles. When comparing the ratios of Co:Ni added initially to the reaction vs. the Co:Ni ratio measured in the product in Table 4.4.1.1, the values are in good agreement and show a deviation of less than 10% which is impressive for a one-pot reaction system using a mild-reducing source. This continuity in data is likely due to the similarities between the reduction potentials of Co^{2+} (-0.28) and Ni^{2+} (-0.25) causing them to behave similarly in the presence of oleylamine.

Table 4.4.1.1: ICP-OES Ratios of Co: Ni in CoNiP Synthesized with TPP

Sample Co:Ni- P Source	Co:Ni Added At Beginning of Reaction	Co:Ni Measured in CoNiP by ICP-OES
30:70-TOP	0.43	0.43
30:70-TPP	0.43	0.45
50:50- TPP	1	1.1

Similar to those made with TOP, the particles using TPP did not differ in phase when comparing Co: Ni ratio of precursors added at the beginning of the reaction. Figure 4.4.1.3 demonstrates the retention of crystal phase with changing Co: Ni ratio. The sample containing a higher cobalt content appears to be less crystalline in nature compared to the more Ni-rich material. This is concurrent with data seen previously in Chapter 3 with decreasing crystallinity in the Co_2P and Fe_2P phases when compared to their CoP and FeP counterparts.
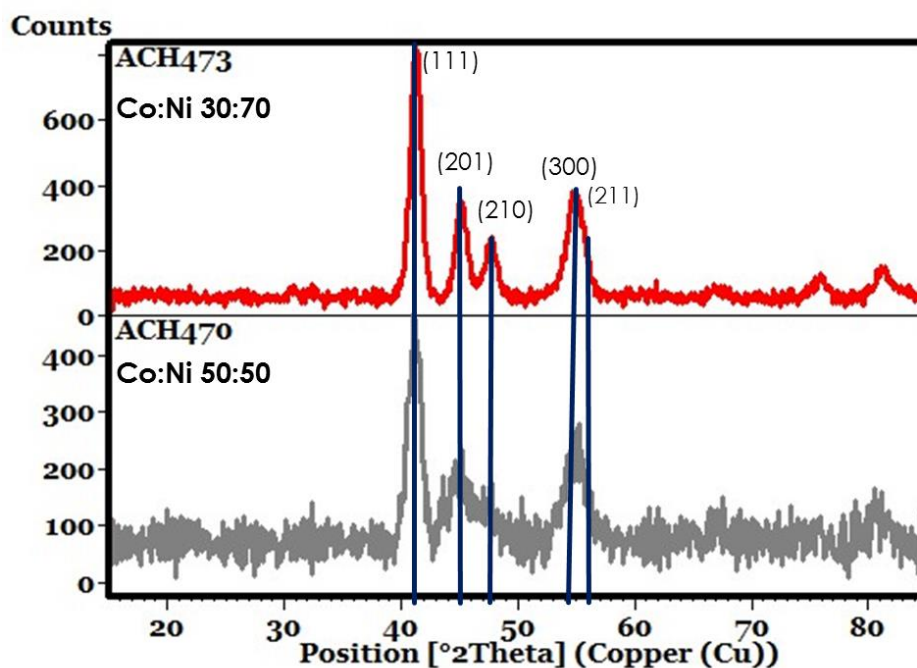
Figure 4.4.1.3: XRD of CoNiP at different Co: Ni ratios

When observing the difference in particle size and morphology in Figure 4.4.1.4, the particles appear to be similar in size of about 10-15 nm but their center void sizes appear differ dramatically. The material with higher cobalt content has much smaller voids at the particles' centers while the Ni-rich material has voids similar to that of the particles containing the same ratio synthesized with TOP instead (pictured in 4.4.1.2 B). The abundance of cobalt in

the lattice compared to nickel may affect the diffusion rates of the metals relative to phosphorus. Since cobalt is ever so slightly larger than nickel, it likely diffuses out of the center slower than nickel particles thereby creating a smaller void.

<div align="center">

A   **B**

</div>
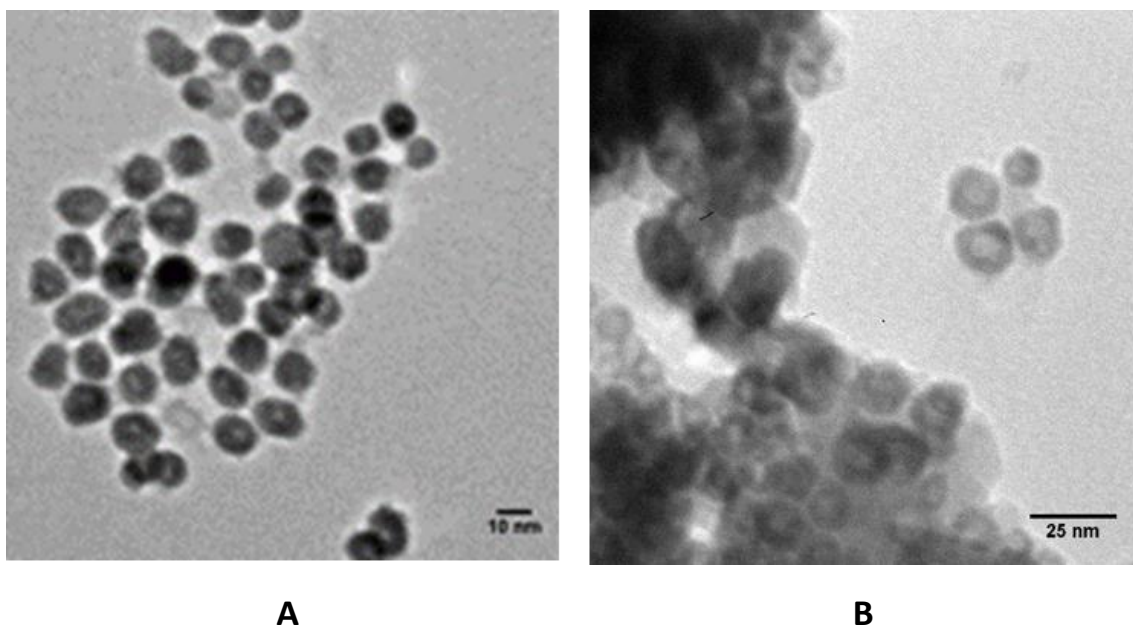
Figure 4.4.1.4 TEM Images of CoNiP at different Co: Ni ratios (A) 470-50:50 (B) 473-30:70

CoNiP nanoparticles are easily synthesized using this system with both phosphorus sources, TOP and TPP and provide relatively uniform particle with good crystallinity. Yet another transition metal phosphide, this time merging two separately active metal phosphide phases is possible. Testing of these particles is reviewed in Chapter 5 of this text.

4.4.2 FeCoP

Working with FeCoP presented itself to be the most difficult of the phases synthesized but gave the most interesting morphologies and magnetic properties. This synthetic system is identical to the schematic outlined in Figure 4.3.1 in the section above and significant research was done on the formation of the FeCo alloy in oleylamine which can be found in Appendix A of this text. Unlike nickel, which is similar to cobalt in reduction potential, iron is more difficult to reduce with a reduction potential of -0.44 compared to that of cobalt at -0.28. Iron also tends to form compounds with oxygen instead of metallic compounds if exposed to enough air.

Due to the low crystallinity observed with both Fe_2P and Co_2P type phases in this wet chemical system, that lack of crystallinity continued to present itself in the X-ray diffraction results of the ternary phosphide materials. While high percentage peaks can be identified in Figure 4.4.2.1, the overall low intensity of the entire diffractogram makes it difficult to seek out other peaks due to either crystallinity or size make it difficult to identify if the phase is pure or contains other impurities. With Fe:Co ratios all around 60:40 and varying ratios of P:M, 143 containing the highest excess and 157 containing the lowest excess, XRD data does not seem to detect a significant difference in phase composition
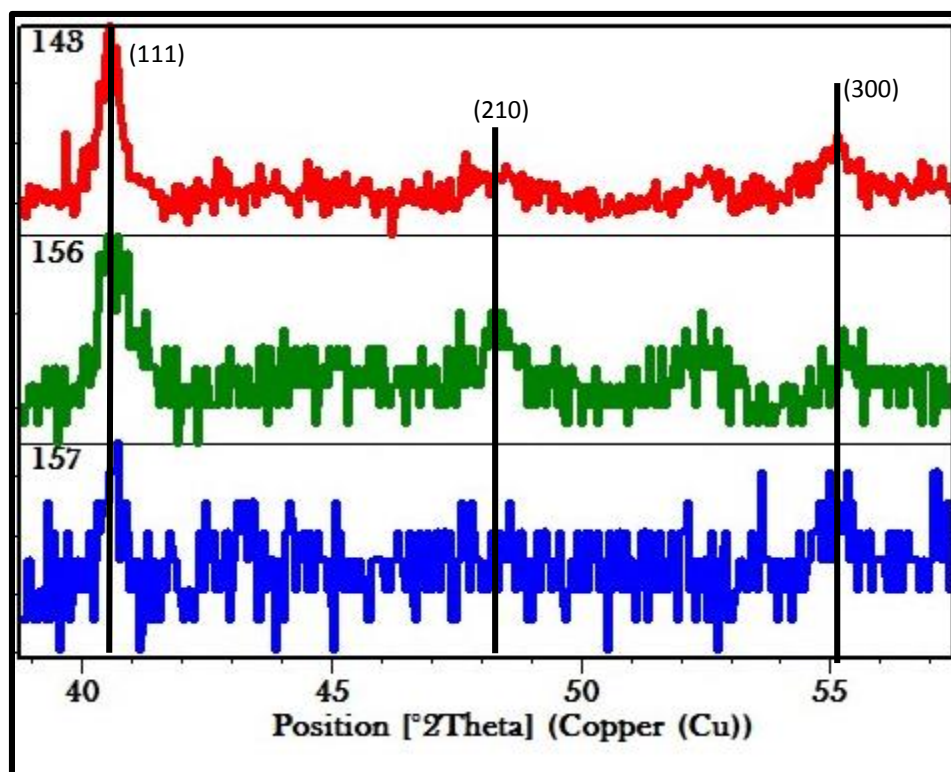
Figure 4.4.2.1: XRD Data of FeCoP

Although their phases do not appear to be significantly different, other properties of these materials differ quite a bit with no real correlation to reaction conditions like the other binary and ternary phosphide phases. The morphology changes however seem to coincide with magnetic changes seen via vibrating sample magnetometry hystereses. When comparing Figures 4.4.2.2 and 4.4.2.3, it is apparent that magnetic saturation and coercivity increase with morphology changes observed via SEM and TEM images.

Figure 4.4.2.2 A consists of more dendritic-like structures that seem to be a collection of short wire-like structures or elongated structures forming off of a spherical center. These particles possess the lowest magnetic saturation and coercivity at 10 emu/g and 200 Oe respectively. Images in part B of the same figure depict more elongated structures that appear

to be better aligned and less clustered, though still aggregated. Lastly, the TEM images in part C

depict particles presenting the best magnetic properties of the three samples with a magnetic

saturation of 45 emu/g and a coercivity of 1600 Oe which is characteristic of hard

ferromagnets.

Blue

Red

A   B   C
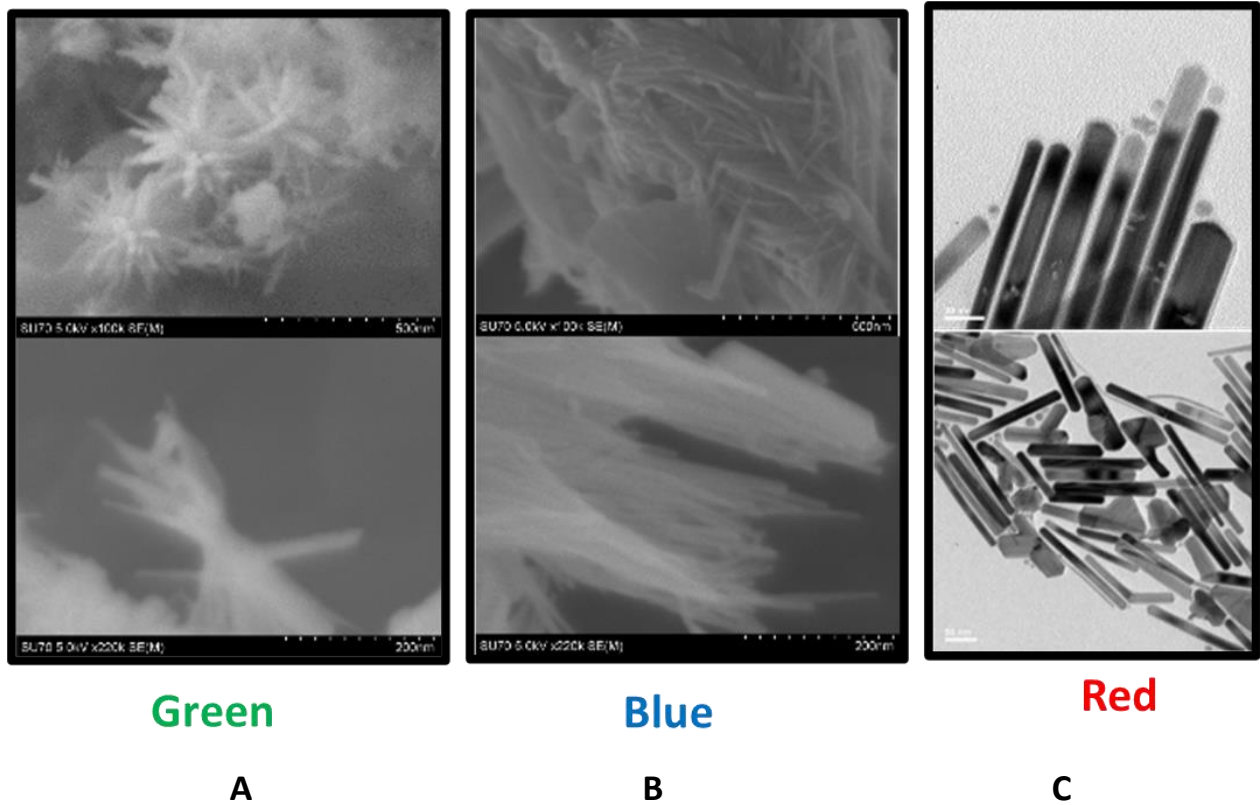
Figure 4.4.2.2: SEM Images (Green and Blue) and TEM Images (Red) of Different FeCoP Samples.

These structures are interesting for particularly their magnetic properties. When taking

a closer look at the inlay present in Figure 4.4.2.3, a kink in the hysteresis loop is noticed. This

kink is often indicative of two phases separate phases contributing to the magnetic data

measured. While this two phase characteristic appears in all of the hysteresis loops, it is easiest

to discern from the hysteresis in blue. If the natural curves of the hysteresis were followed, two

hysteresis curves could be extrapolated corresponding to the two phases. One phase would have a larger coercivity and lower saturation magnetization, while the other would have a smaller coercivity and likely a higher magnetic saturation. Since it is difficult to separate these phases magnetically and the x-ray diffractograms make it difficult to ascertain the identity of the phases present due to low crystallinity, contributions of these properties cannot be pinpointed to a particular material.
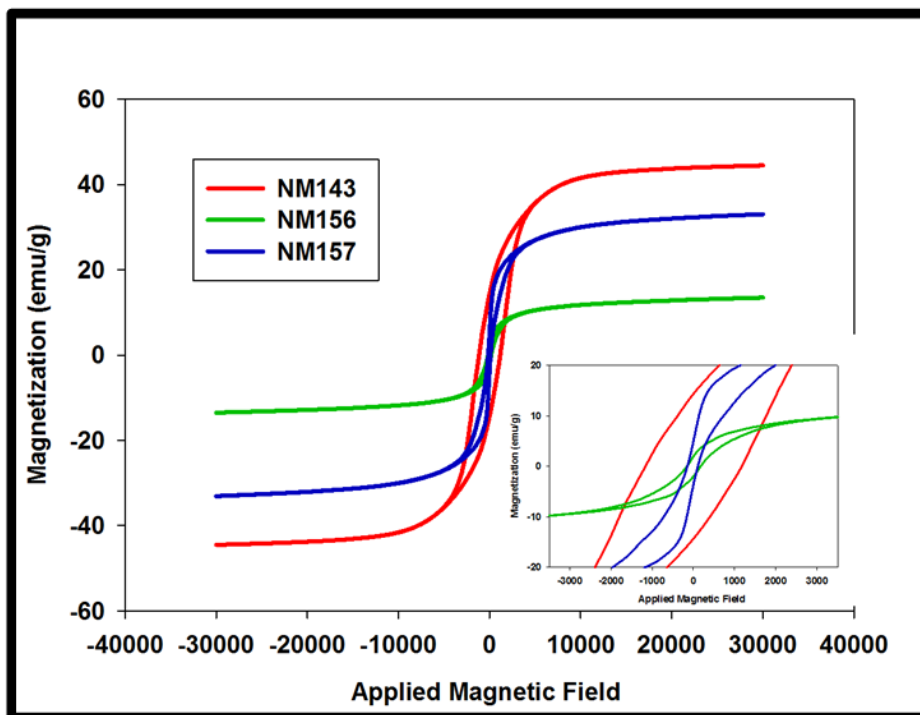
Figure 4.4.2.3 VSM Hysteresis Loops of FeCoP Samples

4.5 Kirkendall Effect

The findings from chapters 3 and 4 lead to the assumption that these metal phosphide nanomaterials are formed via the Kirkendall effect. The Kirkendall effect is a nanoscale phenomenon that occurs at the boundary between two elements as a consequence of different

diffusion rates. As seen in Figure 4.5.1, the formation of these voids seen in many of the binary

and ternary phosphides synthesized is a result of different diffusion rates. In cases where voids

are found in the center of the nanoparticle, the diffusion of metal outward is faster than the

diffusion of phosphorus inward, thus creating vacancies in the nanoparticle. Consequently, if

these diffusion rates are more equal to one another, solid particles without voids can be

observed though it is not known whether or not this is the formation mechanism for solid

phosphide nanoparticles. The likelihood of the Kirkendall effect playing a role in this synthetic

system is the formation of metal nanoparticles first in almost all cases. Typically when reactions

were run for short periods of time, metal or alloyed metal impurities were noticed in x-ray

diffraction. It is postulated that for these systems, the metal acetate precursor decomposes to

yield metal and metal oxide nanoparticles in which the metal oxide nanoparticles undergo

reduction by the oleylamine. Upon the liberation of phosphorus from a chosen phosphorus

source at high temperature, the diffusion of phosphorus into metal nanoparticles occurs

yielding either hollow or solid metal phosphide nanoparticles.
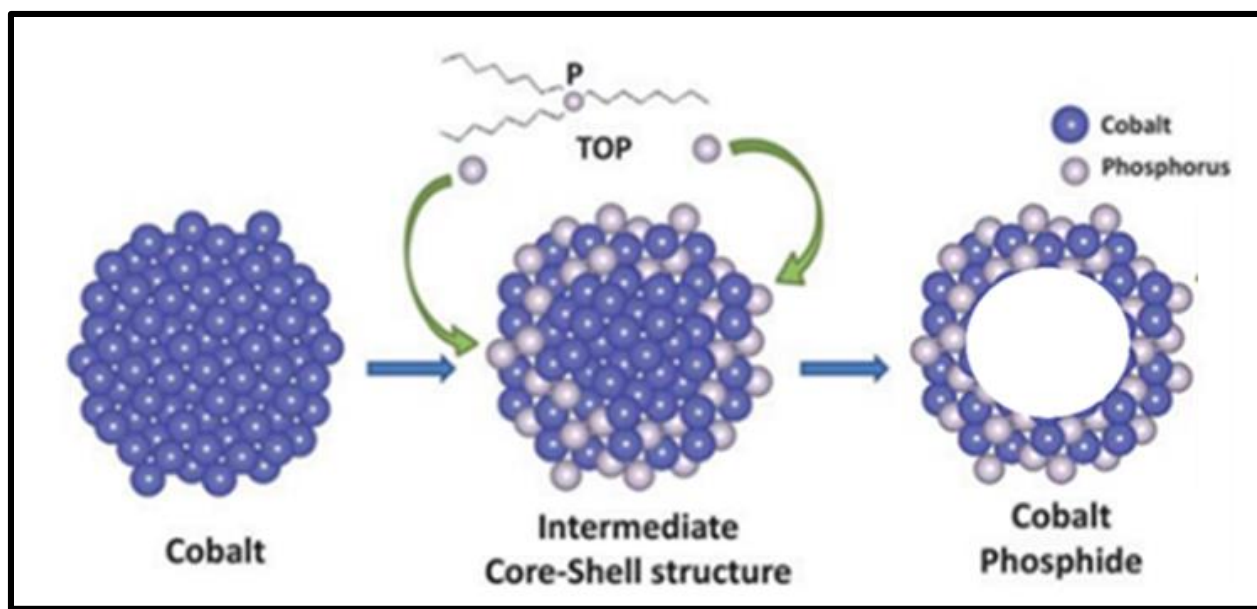
Figure 4.5.1: Schematic of the Kirkendall Effect in the Formation of Cobalt Phosphide

4.6 Conclusion

Ternary metal phosphides, like binary phosphides are also capable of being synthesized using oleylamine as a reducing source, solvent and surfactant though some compositions, particularly FeCoP, present more difficulty than CoNiP in determining phase composition and resulting properties when comparing results with reaction conditions. CoNiP nanoparticles of varying compositions all displayed hollow spherical/hexagonal morphologies and differed in size when using different phosphorus sources, and void size when testing different Co: Ni metal ratios. Some of these materials will be tested in the following chapter for their catalytic activity toward the hydrogen evolution reaction as well as their photocatalytic ability. These findings will be compared to those of binary metal phosphides containing the same metals and other literature findings.

Chapter 5: Preliminary Catalytic Studies Focused around Hydrogen Evolution

5.1 Motivation

Transition metal phosphides have recently gained copious amounts of attention for their ability to successfully catalyze the hydrogen evolution reaction, oxygen evolution reaction and a few photocatalytic reactions. Testing the activity of some of the unsupported catalysts synthesized in this work is beneficial to ascertain the potential utility of the particles made by a facile method that has promise for scalability and industrial applications. Upon demonstration of effective catalysis toward hydrogen evolution as well as photocatalytic activity, these two processes have the potential to be combined to increase performance.

5.2 Hydrogen Evolution Reaction

5.2.1 Introduction
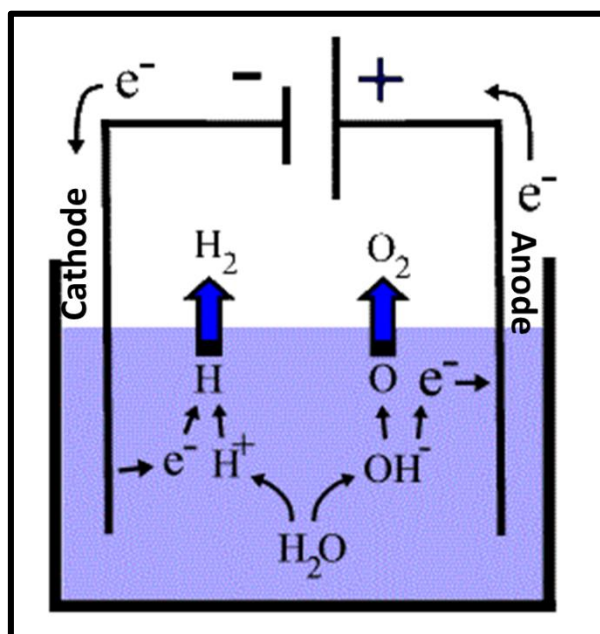
Figure 5.2.1.1: Schematic of Water Electrolysis

Water electrolysis, also known as water splitting, is an incredibly useful and promising electrolytic reaction that converts water into hydrogen and oxygen gas in the presence of a current. Hydrogen gas is generated at the cathode and oxygen gas is generated at the anode in this reaction as depicted in Figure 5.2.1.1. The electrolysis of water theoretically has the ability to generate twice the amount of hydrogen as oxygen for a single molecule of water exhibited by the balanced reaction in Equation 4. The overall electrolytic reaction is comprised of two separate reactions, the hydrogen evolution reaction (Equation 5) and the oxygen evolution reaction (Equation 6). The half reaction of most interest is the hydrogen evolution reaction due to the potential hydrogen possesses as a green, renewable energy source compared to current rapidly declining fuels used that are responsible for greenhouse emissions.

(Equation 4)
$$H_2O\ (l)\ \rightarrow H_2(g) + \frac{1}{2}O_2\ (g)$$

$$\rule{8cm}{0.4pt}$$

(Equation 5) $$(\text{HER})\quad 2H^+\ (aq) + 2e^- \rightarrow H_2(g)$$

(Equation 6) $$(\text{OER})\quad 2H_2O(l) \rightarrow 4e^- + 4H^+ + O_2(g)$$
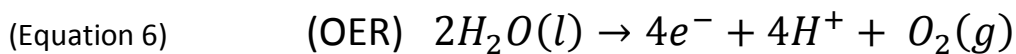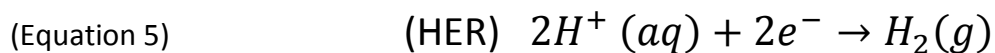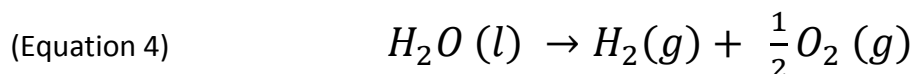
The hydrogen evolution reaction is a multistep process that is capable of generating hydrogen in two different ways depending on the reaction pathway taken. The reaction pathway taken is dependent upon the chemistry that takes place at the catalytic surface. Figure 5.2.1.2 shows a schematic of the two potential reaction pathways involved in the catalytic evolution of hydrogen. The first step during the catalytic evolution of hydrogen is

the discharge step which is also referred to as the Volmer reaction. This step involves electron transfer to the cathode to capture a proton in the electrolyte resulting in an intermediate state of an adsorbed hydrogen atom on one of the catalytic active sites. From this position the adsorbed hydrogen on the catalytic service can combine in two ways to produce hydrogen gas depending on the loading on the catalyst. If the catalyst used has low coverage of adsorbed hydrogen on its surface, the hydrogen adsorbed on the catalytic surface is electrochemically desorbed and recombines with a new electron and proton combined in the electrolyte. This is known as the Heyrovsky reaction and is associated with a measured Tafel slope of 39 mV dec^{-1}. The second pathway that can be taken via the Tafel reaction which occurs when adsorbed hydrogen on the catalytic surface is high. When catalysts possess a large amount of active catalytic sites, recombination between adjacent adsorbed hydrogen atoms is responsible for generation of hydrogen gas through chemical desorption. Catalysts following a Volmer-Tafel mechanism possess a Tafel slope of 29 mV dec^{-1}. While mechanism and obtaining the value of the Tafel slope to ascertain the chemistry taking place between the hydrogen and the catalyst, it is also important to observe how much current it requires for this catalysis to happen in the form of measuring the overpotential.
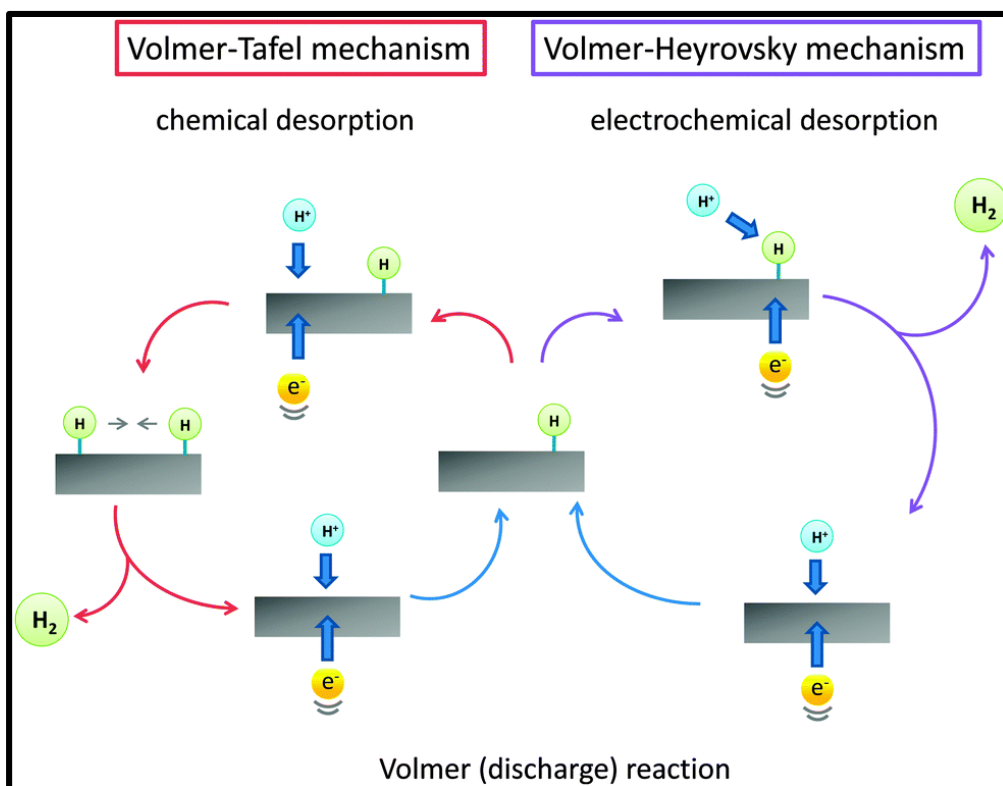
Figure 5.2.1.2: Schematic of Catalyzed Hydrogen Evolution Reaction

Regardless of the media (acidic, neutral or alkaline) that water splitting takes place in, the thermodynamic voltage of water splitting is 1.23 V at 1 atm and 25°C. This thermodynamic voltage can be lowered with an increase in temperature, however standard conditions are usually the simplest way to compare results among researchers. The overpotential is a key factor in determining efficacy of electrocatalysts for the evolution of hydrogen from water electrolysis. The overpotential is the voltage value that must be applied over the thermodynamic voltage, 1.23 V to allow for water splitting to occur. This extra voltage must be applied to overcome intrinsic activation barriers present at both the cathode and the anode, as well as other resistances due to contact or the solution.

The standard electrode potential for HER is zero at standard conditions. The value for overpotential is measured as the absolute value between zero and the onset potential required to initiate HER. The smaller this value is, the better the electrocatalyst performs. High performance catalysts with lower overpotential values essentially require less energy to achieve the same current density. While overpotential is a key measurement for determining the performance of a catalysts, other methods for evaluating an effective electrocatalyst may also be assessed.

5.2.2 Experimental Methods

In a typical catalytic experiment, a rotating disk electrode system was implemented to study the catalytic activity of binary and ternary phosphides. This three-electrode set-up included rotating disk electrode containing the loaded particles catalytic testing, a Pt counter electrode and an Ag/AgCl working electrode. A slurry containing the transition metal phosphide particles were made and placed on the end of the rotating disk composed of polytetraflouroethylene (PTFE).
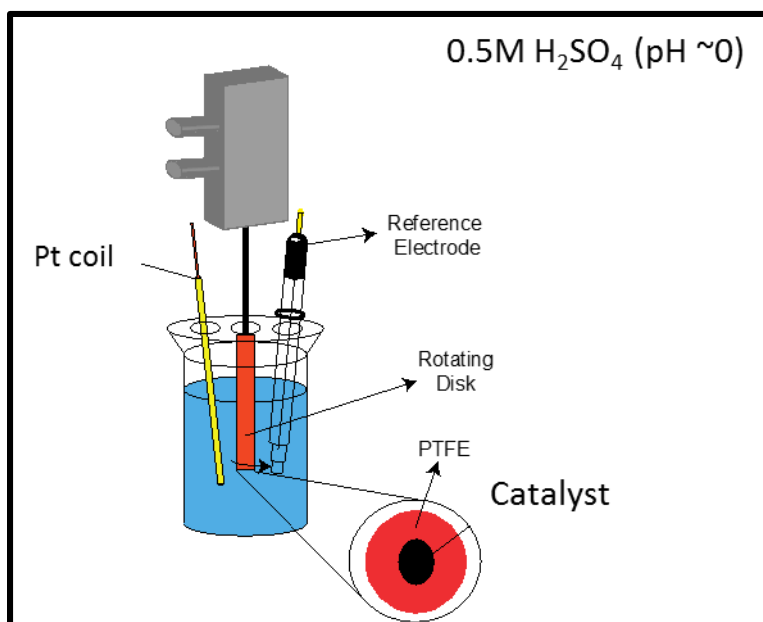
Figure 5.2.2.1: Schematic of Set-up for Catalytic HER Testing

A rotating disk was chosen for homogeneity of catalytic surface exposure to the electrolyte solution and proximity to the cathode or anode. Hydrogen evolution testing was conducted in acidic media using 0.5 M sulfuric acid as the electrolyte. The benefit of using a rotating disk electrode is to minimize concentration overpotential by stirring. Overpotential is broken down into two main forms, activation overpotential, due to the efficacy of the electrocatalyst and concentration overpotential resulting from the concentration difference of the involved ions between the solution and the electrode which is caused by slow diffusion rates of ions. This value can be partly reducing by a rotating disk electrode but can also consequently disturb the electrode reaction. Another form of overpotential is resistance overpotential that occurs on surfaces and interfaces of the measurement system and elevates actual values for overpotential. This value can be corrected by measuring and subtracting the resistance measured between the Luggin capillary and the working electrode. By multiplying this resistance value (R) by the current flowing through the system

One of the many potential applications for the cobalt and nickel binary and ternary nanoparticles developed from the oleylamine synthesis method is as catalysts for the hydrogen evolution reaction (HER). HER testing was performed in a three-electrode setup using a rotating disk electrode in 0.5M sulfuric acid electrolyte with a Pt-counter electrode and a Ag/AgCl working electrode as diagramed in Figure 5.2.1.1. Their resulting performance is shown below in Figure 5.2.3.1. The Ni_2P catalyst required the lowest overpotential, only 320 mV, to achieve a current density of 20 mA/cm^2 while the other mixed phosphides required slightly larger overpotentials, topping out around 420 mV. A clear trend was observed showing increased performance with increasing nickel content where CoNiP with a Co:Ni ratio of 70:30 shows the poorest performance. The pure Co_2P nanoparticles are not shown as their dispersions were not uniform and resulted in erroneous values. I would not be surprising however is Co_2P values were not more similar to that of Ni_2P considering research that has been conducted concluding the high catalytic activity of Co_2P nanoparticles for HER and other similar reactions.
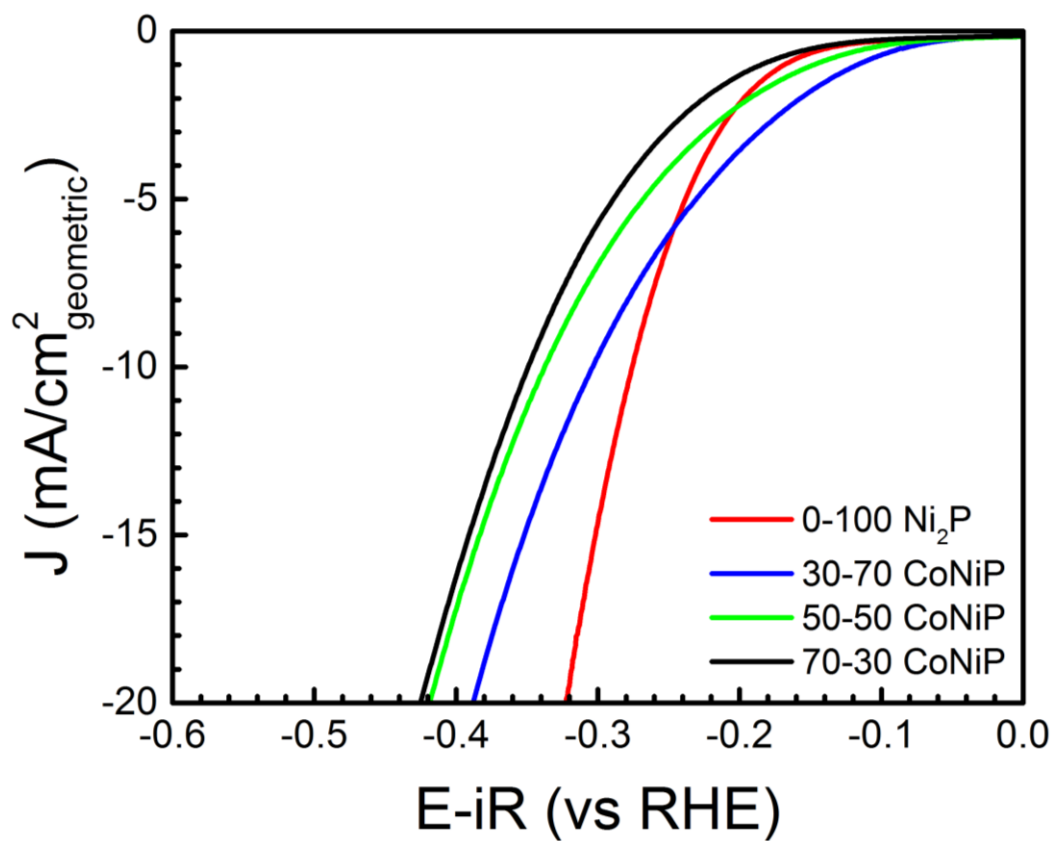
Figure 5.2.3.1: Linear sweep voltammetry results for Ni$_2$P (red), 30:70 CoNiP (blue), 50:50 CoNiP (green), and 70:30 CoNiP (black).
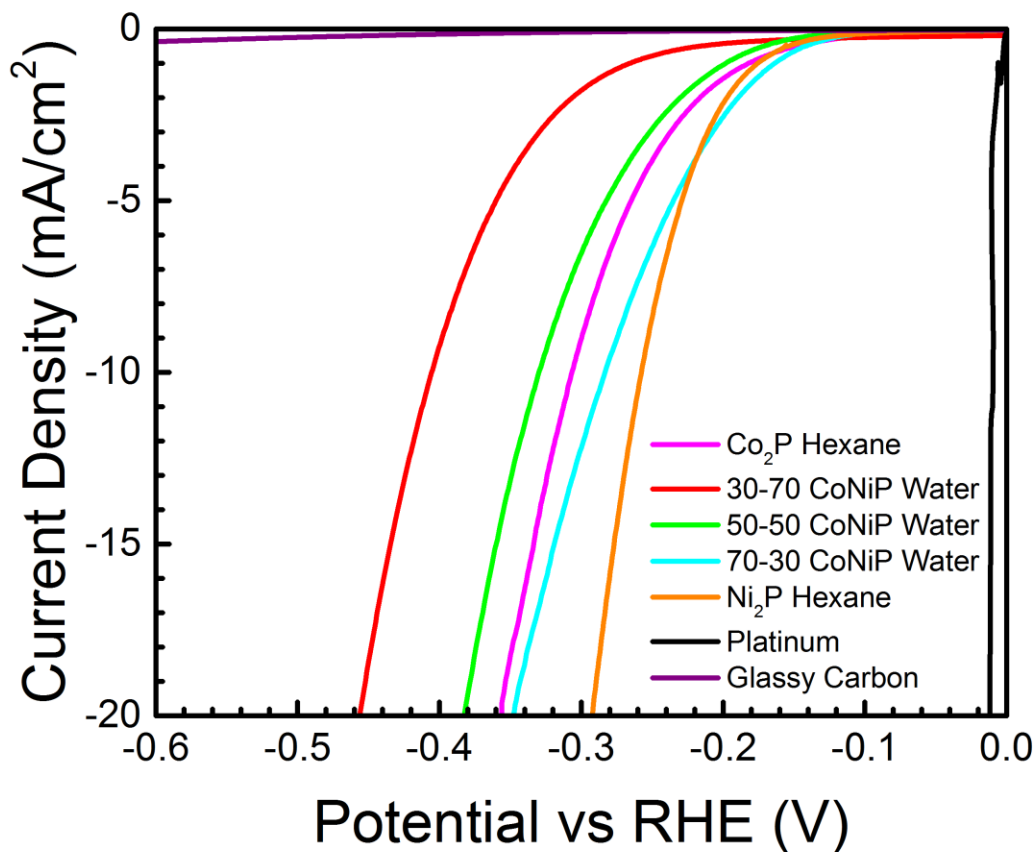
Figure 5.2.3.1 HER Performance of Co$_2$P and Ni$_2$P as well as different ratios of ternary CoNiP

Previously, both Ni$_2$P[4]> and CoP[55] particles have been optimized and demonstrated

excellence for forming hydrogen at low overpotentials. For Ni$_2$P, Popczun et al. achieved

current densities of 20mA/cm^2 at reported overpotentials of 130mV. However, the synthesis

method was significantly more hazardous due to the decomposition of phosphine and was also

time consuming. Furthermore, their loadings were 3 times greater, and they performed post-

processing to remove organic ligands from the surface of the particles. Post-fabrication

optimization of our Ni$_2$P particles for HER including substrate choice, organics removal, and

deposition are likely to yield comparable results to state-of-the-art non-precious metal catalysts.

5.3 Photocatalytic Catalysis

5.3.1 Introduction

Dye degradation has been heavily researched for waste water treatment applications, particularly for the textile industry. Many organic dyes can decompose or react with other natural environmental contents to form toxic products that may be harmful to the environment. One the other hand, some dyes used in textiles without degradation are harmful on their own. Transition metal phosphides consisting of cobalt and nickel phosphide derivatives have shown to be active photocatalysts toward the degradation of organic dyes Pyronine B and Safranine T.[38,56–58] In conjunction with their ability to photcatalytically degrade organic dyes, they have also gained most of their attention for electrocatalysis of the hydrogen and oxygen evolution reactions as discussed in the previous section. Photocatalysis is an interesting property to test these particles for to see if future experiments for HER can produce increase efficacy of the catalyst upon UV irradiation. Some groups are already experimenting with this idea and have found it to be fruitful.[19,59]

Rhodamine B was chosen as the organic dye of interest for no particular reason other than convenience and similarity to other dyes that have been successfully tested with transition metal phosphides. This dye in particular is most often used as a biomarker due to its fluorescent properties and while its degradation is not of utmost concern, it is a good indicator of the synthesized nanoparticles photocatalytic ability. There is some controversy about this dye in

certain states however that have potentially identified the dye as a carcinogen where other

sources disagree.
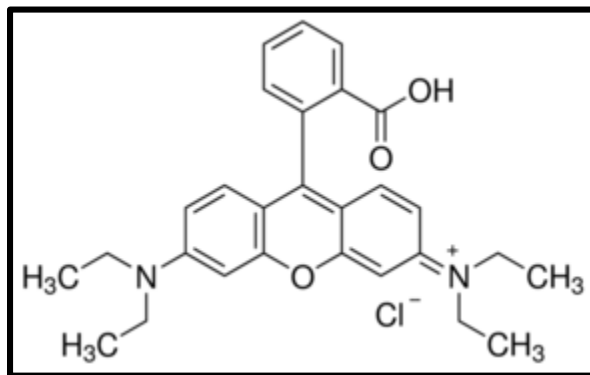
Figure 5.3.1.1: Skeletal Structure of Rhodamine B

5.3.2 Experimental Methods

Rhodamine B is a pink fluorescent dye that is often used in biotechnology and

can easily be monitored by UV-vis spectrometry or a fluorometer. For the purposes of

monitoring photocatalytic degradation ability of different transition metal phosphide particles,

solutions of Rhodamine B were prepared in ethanol and subsequently exposed to ultraviolet

light at a wavelength of 365 nm. Rhodamine B solutions with a concentrations 5 mg L^{-1} in

ethanol were created in the dark. Prepared phosphide nanoparticles (5 mg) were added to 100

mL of a prepared solution and exposed to UV light. To ensure particles were in fact playing an

active role in degradation, a control solution with no particles was exposed to UV light along

with the solutions containing different transition metal phosphide materials. Aliquots of all

solutions were initially taken and measured by UV-vis spectrometry. Subsequent aliquots were

collected of the same solutions in five minute intervals and degradation of Rhodamine B was

monitored over time with different phases of binary and ternary phosphides by monitoring the

predominant peak on the UV-vis spectrum.

5.3.3 Results and Discussion

The photocatalytic degradation of Rhodamine B was measured in the presence

of three separate transition metal phosphide materials. Two binary nickel phosphide phases

and two ternary cobalt nickel phosphide materials. Figure 5.3.3.1 shows the results of these

four samples after exposure to 365 nm UV light for 60 minutes. Note that all test solutions were

made from the same stock solutions and were irradiated at the same time under the same 365

nm UV lamp. The major peak of Rhodamine B at 555 nm was monitored for this study. A

dramatic difference is seen between those samples which contain particles and the sample that

does not contain any particles. A faster rate of degradation clearly occurs with samples

containing transition metal phosphide catalysts vs. no particles at all. Ni_2P and CoNiP-80:20

show similar activity toward Rhodamine but are surpassed by $Ni_{12}P_5$ and CoNiP- 50:50, with the

latter being the most active of the tested transition metal phosphide materials. These results

favor the presence of nickel metal while in the ternary system, activity increases with Ni

content and among the binary phosphides, activity increases with Ni:P ratio when going from 2

(Ni_2P) to 2.4 ($Ni_{12}P_5$).
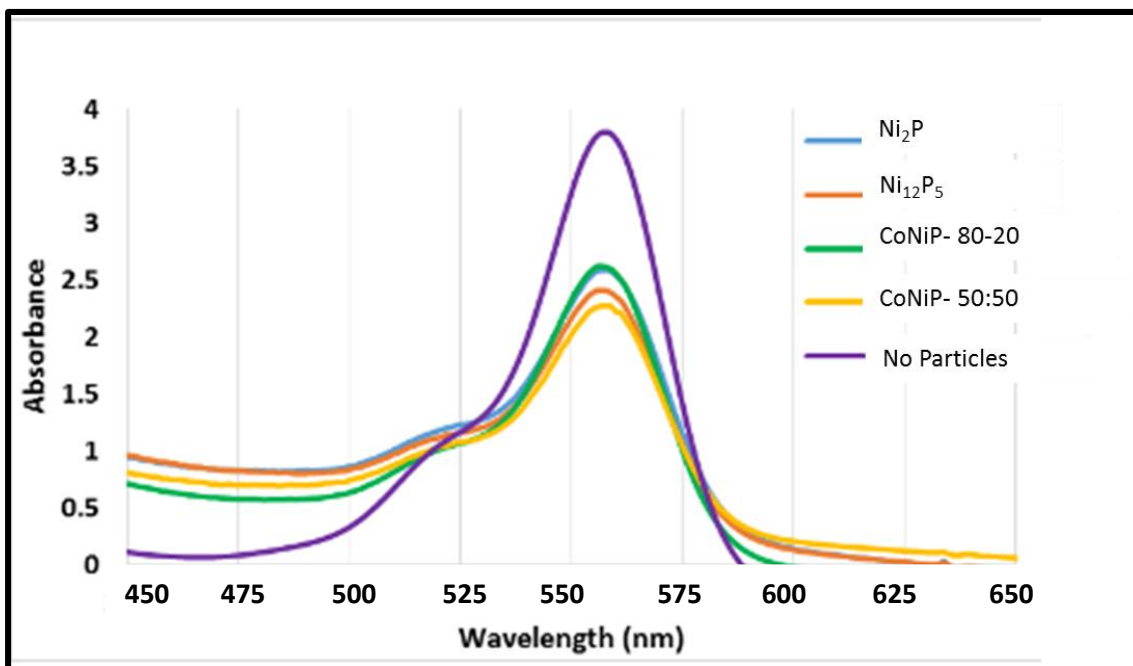
Figure 5.3.3.1: UV-vis Spectrometry Data of Rhodamine B with Different Phases of Phosphides

To ensure that particles were degrading Rhodamine at a faster rate due to UV irradiation was confirmed by placing the most active particles measured in Figure 5.3.3.1 above in solutions that were kept in the dark for the duration of the reaction and exposed to UV light for the entirety of the reaction. Aliquots were taken at 60 min and 120 min and monitored via UV-vis. Figure 5.3.3.2 shows that the particles kept in the dark had larger measured absorbance values at given times than those exposed to UV irradiation indication that the CoNiP particles measured were indeed affected by light
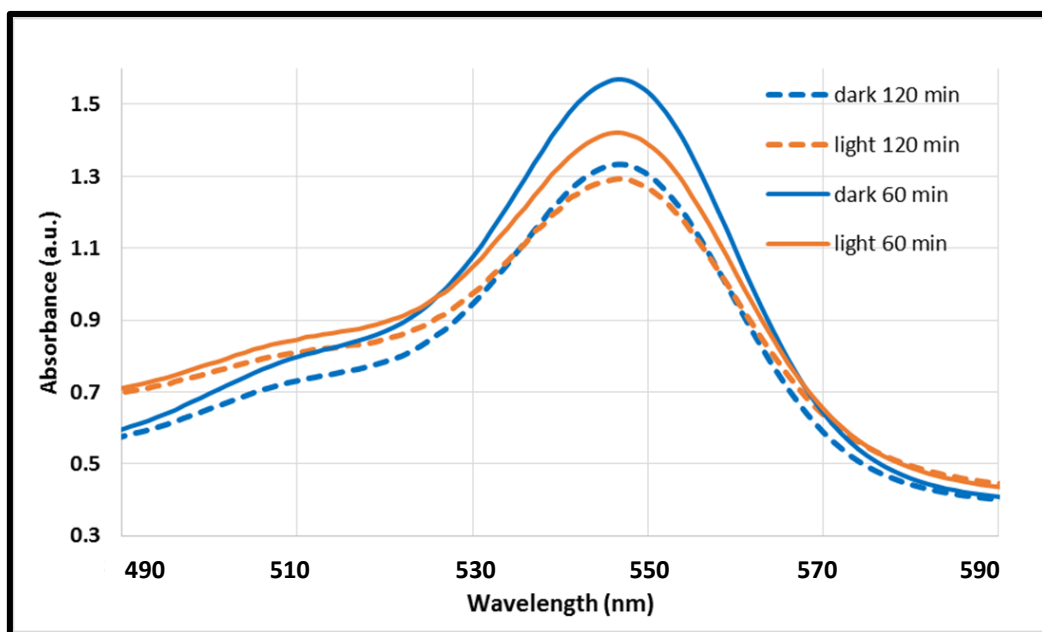
Figure 5.3.3.2: UV-vis Comparison of CoNiP in Rhodamine in Dark vs. UV Light

Lastly, particles were tested for phase stability and the effect of potential organics on the surface on catalytic activity. Sample 479, known to be pure phase $Ni_{12}P_5$ confirmed by x-ray diffraction was annealed in a tube furnace at 425°C for 1 hour. The original and post annealed particles were then evaluated against one another to see if the heat treatment had any effect on phase or photocatalytic activity. When comparing the two diffractograms in Figure 5.3.3.3, it is clearly affirmed by x-ray diffraction that there is no change in phase when comparing the originally synthesized particles to the annealed ones. Photcatalytic activity toward Rhodamine however almost doubles as seen in the UV-vis spectrum comparing the annealed and original particles when exposed to UV irradiation for 60 minutes. This activity difference is likely due to the removal of excess organic material on the surface of the particles providing more active sites for catalysis. To affirm this activity increase, BET surface area measurements were conducted on each sample and showed that surface area doubled upon annealing from 22 m^2/g to 44 m^2/g.
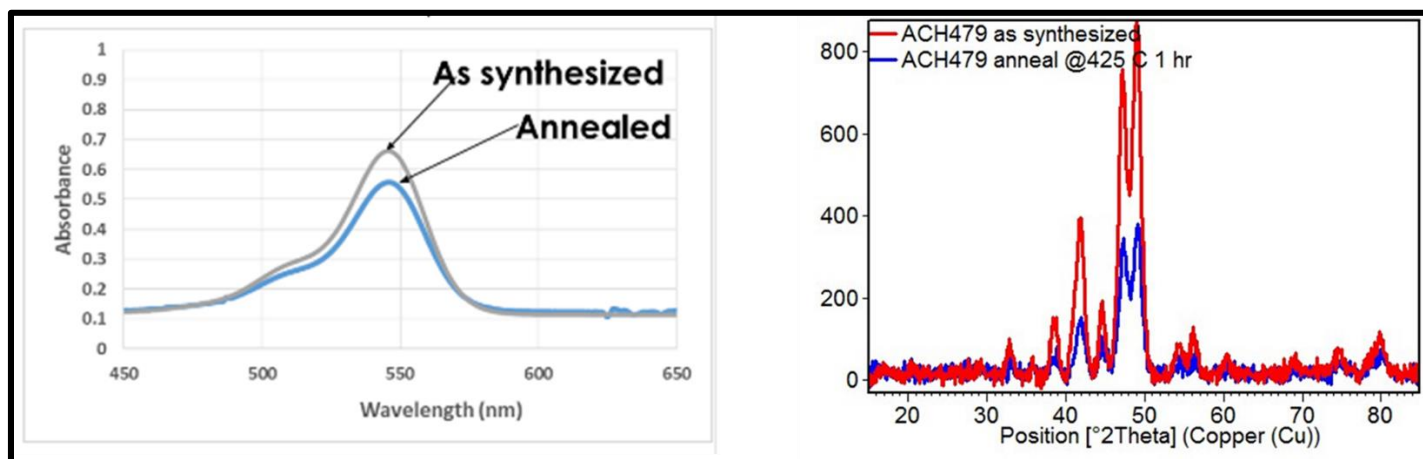
Figure 5.3.3.3: Ni$_{12}$P$_5$ Particles Before and After Annealing: (Left): UV-vis measuring Rhodamine Degradation and (Right) XRD Showing Phase Stability of Ni$_{12}$P$_5$

Morphology retention was also of interest to observe to see if the photocatalytic activity increase and surface area increases were in fact due to surface organic removal or perhaps a change in shape or size of the Ni$_{12}$P$_5$ particles. TEM images presented in Figure 5.3.3.4 show the retention of the hollow spherical/hexagonal particles with comparable sizes of 10-15 nm. The void sizes of these particles also appear to be unchanged which is promising for successful post modification of transition metal phosphide nanoparticles after performing our batch synthesis route.
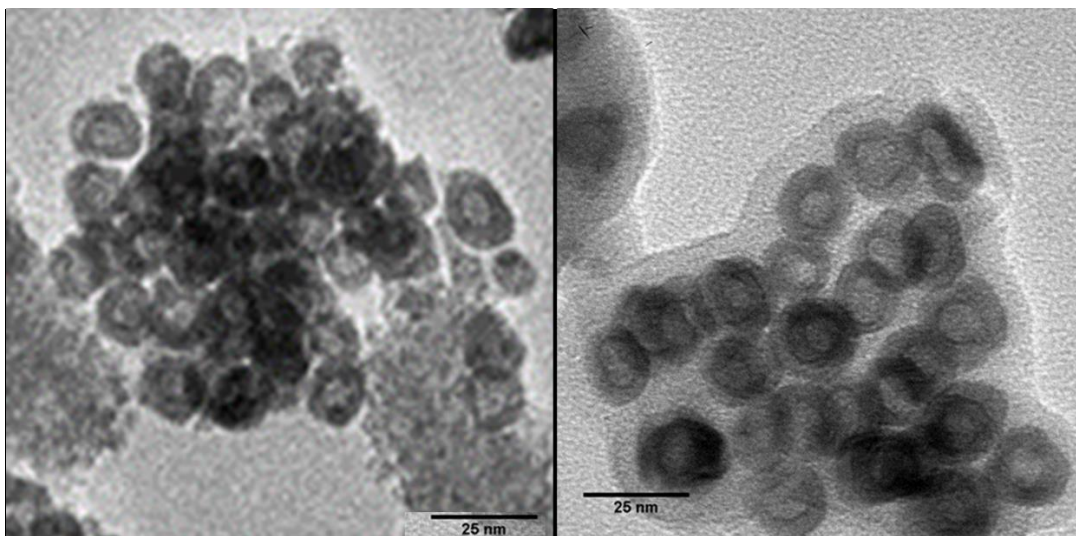
Figure 5.3.3.4: TEM Images of $Ni_{12}P_5$ Particles Before (Left) and After (Right) Annealing

5.4 Conclusion

For both catalytic experiments, binary nickel phosphide phases and ternary phosphide phases with higher nickel contents were more active for both photocatalyic dye degradation and electrocatalysis of the hydrogen evolution reaction. Although further testing needs to be performed for stability of transition metal phosphides with respect to post synthetic processing, the initial results for $Ni_{12}P_5$ post annealing were promising for stability of particles with enhancement of catalytic activity. The combination of electocatalytic activity and photocatalytic activity make transition metal phosphides an attractive candidate for larger scale production or synthesis by simpler and safer methods. These materials could be implemented for a wealth of applications and could potentially use their catalytic activities researched in this chapter cooperatively for enhanced activity toward hydrogen and oxygen evolution, or hydrodesulfurization and hydrodenitrogenation.

Appendix A: Synthesis of FeCo Alloy in Oleylamine

A.1 Motivation

Iron and Cobalt nanoparticles separately have been known to produce materials with interesting ferromagnetic properties. The resulting alloy of these two metals has been reported to possess extremely high magnetic saturation values, making it an attractive soft magnetic material for a multitude of applications. Since it has been shown that iron and cobalt ions are both capable of being reduced by oleylamine, it is advantageous to explore wet chemical methods that are simple and less time consuming than current synthetic methods while maintaining high magnetic saturation values. Oleylamine provides this potential avenue for a simplistic synthetic process that is quick and does not need much material in the way of reagents. Oleylamine will act as the solvent, surfactant and reducing source. In conjunction with testing this method of synthesis of the FeCo alloy for its usefulness as a material itself, the purpose of this work is also to ensure that the FeCo alloy can be made by oleylamine in order to subsequently synthesis the corresponding ternary phosphide material, FeCoP, upon introduction of a phosphorus source. FeCoP has some literature on its properties as a thin film but very little literature has been found on its synthesis by wet chemical methods. This material has the ability to produce interesting magnetic properties as well as potential catalytic properties similar to other transition metal phosphides made with similar metals.

A.2 Introduction

Magnetic nanomaterials are commonly used for biomedical, catalytic and sensing applications.[60] Soft ferromagnetic materials, in particular are often utilized for drug delivery, magnetic separation, data storage, and imaging applications. It is important that these soft materials have high magnetic saturation values for the majority of these applications.[61–64] Therefore, FeCo nanoparticles have gained popularity in recent years due

to their high magnetic saturation value of 240 emu/g.[65] Many avenues to synthesize these particles are being explored in hopes of producing uniform particles with a narrow size distribution, high magnetic saturation, and an efficient and facile synthetic process. To date, FeCo nanoparticles have been synthesized by various processes such as sonochemical reduction, thermal decomposition, chemical vapor deposition, and wet chemical processes. A few of these wet chemical methods have included aqueous borohydride reductions, modified polyol processes, and other time consuming, reagent intensive syntheses.[66,67]

Previous synthetic techniques using oleylamine have involved using surfactants such as oleic acid and trioctylphosphine with reducing agents such as 1,2 hexadecanediol, which achieved good size distributions and high magnetic saturation values.[68] In this study, high magnetic saturation FeCo nanoparticles are synthesized in oleylamine using iron and cobalt salts in the absence of additional surfactants or reducing agents.

A.3 Experimental Methods

A.3.1 FeCo Alloy

In a typical reaction, 20 mL of oleylamine was purged with nitrogen gas for approximately 15 minutes. Under magnetic stirring, cobalt (II) acetate tetrahydrate and anhydrous iron (II) chloride were added to the deoxygenated oleylamine and the suspension was ramped to 320°C. The Fe:Co ratio was varied, while the total metal concentration remained 0.08 M. The particles were aged for 30 minutes upon reaching

the desired temperature then allowed to cool to 40°C before separation. The black/grey

particles were separated magnetically using a rare earth magnet and sonicated several

times with hexane to remove oleylamine from the particles.

Many characterization techniques were carried out to identify particle

composition, crystal phase, size, morphology, aggregation, and magnetic properties.

Powder x-ray diffraction (XRD) was conducted to determine crystal phase of the

synthesized particles at room temperature using Cu Kα radiation, λ=1.54506 Å. Analysis

of phase composition and crystallite size was achieved with the aid of X'Pert Highscore

Plus software using the ICDD/JCPS database for reference. The particle composition was

further investigated by conducting elemental analysis to quantify Fe and Co values using

Inductively Coupled Plasma with Optical Emission Spectroscopy (ICP-OES). The degree

of particle aggregation was observed using a Hitachi SU-70 scanning electron

microscope (SEM) at an accelerating voltage of 10 keV. Thermogravometric analysis

(TGA) was used to ascertain the amount of metal in each sample to yield more accurate

magnetic saturation values. Magnetic characterization used a Quantum Design Versa Lab

vibrating sample magnetometer (VSM) with a 3 Tesla field.

A.4 Results and Discussion

A.4.1.1 Effect of Fe:Co Ratio

The XRD spectra of three different FeCo ratios are shown in Figure 3.4.1.1. The phase change from Co to FeCo can be seen with increasing Fe concentration. Fe:Co ratios are shown as follows: 0:100 (A), 70:30 (B), and 80:20 (C). A mixture of Co and FeCo phases are observed in the XRD spectrum until a starting ratio of 80:20 Fe:Co is used. The crystallite sizes of the Co and FeCo particles were found to be 11.6 nm and 38.5 nm respectively by using the Scherrer equation for each peak and taking the average.
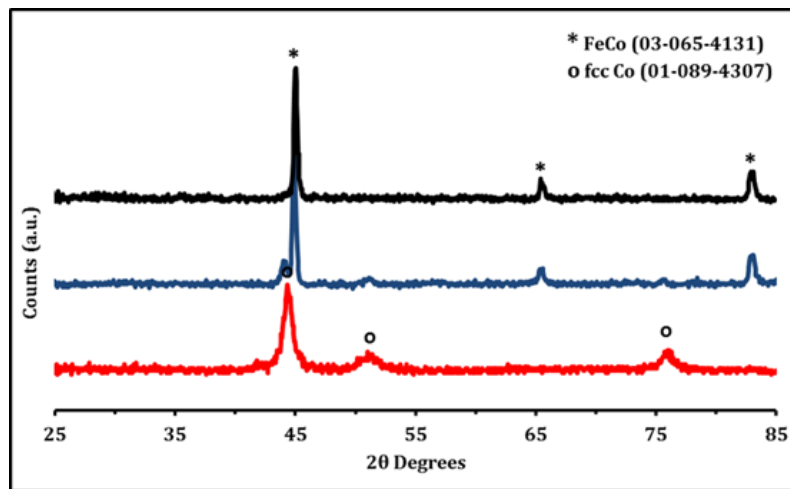
Figure A.4.1.1: XRD spectrum of three different starting ratios of Fe:Co. A) 0:100, B) 70:30, C 80:20

The FeCo particles formed agglomerations that are linear in fashion as seen in Figure 3.4.1.2 (A). These agglomerates seem to consist of particles that

are roughly 300 nm in diameter and look to have a relatively small size

distribution. As for the Co nanoparticles, shown in Figure 2(B), agglomeration

occurs in a different fashion. These spheres are agglomerated into large clusters

with no real preferred orientation. Though the Co spheres have a similar shape

and surface to the FeCo particles, the size of these particles are only about 100

nm. The observed particle diameters were significantly larger than crystallite

sizes determined from XRD analysis, which points toward the individual spheres

being polycrystalline in nature.
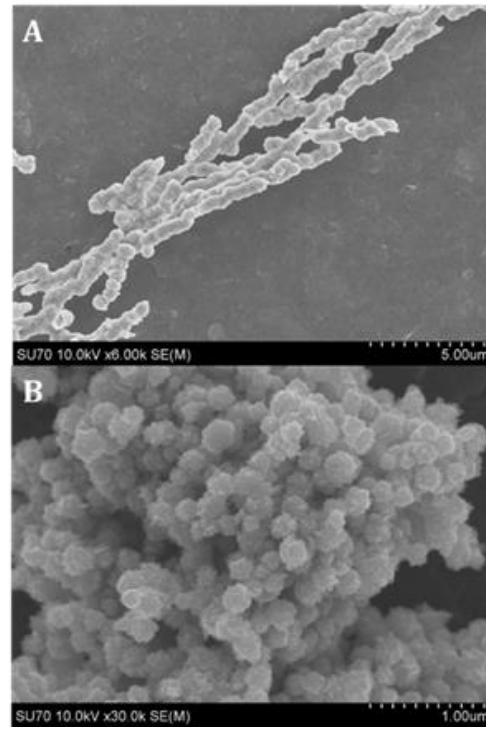
Figure A.4.1.2: SEM images of FeCo nanoparticle agglomerates (A) and Co nanoparticle agglomerates (B)

Figure 4.4.1.3(A) shows the magnetic hysteresis of both Co and FeCo nanoparticles. The Co particles have a magnetic saturation (Ms) of 145 emu/g and a coercivity of 190 Oersted (Oe) and the FeCo particles have a magnetic saturation of 207 emu/g and a coercivity of 100 Oe. Figure 3.4.3 (B) shows the linear correlation between the percentage of Fe in the sample vs. magnetic saturation. Note that these magnetic saturation values are corrected for weight loss observed from TGA experiments. These values have a good linear correlation with an R^2 value of 0.8979 indicating that as the amount of iron in the alloy is increased, the Ms increases accordingly. A maximum magnetization of 207 emu/g is nearly 10% lower than the theoretical maximum for an FeCo at 240 emu/g, however surface oxidation is a common occurrence in Fe based nanomaterials. The presence of some amorphous oxide surface layer is one explanation for the lowered Ms value. The reported magnetization value for pure cobalt is also lower than bulk values, again implying the presence of an amorphous oxide component.
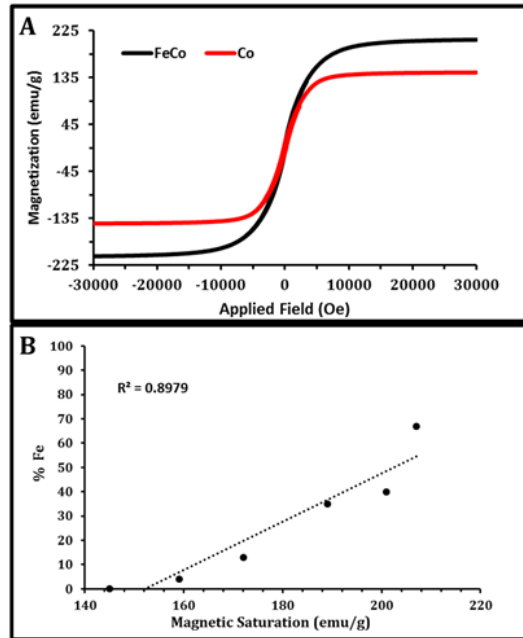
Figure 4.4.1.3: Magnetic hysteresis loops for Co and FeCo particles (A) and liner correlation of % Fe in particles from ICP-OES vs. Ms (B)

The percentage of iron in the alloy increases and the Ms increases up to a maximum value of 67% seen in the Fe:Co 95:5 ratio. One possible explanation for this maximum is the cobalt particles are reduced first and act as nucleation site for the iron to insert itself into the forming cobalt lattice. This may be the reason that both Co and FeCo signals are seen in the XRD pattern until there is a higher concentration of iron in the system. It is worthwhile to mention that in the absence of iron (II) chloride we can produce Co particles but in the absence of cobalt (II) acetate no Fe particles are generated. Furthermore, when iron (II) chloride and cobalt (II) chloride are reacted in oleylamine, no product is collected. Metal particles are attained with both chloride salts only if sodium acetate is introduced into the system. The presence of the carboxylate group on the acetate is most likely aiding in the reduction of the metals by altering the

identity of the primary amine to an imine. Further mechanism studies will have to be conducted in order to ascertain more comprehensive reduction information.

A.4.1.2 Effect of Temperature

For this particular synthesis, temperature proved to be an important parameter. Carrying out reactions above the desired 320°C resulted in impurities in the form of cobalt carbide, thus lowering the M_s and increasing the H_c. These carbide phases can be easily identified in the x-ray diffraction patterns of affected samples and correlated to their magnetics data. Figure 3.4.2.1 shows the changes in the x-ray diffraction pattern corresponding to the formation of carbide phases above temperatures of 330°C. The formation of cobalt carbide is not a surprise at high temperatures, as our group has previously synthesized Co_2C and Co_3C under similar conditions.[5]> Since FeCo is characteristically a soft magnet and cobalt carbide tends to behave more like a hard magnet, the changes in the VSM hystereses are easily seen as a function of temperature as seen in Figure 3.4.2.2. 84 27 emu/g and 500 Oe; 90 160 emu/g and 100 Oe
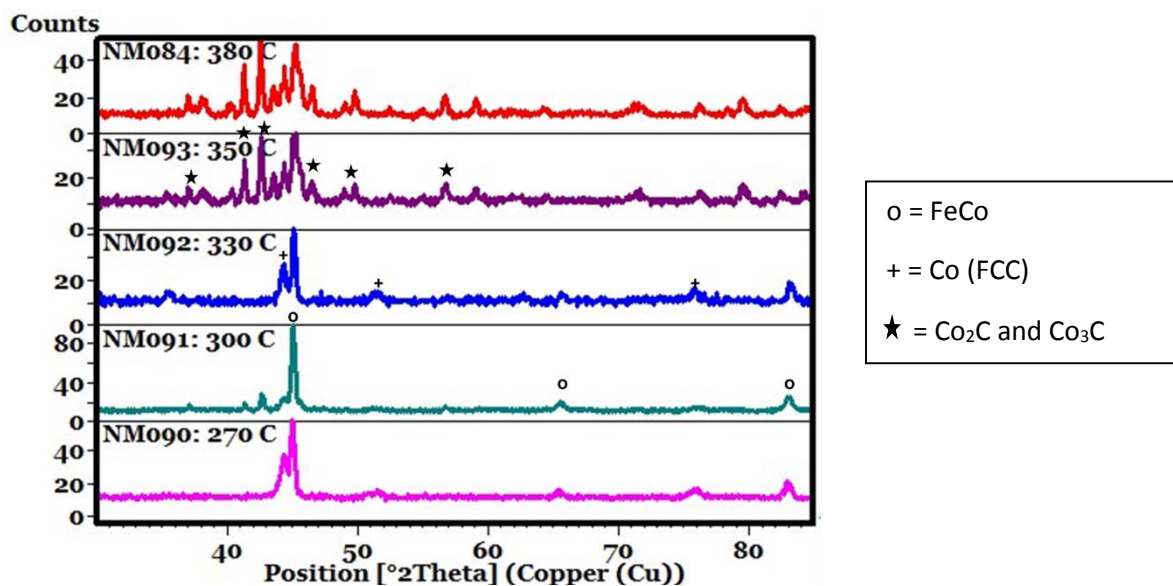
Figure A.4.2.1: XRD Comparison of 50:50 ratio reactions of Fe(OAc)$_2$ and Co(OAc)$_2$ for 1 hr at different temperatures.

A.4.1.3 Effect of Precursor/Surfactant

In a typical synthesis, oleylamine acts as both the reducing agent as well as the surfactant for the FeCo particles. Introducing trioctylphosphine (TOP) into the system alongside OAm has proved to provide some interesting particle shapes across a wide variety of syntheses. This case was no different. In an attempt to change only the particle shape or size of the FeCo particles previously synthesized, the phase was also altered to incorporate phosphorus into the crystal structure. This addition resulted in the the formation of iron and cobalt phosphides or a ternary version iron-cobalt phosphide. Figure 3.4.3.1 shows TEM images of FeCo particles synthesized with TOP as a co-surfactant instead of just oleylamine as the reducing source, solvent and surfactant. This however changes the phase of the material from FeCo to FeCoP. The use of iron (III)

acetylacetonate as an iron precursor as opposed to iron (II) acetate formed FeCo

nanocubes as opposed to spheres. Although these morphology changes are

interesting, they do not increase the overall saturation magnetization of the

FeCo material which is the ultimate goal.

| A | B |
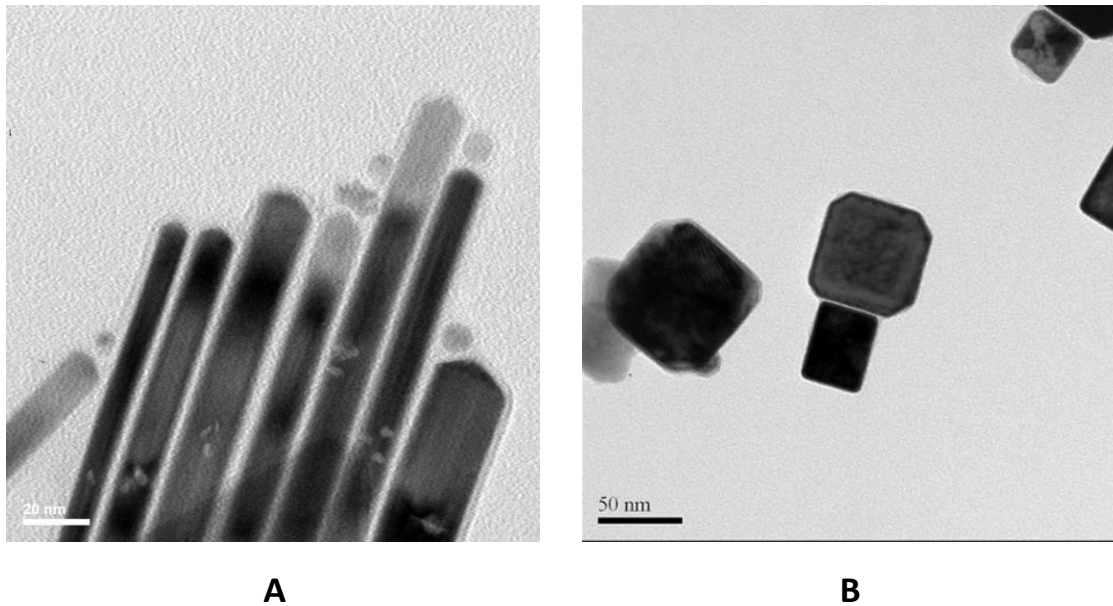
Figure A.4.1.3.1: Morphology differences when using TOP as a co-surfactant (A) and Iron (III)
acetylacetonate as an iron precursor (B)

A.5 Conclusion

Co and FeCo nanoparticles have been synthesized by a facile method

using only oleylamine with cobalt and iron precursors. These Co and FeCo

particles possessed high magnetic saturation values with regard to their given

phases of 145 emu/g and 207 emu/g respectively. Maximum magnetization

values were recorded for an FeCo alloy containing 67% Fe, as determined by ICP-

OES. SEM images show the morphology of both particles was spherical while the

Co particles were 100 nm in diameter and the FeCo nanoparticles were 300 nm

in diameter. The high magnetic saturation of FeCo nanoparticles and ease of the synthetic process makes them useful for many engineering and separation applications.[70,71]

References

(1)   Brock, S. L.; Senevirathne, K. *J. Solid State Chem.* **2008**, *181*, 1552–1559.

(2)   Boyanov, S.; Annou, K.; Villevieille, C.; Pelosi, M.; Zitoun, D.; Monconduit, L. *Ionics (Kiel).* **2007**, *14*, 183–190.

(3)   Pan, Y.; Liu, Y.; Liu, C. *J. Power Sources* **2015**, *285*, 169–177.

(4)   Wang, Y.; Li, X.; Sun, Z.; Wang, A. Metal phosphides as high-performance hydrotreating catalysts. *Journal of the Japan Petroleum Institute*, 2015.

(5)   Kanda, Y.; Aizawa, T.; Kobayashi, T.; Uemichi, Y.; Namba, S.; Sugioka, M. *Appl. Catal. B Environ.* **2007**, *77*, 117–124.

(6)   Yi, Y.; Jin, X.; Wang, L.; Zhang, Q.; Xiong, G.; Liang, C. *Catal. Today* **2011**, *175*, 460–466.

(7)   Topsøe, H. *Appl. Catal. A Gen.* **2007**, *322*, 3–8.

(8)   Prins, R.; Bussell, M. E. *Catal. Letters* **2012**, *142*, 1413–1436.

(9)   Zuzaniuk, V.; Prins, R. *J. Catal.* **2003**, *219*, 85–96.

(10)   M.S., C.; Mitra, S. *Ionics (Kiel).* **2013**, 137–140.

(11)   Yang, D.; Zhu, J.; Rui, X.; Tan, H.; Cai, R.; Hoster, H. E.; Yu, D. Y. W.; Hng, H. H.; Yan, Q. *ACS Appl. Mater. Interfaces* **2013**, *5*, 1093–1099.

(12)   Lu, Y.; Tu, J. P.; Xiang, J. Y.; Wang, X. L.; Zhang, J.; Mai, Y. J.; Mao, S. X. *J. Phys. Chem. C* **2011**, *115*, 23760–23767.

(13)   Lu, Y.; Tu, J.; Xiong, Q.; Qiao, Y.; Wang, X.; Gu, C.; Mao, S. X. *RSC Adv.* **2012**, *2*, 3430.

(14)   Merki, D.; Hu, X.; Crabtree, G. W.; Dresselhaus, M. S.; Buchanan, M. V.; Turner, J. A.; Lewis, N. S.; Nocera, D. G.; Shimura, K.; Yoshida, H.; Vignais, P. M.; Billoud, B.; Meyer, J.; Cook, T. R.; Dogutan, D. K.; Reece, S. Y.; Surendranath, Y.; Teets, T. S.; Nocera, D. G.; Tard, C.; Pickett, C. J.; DuBois, M. R.; DuBois, D. L.; Artero, V.; Fontecave, M.; Appel, A. M.; DuBois, D. L.; DuBois, M. R.; Prins, R.; Debeer, V. H. J.; Somorjai, G. A.; Spalvins, T.; Jaegermann, W.; Tributsch, H.; Albertini, L. B.; Angelo, A. C. D.; Gonzalez, E. R.; Nidola, A.; Schira, R.; Sobczynski, A.; Yildiz, A.; Bard, A. J.; Campion, A.; Fox, M. A.; Mallouk, T.; Webber, S. E.; White, J. M.; Hinnemann, B.; Moses, P. G.; Bonde, J.; Jorgensen, K. P.; Nielsen, J. H.; Horch, S.; Chorkendorff, I.; Norskov, J. K.; Helveg, S.; Lauritsen, J. V.; Laegsgaard, E.; Stensgaard, I.; Norskov, J. K.; Clausen, B. S.; Topsoe, H.; Besenbacher, F.; Lauritsen, J. V.; Bollinger, M. V.; Laegsgaard, E.; Jacobsen, K. W.; Norskov, J. K.; Clausen, B. S.; Topsoe, H.; Besenbacher, F.; Jaramillo, T. F.; Jorgensen, K. P.; Bonde, J.; Nielsen, J. H.; Horch, S.; Chorkendorff, I.; Daage, M.; Chianelli, R. R.; Bonde, J.; Moses, P. G.; Jaramillo, T. F.; Norskov, J. K.; Chorkendorff, I.; Brorson, M.; Carlsson, A.; Topsoe, H.; Agarwal, M. K.; Nagireddy, K.; Patel, H. B.; Byskov, L. S.; Norskov, J. K.; Clausen, B. S.; Topsoe, H.; Lauritsen, J. V.; Helveg, S.; Laegsgaard, E.; Stensgaard, I.; Clausen, B. S.; Topsoe, H.; Besenbacher, E.; Okamoto, Y.; Tamura, K.; Kubota, T.; Li, Y.; Wang, H.; Xie, L.; Liang, Y.; Hong, G.; Dai, H.; Jaramillo, T. F.; Bonde, J.; Zhang, J. D.; Ooi, B. L.; Andersson, K.; Ulstrup, J.; Chorkendorff, I.; Muijsers, J. C.; Weber, T.; vanHardeveld, R. M.; Zandbergen, H. W.; Niemantsverdriet, J. W.; Weber, T.; Muijsers, J. C.; Niemantsverdriet, J. W.; Zong, X.; Yan, H. J.; Wu, G. P.; Ma, G. J.; Wen, F. Y.; Wang, L.; Li, C.; Park,

100

H. G.; Holt, J. K.; Hernandez-Alonso, M. D.; Fresno, F.; Suarez, S.; Coronado, J. M.; Sobczynski, A.; Zong, X.; Na, Y.; Wen, F. Y.; Ma, G. J.; Yang, J. H.; Wang, D. G.; Ma, Y.; Wang, M.; Sun, L.; Li, C.; Kanda, S.; Akita, T.; Fujishima, M.; Tada, H.; Hou, Y. D.; Abrams, B. L.; Vesborg, P. C. K.; Bjorketun, M. E.; Herbst, K.; Bech, L.; Setti, A. M.; Damsgaard, C. D.; Pedersen, T.; Hansen, O.; Rossmeisl, J.; Dahl, S.; Norskov, J. K.; Chorkendorff, I.; Merki, D.; Fierro, S.; Vrubel, H.; Hu, X.; Boettcher, S. W.; Spurgeon, J. M.; Putnam, M. C.; Warren, E. L.; Turner-Evans, D. B.; Kelzenberg, M. D.; Maiolo, J. R.; Atwater, H. A.; Lewis, N. S.; Belanger, D.; Laperriere, G.; Marsan, B.; Laperriere, G.; Marsan, B.; Belanger, D.; Ponomarev, E. A.; NeumannSpallart, M.; Hodes, G.; LevyClement, C.; Albu-Yaron, A.; Levy-Clement, C.; Hutchison, J. L.; Ponomarev, E. A.; AlbuYaron, A.; Tenne, R.; LevyClement, C.; Roy, P.; Srivastava, S. K.; Bockris, J. O. M.; Potter, E. C.; Thomas, J. G. *Energy Environ. Sci.* **2011**, *4*, 3878.

(15)   Ha, D.-H.; Han, B.; Risch, M.; Giordano, L.; Yao, K. P. C.; Karayaylali, P.; Shao-Horn, Y. *Nano Energy* **2016**.

(16)   Izhar, S.; Nagai, M. *Catal. Today* **2009**, *146*, 172–176.

(17)   Pan, Y.; Lin, Y.; Chen, Y.; Liu, Y.; Liu, C. *J. Mater. Chem. A* **2016**, *4*, 4745–4754.

(18)   Xu, M.; Han, L.; Han, Y.; Yu, Y.; Zhai, J.; Dong, S. .

(19)   Uniformly Sized (112) Facet Co2P on Graphene for Highly Effective Photocatalytic Hydrogen Evolution
http://pubs.acs.org.proxy.library.vcu.edu/doi/pdf/10.1021/acs.jpcc.6b00680?source=chemport (accessed Mar 29, 2016).

(20)   Li, H.; Wang, W.; Gong, Z.; Yu, Y.; Piao, lijin; Chen, H.; Xia, J. *J. Phys. Chem. Solids* **2015**, *80*, 22–25.

(21)   Li, J.; Zhou, X.; Xia, Z.; Zhang, Z.; Li, J.; Ma, Y.; Qu, Y. .

(22)   Pan, Y.; Liu, Y.; Liu, S. Y.; Liu, C.; Lin, Y.; Chen, Y. .

(23)   Wu, W.; Yue, X.; Wu, X.-Y.; Lu, C.-Z. .

(24)   Yang, H.; Zhang, Y.; Hu, F.; Wang, Q. .

(25)   FUENTES, S. *J. Catal.* **1988**, *113*, 535–539.

(26)   Rodriguez, J. A.; Kim, J.-Y.; Hanson, J. C.; Sawhill, S. J.; Bussell, M. E. *J. Phys. Chem. B* **2003**, *107*, 6276–6285.

(27)   SUN, F.; WU, W.; WU, Z.; GUO, J.; WEI, Z.; YANG, Y.; JIANG, Z.; TIAN, F.; LI, C. *J. Catal.* **2004**, *228*, 298–310.

(28)   ABU, I.; SMITH, K. *J. Catal.* **2006**, *241*, 356–366.

(29)   Abu, I. I.; Smith, K. J. *Appl. Catal. A Gen.* **2007**, *328*, 58–67.

(30)   Burns, A. W.; Gaudette, A. F.; Bussell, M. E. *J. Catal.* **2008**, *260*, 262–269.

(31)   Ma, D.; Xiao, T.; Xie, S.; Zhou, W.; Gonzalez-Cortes, S. L.; Green, M. L. H. *Chem. Mater.* **2004**, *16*, 2697–2699.

(32)   Guérin, R.; Sergent, M. *Mater. Res. Bull.* **1977**, *12*, 381–388.

(33)   Li, Y.; Malik, M. A.; O'Brien, P. *J. Am. Chem. Soc.* **2005**, *127*, 16020–16021.

(34)   Guo, H.; Liu, X.; Hou, Y.; Xie, Q.; Wang, L.; Geng, H.; Peng, D.-L. *J. Power Sources* **2014**, *260*, 100–108.

(35)   Hou, H.; Peng, Q.; Zhang, S.; Guo, Q.; Xie, Y. *Eur. J. Inorg. Chem.* **2005**, *2005*, 2625–2630.

(36)   Henkes, A. E.; Schaak, R. E. **2007**, 4234–4242.

(37)   Muthuswamy, E.; Savithra, G. H. L.; Brock, S. L. **2011**, 2402–2411.

(38)   Ni, Y.; Jin, L.; Hong, J. *Nanoscale* **2011**, *3*, 196–200.

(39)   Sawhill, S. *J. Catal.* **2003**, *215*, 208–219.

(40)   Feng, L.; Vrubel, H.; Bensimon, M.; Hu, X. *Phys. Chem. Chem. Phys.* **2014**, *16*, 5917–5921.

(41)   Bowker, R. H.; Ilic, B.; Carrillo, B. A.; Reynolds, M. A.; Murray, B. D.; Bussell, M. E. *Appl. Catal. A Gen.* **2014**, *482*, 221–230.

(42)   Bu, W.; Chen, Z.; Chen, F.; Shi, J. *J. Phys. Chem. C* **2009**, *113*, 12176–12185.

(43)   Zou, X.; Hovmoller, S.; Oleynikov, P. *Electron Crystallography: Electron Microscopy and Electron Diffraction*; Vol.16 ed.; Oxford University Press: Oxford, 2011.

(44)   Huessein, G.A.M.; Nohman, A.K.H.; Attiya, K. M. A. *J. Therm. Anal. Calorim.* **1994**, *42*, 1155–1165.

(45)   Mohamed, M.A.; Hallawy, S.A.;Ebrahim, M. M. *J. Anal. Appl. Pyrolysis* **1993**, *27*, 109–110.

(46)   Nam, K. M.; Shim, J. H.; Ki, H.; Choi, S.-I.; Lee, G.; Jang, J. K.; Jo, Y.; Jung, M.-H.; Song, H.; Park, J. T. *Angew. Chemie Int. Ed.* **2008**, *47*, 9504–9508.

(47)   Oleylamine in Nanoparticle Synthesis http://pubs.acs.org/doi/ipdf/10.1021/cm4000476 (accessed Mar 10, 2014).

(48)   Patterson, A. L. .

(49)   Singh, A. K. *Advanced X-ray Techniques in Research and Industries*; Los Pr Inc., 2005.

(50)   Pearson, W. B. *Handbook of Lattice Spacings and Structures of Metals*; Vol. 2.; Pergamon Press: London, 1967.

(51)   Fassel, V. A.; Kniseley, R. N. *Anal. Chem.* **1974**, *46*, 1110A – 1120A.

(52)   Song, L.; Zhang, S.; Wei, Q. *Powder Technol.* **2011**, *212*, 367–371.

(53)   Fruchart, R. *J. Appl. Phys.* **1969**, *40*, 1250.

(54)   Popczun, E. J.; McKone, J. R.; Read, C. G.; Biacchi, A. J.; Wiltrout, A. M.; Lewis, N. S.; Schaak, R. E. *J. Am. Chem. Soc.* **2013**, *135*, 9267–9270.

(55)   Saadi, F. H.; Carim, A. I.; Verlage, E.; Hemminger, J. C.; Lewis, N. S.; Soriaga, M. P. *J. Phys. Chem. C* **2014**.

(56)   Mi, K.; Ni, Y.; Hong, J. *J. Phys. Chem. Solids* **2011**, *72*, 1452–1456.

(57)   Ni, Y.; Li, J.; Zhang, L.; Yang, S.; Wei, X. *Mater. Res. Bull.* **2009**, *44*, 1166–1172.

(58)   Li, J.; Ni, Y.; Liao, K.; Hong, J. *J. Colloid Interface Sci.* **2009**, *332*, 231–236.

(59)   Shi, Y.; Zhang, B.; Faber, M. S.; Jin, S.; Jiao, Y.; Zheng, Y.; Jaroniec, M.; Qiao, S. Z.; Zheng, Y.; Jiao, Y.; Qiao, S. Z.; Zou, X.; Zhang, Y.; Morales-Guio, C. G.; Stern, L. A.; Hu, X.; Carenco, S.; Portehault, D.; Boissiere, C.; Mezailles, N.; Sanchez, C.; Liu, P.; Rodriguez, J. A.; Xu, Y.; Wu, R.; Zhang, J.; Shi, Y.; Zhang, B.; Popczun, E. J.; McKone, J. R.; Read, C. G.; Biacchi, A. J.; Wiltrout, A. M.; Lewis, N. S.; Schaak, R. E.; Laursen, A. B.; Patraju, K. R.; Whitaker, M. J.; Retuerto, M.; Sarkar, T.; Yao, b. N.; Ramanujachary, K. V.; Greenblatt, M.; Dismukes, G. C.; Liang, Y.; Liu, Q.; Asiri, A. M.; Sun, X.; Luo, Y.; Pu, Z.; Liu, Q.; Asiri, A. M.; Sun, X.; Tian, J.; Liu, Q.; Asiri, A. M.; Sun, X.; Vrubel, H.; Moehl, T.; Gratzel, M.; Hu, X.; Xiao, P.; Sk, M. A.; Thia, L.; Ge, X.; Lim, R. J.; Wang, J.; Lim, K. H.; Wang, X.; Wu, R.; Zhang, J.; Shi, Y.; Liu, D.; Zhang, B.; Pan, Y.; Liu, Y.; Zhao, J.; Yang, K.; Liang, J.; Liu, D.; Hu, W.; Liu, D.; Liu, Y.; Liu, C.; Callejas, J. F.; Read, C. G.; Popczun, E. J.; McEnaney, J. M.; Schaak, R. E.; Blanchard, P. E. R.; Grosvenor, A. P.; Cavell, R. G.; Mar, A.; Jaramillo, T. F.; Jørgensen, K. P.; Bonde, J.; Nielsen, J. H.; Horch, S.; Chorkendorff, I.; Kucernak, A. R. J.; Sundaram, V. N. N.; Kibsgaard, J.; Jaramillo, T. F.; Saadi, F. H.; Carim, A. I.; Verlage, E.; Hemminger, J. C.; Lewis, N. S.; Soriaga, M. P.; Wang, X.; Kolen'ko, Y. V.; Liu, L.; Han, S.; Feng, Y.; Zhang, F.; Yang, C.; Yao, Z.; Zhao, W.; Qiu, F.; Yang, L.; Yao, Y.; Zhuang, X.; Feng, X.; Lu, Z.; Zhu, W.; Yu, X.; Zhang, H.; Li, Y.; Sun, X.; Wang, X.; Wang, H.; Wang, J.; Luo, J.; Lei, X.; Jiang, L.; Shi, Y.; Xu, Y.; Zhuo, S.; Zhang, J.; Zhang, B.; Cao, S.; Chen, Y.; Hou, C.; Lv, X.; Fu, W.; Huang, Z.; Chen, Z.; Chen, Z.; Lv, C.; Meng, H.; Zhang, C.; Tian, J.; Liu, Q.; Cheng, N.; Asiri, A. M.; Sun, X.; Wu, T.; Chen, S.; Zhang, D.; Hou, J.; Tian, T.; Ai, L.; Jiang, J.; Deng, J.; Ren, P.; Deng, D.; Bao, X.; Liu, Q.; Tian, J.; Cui, W.; Jiang, P.; Cheng, N.; Asiri, A. M.; Sun, X.; Zhuo, J.; Cabán-Acevedo, M.; Liang, H.; Samad, L.; Ding, Q.; Fu, Y.; Li, M.; Jin, S.; Jin, Z.; Li, P.; Huang, X.; Zeng, G.; Jin, Y.; Zheng, B.; Xiao, D.; Wang, X.; Kolen'ko, Y. V.; Bao, X. Q.; Kovnir, K.; Liu, L.; Zheng, Y.; Jiao, Y.; Jaroniec, M.; Qiao, S. Z.; Hansen, M. H.; Stern, L.-A.; Feng, L.; Rossmeisl, J.; Hu, X.; Zou, X.; Huang, X.; Goswami, A.; Silva, R.; Sathe, B. R.; Mikmekova, E.; Asefa, T.; Ledendecker, M.; Calderon, S. K.; Papp, C.; Steinruck, H. P.; Antonietti, M.; Shalom, M.; Ryu, J.; Jung, N.; Jang, J. H.; Kim, H. J.; Yoo, S. J.; Yang, Y.; Fei, H.; Ruan, G.; Tour, J. M.; Ran, J.; Zhang, J.; Yu, J.; Jaroniecc, M.; Qiao, S. Z.; Callejas, J. F.; McEnaney, J. M.; Read, C. G.; Crompton, J. C.; Biacchi, A. J.; Popczun, E. J.; Gordon, T. R.; Lewis, N. S.; Schaak, R. E.; Lee, S. W.; Carlton, C.; Risch, M.; Surendranath, Y.; Chen, S.; Furutsuki, S.; Yamada, A.; Nocera, D. G.; Shao-Horn, Y.; Xia, Y.; Xiong, Y.; Lim, B.; Skrabalak, S. E.; Ren, B.; Xu, X.; Li, X. Q.; Cai, W. B.; Tian, Z. Q.; Li, J. F.; Huang, Y. F.; Ding, Y.; Yang, Z. L.; Li, S. B.; Zhou, X. S.; Fan, F. R.; Zhang, W.; Zhou, Z. Y.; Wu, D. Y.; Ren, B.; Wang, Z. L.; Tian, Z. Q.; Kornienko, N.; Resasco, J.; Becknell, N.; Jiang, C. M.; Liu, Y. S.; Nie, K.; Sun, X.; Guo, J.; Leone, S. R.; Yang, P. *Chem. Soc. Rev.* **2016**, *45*, 1529–1541.

(60)   Frey, N. a; Peng, S.; Cheng, K.; Sun, S. *Chem. Soc. Rev.* **2009**, *38*, 2532–2542.

(61)   Huetten, A.; Sudfeld, D.; Ennen, I.; Reiss, G.; Wojczykowski, K.; Jutzi, P. *J. Magn. Magn. Mater.* **2005**, *293*, 93–101.

(62)   Huetten, A.; Sudfeld, D.; Ennen, I.; Reiss, G.; Wojczykowski, K.; Jutzi, P. In *IEEE-NANO 2004, Fourth IEEE Conf. Nanotechnol.*; Institute of Electrical and Electronics Engineers, 2004; pp. 322–324.

(63)   Thirumal, E.; Prabhu, D.; Chattopadhyay, K.; Ravichandran, V. *Phys. Status Solidi* **2010**, *207*, 2505–2510.

(64)   Behrens, S.; Bönnemann, H.; Matoussevitch, N.; Gorschinski, A.; Dinjus, E.; Habicht, W.; Bolle, J.; Zinoveva, S.; Palina, N.; Hormes, J.; Modrow, H.; Bahr, S.; Kempter, V. *J. Phys. Condens. Matter* **2006**, *18*, S2543–S2561.

(65)   Hunger, C.; Ojo, W.-S.; Bauer, S.; Xu, S.; Zabel, M.; Chaudret, B.; Lacroix, L.-M.; Scheer, M.; Nayral, C.; Delpech, F. *Chem. Commun. (Camb).* **2013**, *49*, 11788–11790.

(66)   Zin, V.; Zanella, A.; Agnoli, A.; Brunelli, K.; Dabala, M. *Curr. Nanosci.* **2009**, *5*, 232–239.

(67)   Huba, Z. J.; Carroll, K. J.; Carpenter, E. E. *J. Appl. Phys.* **2011**, *109*, 07B514.

(68)   Chaubey, G. S.; Barcena, C.; Poudyal, N.; Rong, C.; Gao, J.; Sun, S.; Liu, J. P. **2007**, 7214–7215.

(69)   Huba, Z. J.; Carpenter, E. E. *CrystEngComm* **2014**, *16*, 8000.

(70)   Park, J.; Kang, E.; Son, S. U.; Park, H. M.; Lee, M. K.; Kim, J.; Kim, K. W.; Noh, H.-J.; Park, J.-H.; Bae, C. J.; Park, J.-G.; Hyeon, T. *Adv. Mater.* **2005**, *17*, 429–434.

(71)   Choi, S.-H.; Na, H. Bin; Park, Y. Il; An, K.; Kwon, S. G.; Jang, Y.; Park, M.; Moon, J.; Son, J. S.; Song, I. C.; Moon, W. K.; Hyeon, T. **2008**.